Channel-selective analysis of light-induced wave packet dynamics in molecules

by

Sanduni Sandeepani Kudagama

B.Sc., University of Colombo, Sri Lanka, 2020

A THESIS

submitted in partial fulfillment of the requirements for the degree

MASTER OF SCIENCE

Department of Physics
College of Arts and Sciences

KANSAS STATE UNIVERSITY
Manhattan, Kansas

2025

Approved by:

Major Professor
Artem Rudenko

Copyright

Abstract

Many light-induced molecular processes, including photosynthesis, biosynthesis of vitamin D, or isomerization in retinal chromophore, are essential for human existence on Earth. A traditional approach for studying such photochemical and photobiological reactions focuses on the initial molecular structure and the final products formed during these processes. However, this point of view does not provide information on the short-lived, transient molecular configurations, which often determine both the mechanisms and the outcome of the reaction. A particular challenge here is that light-induced changes in molecular structure typically occur on a very fast time scale, determined by the motion of individual atoms. Hence, with the development of femtosecond lasers and modern molecular imaging techniques, time-resolved studies of ultrafast light-induced dynamics have become an increasingly important topic in molecular physics and photochemistry.

To capture ultrafast molecular dynamics in the time domain, femtosecond lasers are often used in a pump-probe scheme, where the pump pulse initiates the dynamics of interest and the probe pulse interrogates the evolving system at different times. Here, the probe step needs to employ an experimental technique that can provide information on evolving molecular structure. One of the promising approaches to address this goal is the so-called Coulomb Explosion Imaging (CEI), which relies on rapid multiple ionization and subsequent fragmentation of the target molecule. The information on molecular structure at the instant of laser-molecular interaction is then encoded in the momenta of the created positively charged ions, which can be measured as a function of time delay between pump and probe pulses. This approach can be efficiently combined with time-resolved ion mass spectrometry and Fourier analysis of different delay-dependent observables, including ion yields, their kinetic energies, or angular distributions, in particular, if COLd Target Recoil Ion Momentum Spectroscopy (COLTRIMS) is used to characterize the created ionic fragments.

The thesis focuses on two major aspects of light-induced molecular dynamics studies. The first part of the thesis described the commissioning of a new COLTRIMS apparatus coupled with a newly installed 100 kHz femtosecond laser system at the James R. Macdonald Laboratory (JRML). This instrument is planned to be used in various pump-probe experiments at JRML, particularly focusing on CEI studies of photochemical processes. The corresponding section of the

thesis briefly outlines the operational principle of COLTRIMS and describes essential components of the newly commissioned setup. This part also includes some preliminary experimental results on laser-induced fragmentation of chloroiodomethane (CH_2ClI) molecules obtained with the new apparatus.

The second part of the thesis focuses on the study of strong-field-induced molecular wave packet dynamics in sulfur dioxide (SO_2) molecules. The experiments described in this section were conducted using an older COLTRIMS instrument coupled with two different femtosecond laser systems, operating at 3 kHz and 10 kHz repetition rates. In these experiments, an intense near-infrared (NIR,800 nm) or visible (400nm) pump pulse was used to trigger wave packet dynamics in SO_2 and SO_2^+, which were probed by a second, more intense NIR pulse that further ionized and/or dissociated the molecule. The information on the time evolution of the created molecular wave packets was deduced by analyzing the delay-dependent yields of several singly, doubly, and triply charged final states of the molecule, as well as the kinetic energies and angular distribution of resulting ionic fragments. For either pump pulse used, we observed clear signatures of both vibrational and rotational dynamics. For the experiments employing the NIR pump pulse, where the delay between the pump and probe pulses ranged from 0 to 2 ps, channel-selective Fourier analysis revealed signatures of bending vibration in both ionic and neutral states of the SO_2 molecules. Fast Fourier Transform (FFT) spectra for all channels showed prominent peaks at the ionic bending vibrational frequency ($\sim 400\ cm^{-1}$), while some channels also displayed a weaker but clearer peak around $520\ cm^{-1}$, reflecting bending vibrations in the ground electronic state of the neutral SO_2 molecule. To reveal the initial direction of the wave packet motion and to characterize the corresponding wave packet phase in both ionic and neutral ground states, we performed the inverse Fast Fourier Transform (IFFT), selecting the corresponding frequency in the FFT spectra.

For the experiments with the 400 nm pump pulse, observed vibrational dynamics have been dominated by the ionic state bending vibrations, reflected by the pronounced FFT peak around $400\ cm^{-1}$. In addition, a weak feature corresponding to the symmetric stretching mode at $1058\ cm^{-1}$ has been observed in the yield of (S^+, O^+, O^+) coincidence channel. No signature of the neutral-state vibrational dynamics has been observed when using the 400 nm pump. For both pump frequencies used, we observed weak but clear impulsive alignment of the molecules by the pump laser pulse, reflected in the time evolution of the angular distributions of the fragments with

respect to (linear) laser polarization. While in both cases the initial alignment deteriorated because of the rotational wave packet dephasing, the time scale of this dephasing was found to be significantly longer for the 400 nm pump pulse (~1.5 ps vs. ~ 0.5 ps for 800 nm pump), most likely because of the narrower distribution of the populated rotational states. In this experiment, where the pump-probe delay window was extended to 20 ps, we also observed a fractional revival of the rotational wave packet.

Finally, for both pump wavelengths, we observed a clear decrease in the amplitude of the oscillations with 400 cm^{-1} frequency at larger delays. For the experiments with the 400 nm pump, where a longer delay window was used, this oscillation was found to be completely suppressed after a few ps. However, for the delay-dependent yield of the doubly charged molecules (SO_2^{++}), we found that this oscillation is partially restored after ~9 ps, clearly visualized by the reappearance of the peak around 400 cm^{-1} in the sliding-window FFT. A similar reappearance has not been found on any other channel so far. While the exact origin of this behavior and its channel specificity remain unclear, this could be a signature of the vibrational wave packet dephasing and subsequent revival - the phenomenon that is well understood in diatomic molecules but is much less studied in larger systems with an additional degree of freedom.

Overall, the work reported in this thesis provides new insights into laser-induced dynamics in triatomic molecules and highlights the power of time-resolved ion spectroscopy, CEI, and channel-selective Fourier analysis for studies of ultrafast molecular processes. With the newly commissioned COLTRIMS setup in combination with the 100 kHz repetition rate of the new JRML laser, the experimental approach used in this work can be efficiently applied to map many light-induced reactions in more complex, chemically relevant systems.

Table of Contents

List of Figures

List of Tables

Acknowledgements

The completion of this work has been only possible with the guidance, support, and encouragement I have received from many individuals around me throughout this journey.

First and foremost, I would like to express my sincere gratitude to my advisor, Professor Artem Rudenko. From the very first day I met him in December 2022, when I was a new student with little experience, to this moment as I stand ready to graduate, the journey of becoming the person I am today has only been possible because of the unwavering guidance, patience, and encouragement of my advisor. I am truly at a loss for words to express how deeply grateful I am to him. His constant belief in me made me feel capable of doing better each day on this research journey. I cannot thank him enough for all the time he spent patiently explaining physics concepts, guiding me through lab work, data analysis, offering feedback and suggestions, providing corrections on my work and projects, encouraging me to participate in conferences and external beamtimes, and always guiding me towards new opportunities that helped me grow both professionally and personally. His unwavering support helped me immensely in reaching every milestone during my time at KSU and in deciding to graduate and move forward with the next chapter of my studies.

I would also like to thank Professor Daniel Rolles and Professor Vinod Kumarappan for serving on my committee and providing invaluable guidance, insights, and feedback on my work. I am deeply grateful to them for generously giving their time whenever I had questions, helping me to understand important concepts, and carefully reviewing my work with thoughtful comments and suggestions, all of which were an immense source of support throughout my journey.

I am also very thankful to all the postdocs and graduate students in our group, who were such an important part of my journey in the department. I feel incredibly fortunate to have had the opportunity to work with these brilliant individuals, who helped me greatly in learning laboratory work and data analysis codes from the very beginning. I truly appreciate everyone who supported me during beamtimes and generously shared their experience and knowledge with me.

I would like to acknowledge Professor Uwe Thumm and his group for providing feedback on the theoretical point of view, and Dr. Charles Fehrenbach, Dr. Cosmin Blaga, and his group for their efforts in maintaining the laser systems and providing their help in keeping them running during our beamtimes. I am also grateful to all the technical staff members, Chris Aikens, Justin

Millette, Scott Chainey, and Vince Needham, for their immense contribution to the James R. Macdonald Lab. Without their time and effort, we would not be able to run our experiments smoothly in the lab.

I am also very grateful to all the faculty members in the Department of Physics at Kansas State University. I feel fortunate to have had the opportunity to learn advanced concepts of physics from such inspiring teachers. My sincere thanks also go to Kim Coy and all the staff members in the department, whose friendliness and willingness to help with all my questions over the years made my life much easier.

I would like to thank all the friends and fellow students I met in the department. Their friendship made this journey far more enjoyable and memorable. My deepest thanks go especially to my five best friends in the Sri Lankan student community, who became my family away from home. Their unwavering support and encouragement have been one of the greatest emotional strengths that have helped me immensely to stay strong and succeed in this journey.

Last but not least, I would like to express my heartfelt gratitude to the dearest members of my family —my father, Dayananda Kudagama, my mother, Nayana Hettiarachchi, and my younger sister, Hiruni Kudagama, back in Sri Lanka. Amme and Thaththe, thank you for all your hard work and sacrifices to give us comfort, a good education, and a beautiful childhood, always making sure that we never experienced hardship. Even though I was the first to move away from our loving home, you made sure I never felt alone. It was never easy to be far away from home, but you were always just one call away, day and night, keeping me company all the time. Without the three of you, I would never have made it this far. I would also like to thank my partner, Sahan Thathsara. You are the most loving and kind person I could ever wish to have in my life. Though we have been miles apart, your sweet voice and encouraging words were my remedy for even the toughest days. Thank you for always being there and patiently waiting for me. I am so excited to see what the future holds for us and our life together.

Dedication

To my parents, my younger sister, and my Sahan!!

Chapter 1 - Introduction

In nature, there are many light-matter interaction processes that are essential to the existence of humans, such as photosynthesis [1], the biosynthesis of vitamin D [2], and O_2 formation in the planetary environment [3],[4]. With the development of science and technology, scientists across many fields, including physics, chemistry, and biology, have become more and more interested in understanding these light-induced molecular dynamics in various quantum systems. Historically, the most common approach to studying many photo-induced processes is examining the initial reactants and final products of a reaction. Even though this approach can provide very detailed information about the reaction of interest, in most cases, it does not provide the full picture of the process. In particular, it does not deliver direct information about different mechanisms and pathways that could lead to the same final state, and is insensitive to (often short-lived) intermediate molecular configurations, their kinetics, etc. It is important to note that many of the processes important for photophysics, photochemistry and photobiology, including light-induced electronic motion [6],[7] and charge transfer processes [5], occur on attoseconds to femtosecond timescales, while vibrational [17],[19] and rotational [54],[55] dynamics in bound molecules, molecular bond breaking and forming [8], [9] may take place over tens of femtoseconds to picoseconds. Therefore, obtaining information on molecular dynamics involved in these types of photoprocesses requires experimental tools that can resolve changes in molecular structure on corresponding ultrafast timescales.

A breakthrough in studying ultrafast processes, which triggered a wide range of time-resolved measurements, was achieved by Ahmed Zewail, who was awarded the Nobel Prize in Chemistry in 1999 [10],[11] for the development of a new subfield called *femtochemistry*. This was achieved by developing methods to incorporate femtosecond laser systems into various types of measurements. The advancement of ultrashort laser pulses ranging from infrared to vacuum ultraviolet (VUV) and the recent development of X-ray Free Electron (XFEL) lasers, which produce intense and ultrashort X-ray pulses, provided researchers with a variety of tools needed to investigate photo-induced molecular dynamics in real-time [12],[13],[14].

The most common experimental approach for performing time-resolved measurements is based on a pump-probe concept. In this technique, the first (pump) light pulse initiates the dynamics (i.e., a photochemical reaction of interest), providing the initial start time (t_0) for

clocking the reaction. Then a second pulse, known as the probe, which arrives at various times (t) after the pump pulse, investigates the temporal evolution of the system. This time difference is referred to as the pump-probe delay, denoted as $\Delta t = (t_0 - t)$. As an example of such a pump-probe measurement, by recording a series of snapshots of molecular geometry at a variable pump-probe delay (Δt), one can generate a "molecular movie" to illustrate nuclear dynamics of a photochemical reaction [25].

This two-pulse method can be combined with different schemes for probing evolving molecular structure. One of the promising methods focusing on the positions of the nuclei is the so-called Coulomb Explosion Imaging (CEI) technique, initially introduced by Vager et al [26], to determine the static geometry of molecules. CEI is based on the fast removal of electrons from molecules, leading to their breakup into charged fragments following such rapid ionization [15], [25]. [26]. The information on molecular geometry is then contained in the momentum vectors of the created ionic fragments, which can be detected in coincidence. To be successful, the CEI technique requires that the ionization process is fast compared to the molecular dynamics of interest, such that the geometry changes during this process can be neglected. In Vager's original work, CEI was realized by sending a fast ion beam through a thin foil to strip off electrons. However, nowadays, with the advancement of short-pulse laser technology, high-intensity optical and free-electron lasers are widely used to ionize the molecules and initiate CEI [16], [18]. Use of femtosecond laser pulses enables employing CEI as a probe method in a pump-probe experiment, which opens the way for time-resolved studies of light-induced molecular dynamics.

Over the years, the CEI technique in combination with a pump-probe scheme has been successfully employed to probe vibrational dynamics in diatomic and small polyatomic molecules [16], [19], to study rotational wave packet dynamics induced by the laser alignment [20], and to visualize molecular dissociation [49]. A typical experimental approach to studying molecular dynamics using CEI is to measure the momenta of the ions produced during laser-induced fragmentation processes. The method for measuring the complete 3D momenta of the detected fragments is known as "momentum spectroscopy" [21],[22], and the experimental setups capable of measuring the 3D momentum vectors of multiple charged particles (such as ions and electrons) in coincidence are sometimes called reaction microscopes (REMIs) [21]. These instruments are typically based on the ion momentum measuring technique known as COLTRIMS (COLd Target

Recoil Ion Momentum Spectroscopy), [21], [22]. The main goal of this work is to advance COLTRIMS applications for studying ultrafast molecular dynamics.

More specifically, this thesis focuses on two main aspects: technical and scientific. The first part of the thesis describes the commissioning of the new COLTRIMS setup for the newly installed 100 kHz laser system, a project in which I have actively participated at the James R. Macdonald Laboratory (JRML) at Kansas State University since 2024. The second one, which contains the main scientific results of this work, focuses on the channel-selective analysis of strong-field-induced nuclear wave packets in a sulfur dioxide (SO_2) molecule. As a triatomic, asymmetric top, bent molecule, SO_2 has been widely used as one of the prototypes for investigation of atmospheric chemistry over the past few years, due to its role in the efficient formation of neutral and ionic molecular oxygen [3], [19], [23], [24]. SO_2 molecules are one of the extensively found molecules in planetary environments. The experiments described in this thesis have been conducted using three different femtosecond laser systems available at the JRML.

The thesis document is organized as follows. Chapter 2 provides an introduction and essential concepts to understand the strong field-induced molecular dynamics. Chapter 3 focuses on the commissioning of the new COLTRIMS setup. Besides covering the key concepts and working principles of COLTRIMS, signal generation, and data acquisition of the new setup, this chapter includes a brief description of the laser systems used to generate ultrafast femtosecond near-infrared (NIR) and visible pulses used in this work. The data on SO_2 molecules were collected using a different COLTRIMS setup, which will be briefly described at the end of Chapter 3. Chapter 4 presents the experimental results on SO_2, addressing strong field induced molecular dynamics, Coulomb explosion (CE) and dissociative ionization (DI) processes, identification of different fragmentation pathways, their corresponding Fast Fourier Transforms (FFT) and inverse FFT (IFFT). Finally, Chapter 5 summarizes the work presented and provides a brief outlook for future directions.

Chapter 2 - Theory

2.1 Franck-Condon Principle and Transition Probability

With the development of new quantum mechanics and the introduction of wave and particle duality nature of electrons by Louis de Broglie, in 1926, Erwin Schrodinger proposed his theory of wave mechanics by describing electrons as standing waves that surround the nuclei.

$$H(r,R)\psi\,(r,R) = E\psi\,(r,R) \tag{2.1}$$

where *r* is the position of all electrons and *R* is the position of all nuclei.

The above equation is identified as the time-independent Schrodinger equation with $H\,(r,R)$ is the total Hamiltonian and the $\psi\,(r,R)$ is the total wavefunction. The total Hamiltonian consists of the contributions of the kinetic energies of the electron (T_e) and nuclei (T_n), potential energies due to coulombic repulsions between electrons (V_{ee}), between nuclei (V_{nn}), and the attractive forces between electrons and nuclei (V_{en}).

$$H(r,R) = T_e(r) + T_n(R) + V_{ee}(r) + V_{nn}(R) + V_{en}(r,R) \tag{2.2}$$

In the case of fixed nuclei, which do not move in space at a distance *R*, T_n=0. $V_{nn}(R)$ is a constant in the solution of the electronic wave function. These approximations reduced the total Hamiltonian to the electronic Hamiltonian.

$$H_{ele}(r,R) = T_e(R) + V_{ee}(r) + V_{en}(r,R) \tag{2.3}$$

Then the electronic eigenfunction for a molecule that satisfies the electronic Schrodinger equation is given by

$$H_{ele}(r,R)\psi_n^{ele}\;(r,R) = E_n^{ele}(R)\psi_n^{ele}\,(r,R) \tag{2.4}$$

where n is the electronic quantum number.

Max Born and Robert Oppenheimer proposed a method called Born-Oppenheimer (BO) Approximation in 1927 to derive the wavefunction of molecular systems. Since the motion of the nuclei is slower compared to the electron motion, the BO approximation states that electrons can immediately change their distribution. This allows the nuclei and electrons to be mathematically treated independently. By varying the position of nuclei, we can calculate the electric energy of a molecule $E_n^{ele}(R)$ as a function of R, to construct the Potential Energy Surface (PES) of a given molecule [29].

Molecular energy is approximated to be the summation of the electronic, vibrational, and rotational energies, while the total wavefunction ψ is approximated as the product of

wavefunctions corresponding to these three types of motion. Then the intensity of a transition between two states of the total wave function ψ'' (lower state) and ψ' (upper state) can be derived by the square of the corresponding transition moment R_{fi}, given by

$$R_{fi} = \int \psi'^{*}\, M\, \psi'' d\tau \tag{2.5}$$

where M is the total dipole moment. Dipole moment M can be written as the summation of electric and nuclear components as

$$M = M_e + M_n \tag{2.6}$$

Since most of the spectrum is not rotationally resolved, by ignoring the rotational wavefunction and applying the BO approximation, the total wavefunction of the nuclear system can be written as a product of ψ_e and ψ_v, the electronic and vibrational wavefunction, respectively.

$$\psi = \psi_e(r, R)\psi_v(R) \tag{2.7}$$

Hence, the transition moment for the two vibronic states can be derived as,

$$R_{fi} = \int \psi_e'^{*}\, \psi_v'^{*}\, (M_e + M_n)\psi_e''\, \psi_v''\, d\tau_e d\tau_n \tag{2.8}$$

By replacing $d\tau_n$ with dR, since the nuclear wave function depends only on the internuclear distance R, and considering that the nuclear dipole moment (M_n) depends solely on R because it is independent of the electrons coordinates, the transition moment can be simplified due to the orthogonality of the electronic wave functions of different electronic states, as follows.

$$R_{fi} = \int \psi_e'^{*}\, \psi_v'^{*}\, M_e\, \psi_e''\, \psi_v''\, dr dR = \int \psi_e'^{*}\, M_e\, \psi_e''\, dr \int \psi_v'^{*}\, \psi_v''\, dR \tag{2.9}$$

The first integral of the transition moment R_{fi} corresponds to the electronic transition moment. The square of the second integral (or the overlap integral) determines the relative intensities of different vibrational bands of the molecular system.

The Frank-Condon Principle states that during the electronic transition, the instantaneous internuclear distance and the velocity of the nuclei can be considered to remain unchanged, resulting in no significant change in the nuclear configuration of the molecule. This happens because nuclei are heavier than electrons, and electronic transitions in a molecule happen faster than the vibrational motion of the nuclei.

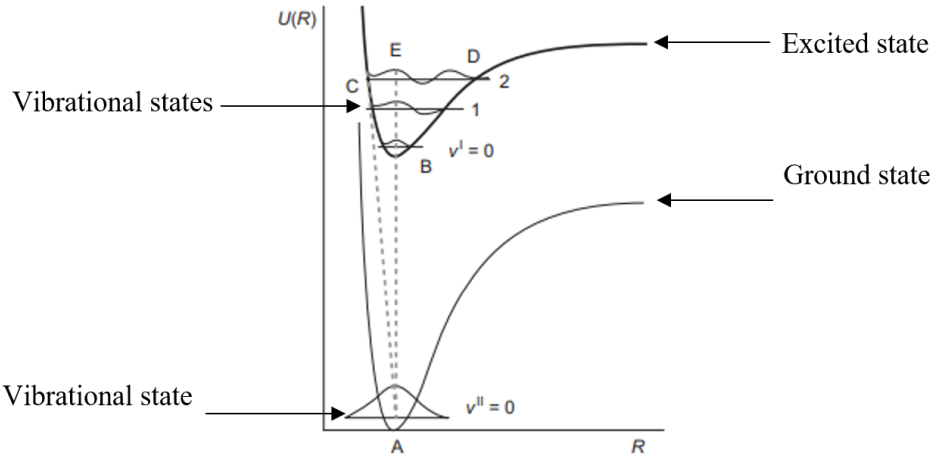

Figure 2.1 Visualizing the Frank-Condon principle using potential energy curves. Adapted from [30].

According to our previous discussion, we saw that the probability of transition between two vibrational states v' and v'' depends on the Frank-Condon factor $[\int \psi_v'^* \, \psi_v'' \, dr]^2$. Therefore, the magnitude of the overlap between the two states depends on the shape of the eigenfunctions ψ_v. Figure 2.1 shows the different vibrational states in two electronic states. According to these PECs, for v=0, the distribution function is a bell-shaped curve, while for other vibrational levels, the distribution functions consist of broad maxima at or near the classical turning points, which mainly contribute to the integral overlap. The smaller minima or maxima observed between the classical turning points make very little contribution to the overlap integral [30]. Thus, according to the Frank condition, the distribution of probability density maximizes at the middle point for the v=0 level and near the turning points of higher vibrational energy levels of the system with electronic states lying at approximately the same internuclear distance [30]. The most intense and probable vertical transition without any change in the position or velocity of the molecular motion can be visually shown in a PEC by vertical lines. According to Figure 2.1, the most intense and probable vertical transition happens between A to B, (0,0), while transitions from A to C require a change in the internuclear distance, and A to E require a change in kinetic energy.

In 1925, Franck discussed different levels of intensity distributions found in the vibrational structure of electronic bands due to vibronic (simultaneous occurrence of both vibrational and electronic) transitions.

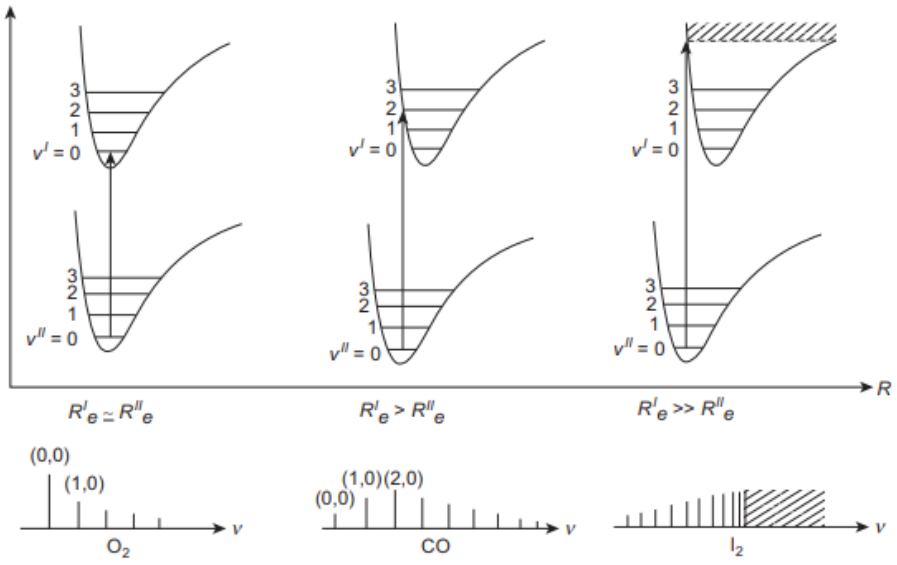

Figure 2.2 Representation of different intensity distributions in vibrational fine structure of electronic spectra according to the Frank-Condon Principle. R is the internuclear distance [30].

Depending on the shape and the equilibrium internuclear distance of the potential energy of the two electronic states involved in the transition, there are three types of intensity distributions observed in nuclear systems. As shown in Figure 2.2 (a), when the upper electronic state and the lower electronic states have the same equilibrium internuclear distance, according to the FC principle, the vertical transitions are observed with the most intense spectral line corresponding to $v'' = 0$ to $v' = 0$ transition. When the potential energy curve of the upper electronic state shifts towards larger R values as in Figure 2.2 (b), the most intense spectral line with maximum overlap integral is observed only when the wave function corresponds to the upper vibrational level (i.e. $v' = 2$) has either a minimum or a maximum and lies vertically above the maximum of the wave function of $v'' = 0$ state [30]. The transitions to the other higher and lower v'states are less likely to occur. The last scenario is where the upper electronic state is at a considerable R distance away from the lower state, as shown in Figure 2.2 (c). Here, the most probable transition can happen from $v'' = 0$ to a state with very large values of v', which might be a continuum state as well [30]. Therefore, if the excited molecule energy is high enough, it is more likely for molecules to dissociate (fragmentation of a bound molecule upon absorption of one or more photons) [31] without any vibrations.

2.2 Wave packet dephasing and revival

Due to the anharmonicity of the potential well, the vibrational energy levels, which are not equally spaced, will evolve over time with slightly different phases. Hence, the initially localized wave packet will lose its coherence and spread out over the potential well. This phenomenon is known as "dephasing" of the vibrational wave packet. However, since the energy levels are quantized (discrete nature) and due to the periodicity of the phases of different vibrational components and smaller anharmonicity [57], after a certain characteristic time, the phases can realign, resulting in the wave packet being re-localized. This is a purely quantum mechanical phenomenon known as "revival".

The evolution of the time-dependent wave packet $\psi(x,t)$, which is a coherent superposition of vibrational eigenstates, can be expanded in terms of a Fourier expansion of energy eigenfunctions (φ_n) with quantized energy eigenvalues (E_n) [50].

$$\psi(x,t) = \sum_{n=0}^{\infty} a_n \varphi_n(x) e^{-\frac{iE_n t}{\hbar}} \tag{2.10}$$

where a_n is their corresponding overlap integral with the $n = 0$ state with the initial wave packet following the initial transition at time t=0

$$a_n = \int_{-\infty}^{+\infty} [\varphi_n(x)]^* \psi(x,0) dx \tag{2.11}$$

The autocorrelation function $A(t)$, which described the overlap between the time-dependent quantum state ($|\psi_t>$) with the initial state ($|\psi_0>$) can be evaluated in either position or momentum space to give

$$A(t) \equiv (<\psi_t|\psi_0>) \tag{2.12}$$

For $|A(t)|$ to be large, the wave function at later times must have significant overlap with the initial state in both x and p-space [50]. The most common useful form for the $A(t)$ for initially highly localized wave packets, can be derived in terms of the square of the overlap integral as,

$$A(t) = \sum_{n=0}^{\infty} |a_n|^2 e^{+\frac{iE_n t}{\hbar}} \tag{2.13}$$

The energy of a localized wave packet that is excited with an energy spectrum tightly spread around a large central value of the quantum number n_0 be expanded as [50]

$$E_n = E(n_0) + E'(n_0).(n-n_0) + \frac{E''(n_0)}{2}.(n-n_0)^2 + \frac{E'''(n_0)}{6}(n-n_0)^3 + \cdots \tag{2.14}$$

where $E'(n_0) = (\frac{dE_n}{dn})_{n=n_0}$ and so on. Then the time-dependence of each quantum state is given by

$$exp\left(\frac{-iE_n t}{\hbar}\right) = exp\left(\frac{-i}{\hbar}\left[\begin{array}{c} E(n_0)\, t + (n-n_0)\, E'(n_0)t + \frac{1}{2}.(n-n_0)^2 E''(n_0)t + \\ \frac{1}{6}.(n-n_0)^3 E'''(n_0)t + \cdots \end{array}\right]\right) \quad (2.15)$$

Other than the first term, which is n independent, all other terms in the expansion correspond to an important characteristic time scale. In this study, we are mostly interested in the second derivative term, which defines the revival time of the wave packet as [50],

$$T_{rev} = \frac{2\,\pi\,\hbar}{|E''(n_0)|/2} \quad (2.16)$$

The energy eigenvalues of a harmonic oscillator are given by

$$E_n = \hbar\omega\left(n + \frac{1}{2}\right) \quad and \quad n = 0,1,2.. \quad (2.17)$$

In this expression, E_n (measured in Joules) includes the zero-point energy ($E_n = 1/2\,\hbar\omega$).

In a more specific case, for the Morse potential (or anharmonic oscillator), the customary energy level expression (G_v) measured in cm^{-1} can be written as, [56]

$$G_v = \frac{E_v}{hc} = \omega_e\left(v + \frac{1}{2}\right) - \omega_e x_e\left(v + \frac{1}{2}\right)^2 + \cdots (\text{higher order terms}) \quad (2.18)$$

where v is the vibrational quantum number, ω_e is the fundamental vibrational frequency, x_e is the first-order anharmonicity constant, and c is the speed of light (in cms^{-1}).

Then the energy expression E_n in Equation 2.15 can be rewritten in terms of G_v as

$$exp\left(-\frac{iG_v t(hc)}{\hbar}\right) = \exp\left(-iG_v t(2\pi c)\right) = \exp\left(-i2\pi c[G(v_0)\, t + (v-v_0)\, G'(v_0)t + \frac{1}{2}.(v-v_0)^2 G''(v_0)t + \frac{1}{6}.(v-v_0)^3 G'''(v_0)t + \cdots]\right) \quad (2.19)$$

Then the revival time (in ps) becomes,

$$T_{rev} = \frac{2\,\pi}{2\,\pi c\omega_e x_e} = \frac{1}{c\omega_e x_e} \quad (2.20)$$

From equation 2.18, we can derive an expression for the anharmonicity ($\omega_e\chi_e$), associated with the spacing between the adjacent energy levels, which also corresponds to the vibrational

transition frequency. Since the $G(v)$ and $G(v+1)$ are the energy level expressions of the vibration level v and $v+1$, the energy difference between these levels gives the vibrational frequency corresponding to $v+1 \leftarrow v$ transition [56]. A new label $\Delta G_{v+\frac{1}{2}}$ was incorporated to express this difference, as it is centered halfway between the two levels at $v+\frac{1}{2}$, measured in (cm^{-1}).

$$\Delta G_{v+\frac{1}{2}} = G(v+1) - G(v) = \omega_e - 2\omega_e\chi_e(1+v) \tag{2.21}$$

$$\omega_e.\chi_e = \frac{\left[\Delta G_{(v+1)+\frac{1}{2}}\right] - \left[\Delta G_{v+\frac{1}{2}}\right]}{2} \tag{2.22}$$

Since this picture neglects any coupling to different modes and coupling for rotations, we can estimate the revival time of a vibrational wave packet of a molecule (T_{rev}) using half of the vibrational level spacing, which is inherited due to the anharmonicity of the potential curve of the electronic state.

We should also note that the wave packet also reforms near the half-revival time ($T_{rev}/2$), with the original classical periodicity, but half a period of phase with the initial wave form [50]. The approximate revival at $T_{rev}/2$ can, in fact, be somewhat better than at the full revival time T_{rev} since the higher-order anharmonicities have had less time to affect the phase structure of the revivals [59].

2.3 Laser Ionization Processes

The experiments carried out during this work are based on the ionization of molecules by intense femtosecond laser pulses. In this thesis, we will, in general, refer to these ionization processes as Strong Field Ionization (SFI), implying all ionization processes induced by an intense electromagnetic field of the laser pulse.

During light-matter interaction, if the energy of a photon absorbed by the molecule is larger than its ionization potential I_p, then the molecule AB in its ground state can be ionized to its cation AB^+. This process is defined as "photoionization" or "single-photon ionization" and can be described as,

$$AB + \hbar\omega \rightarrow AB^+ + e^- \tag{2.23 a}$$

where ħω is the energy of the photon. If the energy of the photon is smaller than the ionization potential ($\hbar\omega < I_p$), ionization would require absorption of more than one photon and can be described as

$$AB + n\hbar\omega \rightarrow AB^+ + e^- \qquad (2.23\ b)$$

where *n* is the number of photons absorbed. This process is normally referred to as "multiphoton ionization" and requires higher light intensity than single-photon ionization.

To distinguish different photoionization processes observed in strong electromagnetic fields, L.V. Keldysh introduced the so-called adiabaticity (Keldysh) parameter, γ, in 1965 [27], [28], [33]. The Keldysh parameter is defined as the ratio between the field-free ionization potential (I_p) and the ponderomotive energy of a free electron oscillating in the laser field (U_p)

$$\gamma = \sqrt{\frac{I_p}{2U_p}} \qquad (2.24)$$

U_p is defined by

$$U_p = \frac{e^2 E_0^2}{4 m_e \omega_{laser}^2} = 9.338 \times 10^{-14} I \left[\frac{W}{cm^2}\right] \lambda^2 [\mu m]^2 \qquad (2.25)$$

where E_0 is the maximum electric field strength of the oscillating field, which depends on the intensity of the laser. ω_{laser} is the frequency of the oscillating field. m_e is the mass of the electron, and e is the absolute value of charge.

Figure 2.3 shows three types of photoionization processes observed in different regimes of light-matter interactions. Figure 2.3 (a) corresponds to the single-photon ionization process that can be observed whenever the photon energy exceeds the ionization potential of the system. Figure 2.3 (b) corresponds to multiphoton ionization, where ionization happens through simultaneous absorption of multiple photons. This can be considered as an extension of the single-photon ionization that happens at high laser intensities when the photon energy is smaller than (I_p).

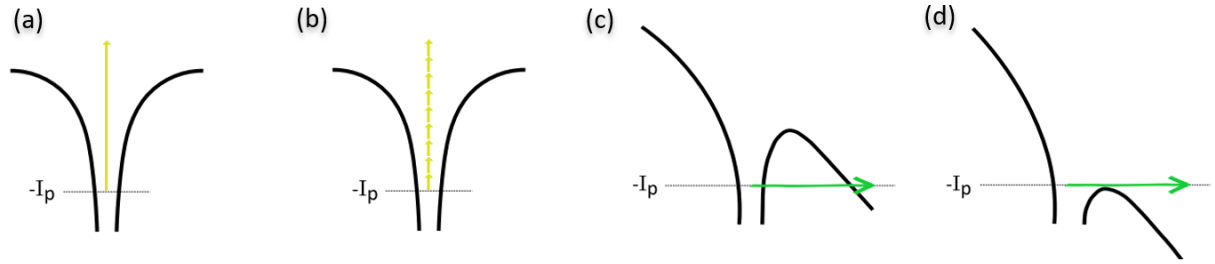

Figure 2.3 Photoionization processes in different regimes of light-matter interactions (a) single, ionization, (b) multi-photon ionization, (c) tunneling ionization, and (d) over the barrier ionization [33].

In the case of intense laser light, instead of considering the interaction as a stream of discrete photons, we can adopt the electromagnetic wave perspective. In this representation, the strong laser field can significantly distort the atomic Coulomb potential, as shown in Figure 2.3 (c). This distortion lets the electron tunnel through the lowered barrier, resulting in tunneling ionization. The extent to which an electromagnetic field modifies the atomic potential can be quantified using the Keldysh parameter γ. For multi-photon ionization, $\gamma \geq 1$, while for tunneling ionization, $\gamma \leq 1$ [28],[33].

Finally, at even higher laser field strength, the Coulomb barrier can be completely suppressed, such that the ground state is no longer bound, as shown in Figure 2.3 (d). This regime is known as over-the-barrier ionization (OBI) [58]. The critical intensity at which the field strength becomes high enough for OBI can be estimated by

$$I_{OBI} = \frac{\pi^2 c \epsilon^3 I_p^4}{2Z^2 e^6} = 4 \times 10^9 \, I_p^4 \, Z^2 \quad \left[\frac{W}{cm^2}\right] \tag{2.26}$$

where I_p is the ionization potential, and Z is the charge state of the relevant ion or atom [58]. It should be noted that more elaborate calculations as well as numerical approaches show that this simple expression underestimates the critical intensity for OBI, and the ionization probability reaches unity only at the intensities well above I_{OBI} [65].

There are many cases when the absorbed energy of light is high enough to result in both dissociation and ionization of the molecule. In that case, the process is called "dissociative ionization" and, within the multiphoton picture for a diatomic molecule, can be described as,

$$AB + n\hbar\omega \rightarrow AB^+ \rightarrow A^+ + B + e^- \tag{2.27}$$

In this case, the molecule can either be directly ionized to one of the dissociative excited cationic states or can first be ionized to a bound (e.g., ground) cationic state and then promoted to a higher-lying dissociative state by absorbing additional photon(s). In both cases, the molecule will eventually dissociate by creating ionic and neutral fragments. The dissociation dynamics of such pathways strongly depend on the shape of the potential energy surfaces (PES) of the initial ground state of the neutral molecule and the ionic states populated during ionization.

If the laser intensity is high enough, it is also possible to remove two or more electrons from the molecule, resulting in its double or multiple ionization. If the resulting multiply charged state (AB^{m+}) is repulsive; the system rapidly breaks up into ionic fragments due to the electrostatic repulsion. This process is called the "Coulomb Explosion (CE)" of the molecular ion. For the double ionization of diatomic molecules, it can be represented as

$$AB + n\hbar\omega \rightarrow AB^{2+} + 2e^{-} \rightarrow A^{+} + B^{+} + 2e^{-} \tag{2.28}$$

2.4 Coulomb Explosion Imaging (CEI)

As discussed in Chapter 1, Coulomb Explosion Imaging (CEI) is a widely used imaging technique to study molecular structure and dynamics described by the time evolution of nuclear wave packets through the pump-probe method [15], [26], [32], [34]. In laser-driven CEI, by exposing the target molecules to an intense ultrashort laser pulse, the absorption of multiple photons results in the least bound valence electrons from the molecules being ejected during the rapid ionization process. Hence, the bound parent ion breaks up into fragment ions due to the CE, and the resultant fragment kinetic energies depend on the charge of the ions and the separation between each of them. If we assume an instantaneous ionization process to the purely Coulombic final state, the energy released in such a breakup can be readily estimated based on the Coulomb law. The following equations show the energies expected under these assumptions for two and three-body CE breakup processes.

$$E_{12} = \frac{1}{4\pi\varepsilon_0}\frac{q_1 q_2}{r_{12}} \quad for\ two-body\ breakup \tag{2.29 a}$$

$$E_{123} = \frac{1}{4\pi\varepsilon_0}\left[\frac{q_1 q_2}{r_{12}} + \frac{q_2 q_3}{r_{23}} + \frac{q_1 q_3}{r_{13}}\right] for\ three-body\ breakup \tag{2.29 b}$$

As shown in Figure 2.4 for an example of a pump-probe experiment, where CEI is used to probe the dynamics in the ground cationic state of a diatomic molecule, the first arriving pulse (the pump) induces the process we want to study and launches a nuclear wave packet that evolves in time on the bound electronic state AB^+. Then, the probe pulse arriving at a variable time delay induces strong field ionization of the molecular ion to a repulsive dicationic state, which finally Coulomb explodes into charged fragment ions A^+ and B^+.

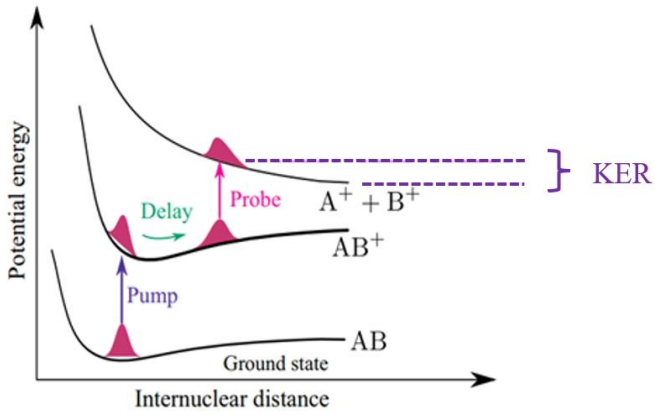

Figure 2.4 Representation of the pump-probe process in a diatomic molecular system (AB). Adapted from [35].

Cold-target recoil ion momentum spectroscopy is a coincidence momentum imaging technique that is used to study the laser-induced dynamics of molecules. By measuring the time-of-flight and hit position information of the detected ions, this method enables us to compute the complete three-dimensional momenta of all fragment ions created during the laser molecular interaction. These complete 3D momenta of the fragment ions can be used to reconstruct the instantaneous structure (using the bond angles and bond lengths) of the molecule before the CE. It is important to note that the accuracy of the reconstructed molecular structure using CEI mainly depends on the validity of the Coulomb approximation (which assumes the interaction between fragment ions is only by the Coulomb repulsion) and on the change in the molecular geometry during the multiple ionization process [34]. More details of COLTRIMS and momentum measurement will be discussed in Chapter 3. Using the measured complete 3D momentum vectors and employing the momentum and energy conservation laws, we can calculate the kinetic energies (KE) of each fragment ion and the kinetic energy release (KER), the sum of the kinetic energies

of all ions corresponding to a particular breakup pathway. Equations from (2.30 a) to (2.31 b) are described in the scenario illustrated in Figure 2.4

$$KE_A = \frac{m_B}{m_A + m_B} KER \tag{2.30 a}$$

$$KE_B = \frac{m_A}{m_A + m_B} KER \tag{2.30 b}$$

where

$$KER = \frac{1}{2} m_A V_A^2 + \frac{1}{2} m_B V_B^2 \tag{2.31 a}$$

$$m_A V_A = -m_B V_B \tag{2.31 b}$$

The total KER mainly depends on the internuclear distance between the fragment ions and the final dissociative state. Therefore, sometime after dissociation and CE, the separation between the two ions becomes significantly larger, which results in a decrease in the KER. This can be observed in the delay-dependent KER spectrum, which enables us to identify different dissociative states after ionization and to track the movement of the molecule over the time delay. More details of the momentum calculations and observed molecular structure and dynamics will be discussed in Chapter 4.

2.5 Rotational Dynamics and Impulsive Alignment of Molecules

Due to the interaction between the polarizability of the molecules and the laser field, molecules can be aligned by a laser pulse. For femtosecond laser pulses, the duration of the pulse τ is typically much shorter than the rotational period of the molecule, T_{rot}, which is on the picosecond scale. In a pump-probe experiment with sufficiently intense pump pulses at optical frequencies, the pump pulse initiates rich rotational wave packet dynamics. The initial rotational wave packet is a broad, coherent superposition of discrete rotational eigenstates of a molecule, which depends on the parameters of the pump pulse and the temperature of the molecular target [55]. After the impulsive excitation by the pump pulse, the created rotational wave packet evolves under field-free conditions [54]. It typically exhibits a pronounced initial alignment peak, which can rapidly dephase because of the large spread of rotational frequencies. Depending on the type of molecule, one can observe periodic revivals of the molecular alignment [53]. For linear molecules, the full revivals occur at an integer number of the fundamental rotational period T_{rot}, and the pronounced half-revivals and, in curtained cases, quarter-revivals can also be observed.

Since the interaction of intense probe pulses with molecules depends on molecular alignment, an understanding of the rotational dynamics mentioned above is crucial for interpreting the results of pump-probe experiments. Usually, in the pump-probe scheme, the time evolution of the rotational wave packet and the degree of alignment are characterized by a time-dependent parameter $< cos^2\theta >$, known as "molecular alignment parameter". Here θ is the angle between the molecular axis and the polarization of the laser field.

$$< cos^2\theta > = \frac{1}{4\,\pi}\int_0^{2\pi} d\Phi \int_0^{\pi} cos^2\theta\, sin\theta\, d\theta = \frac{1}{3} \tag{2.32}$$

When $< cos^2\theta >$ is 1/3, molecule has no alignment, which implies a completely random, isotropic spatial distribution of the molecules. $< cos^2\theta >$ =1 implies perfect alignment of the molecule along the laser polarization axis. Hence, any value of $< cos^2\theta >$ ranging from 1/3 to 1 indicates that the net alignment of the molecules is along the laser polarization axis, while $< cos^2\theta >$ less than 1/3 implies that the molecules are preferentially aligned perpendicular to the laser polarization axis, with $< cos^2\theta >$ reaching 0 for perfect anti-alignment of the molecules. Experimentally, $< cos^2\theta >$ can be deduced from the measured angular distributions of the fragment ions resulting from CE of the molecule (assuming the validity of the so-called axial recoil approximation, which implies that the molecule breaks up before any change in the initial orientation of the fragmenting bond occurs [61]).

Chapter 3 - Experimental Methods

Experimental studies of femtosecond molecular dynamics, which are the main subject of this work, are based on two main components: an ultrafast femtosecond light source and an ion momentum spectrometer. This chapter provides a brief overview of femtosecond laser systems employed in this work, describes the commissioning of the new Cold-Target Recoil Ion Momentum Spectrometer (COLTRIMS) to be used with the new 100 kHz laser, and includes a brief description of the older COLTRIMS setup that was used for the experiments on sulfur dioxide molecules discussed in the next chapter.

.

3.1 Femtosecond laser systems employed at JRML

3.1.1 Prairie Ultrafast Light Source for Attosecond Research (PULSAR)

PULSAR is the oldest of all femtosecond lasers currently operational at the JRML. It is a customized version of a commercial Red Dragon laser system designed by KM Labs. In brief, PULSAR is a Ti: Sapphire laser operating at 10 kHz with a maximum pulse energy of 2 mJ, generating linearly polarized near-infrared pulses with a central wavelength of approximately 790 nm and a pulse duration of about 28 fs. Further details can be found elsewhere [36],[43],[44].

3.1.2 Femtosecond LAser for Multicolor Experiments (FLAME)

The FLAME laser is a commercial Legend Elite Duo laser system developed by Coherent, Inc. As PULSAR, FLAME is also a Ti: Sapphire laser system. It has a central wavelength of approximately 800nm, pulse energy of up to 5 mJ, pulse duration of 30 fs, and a repetition rate of 3 kHz. More detailed information about the FLAME laser system can be found in [37].

3.1.3 “Konza”: a new 100kHz laser system for JRML

The high-power femtosecond laser technology behind the newly built Konza laser at the JRML is based on the so-called optical parametric chirped pulse amplification (OPCPA). In OPCPA, the principles of laser chirped-pulse amplification (CPA) are combined with optical parametric amplification (OPA), enabling the amplification of ultrashort femtosecond pulses while maintaining both high pulse energies and high repetition rates [38].

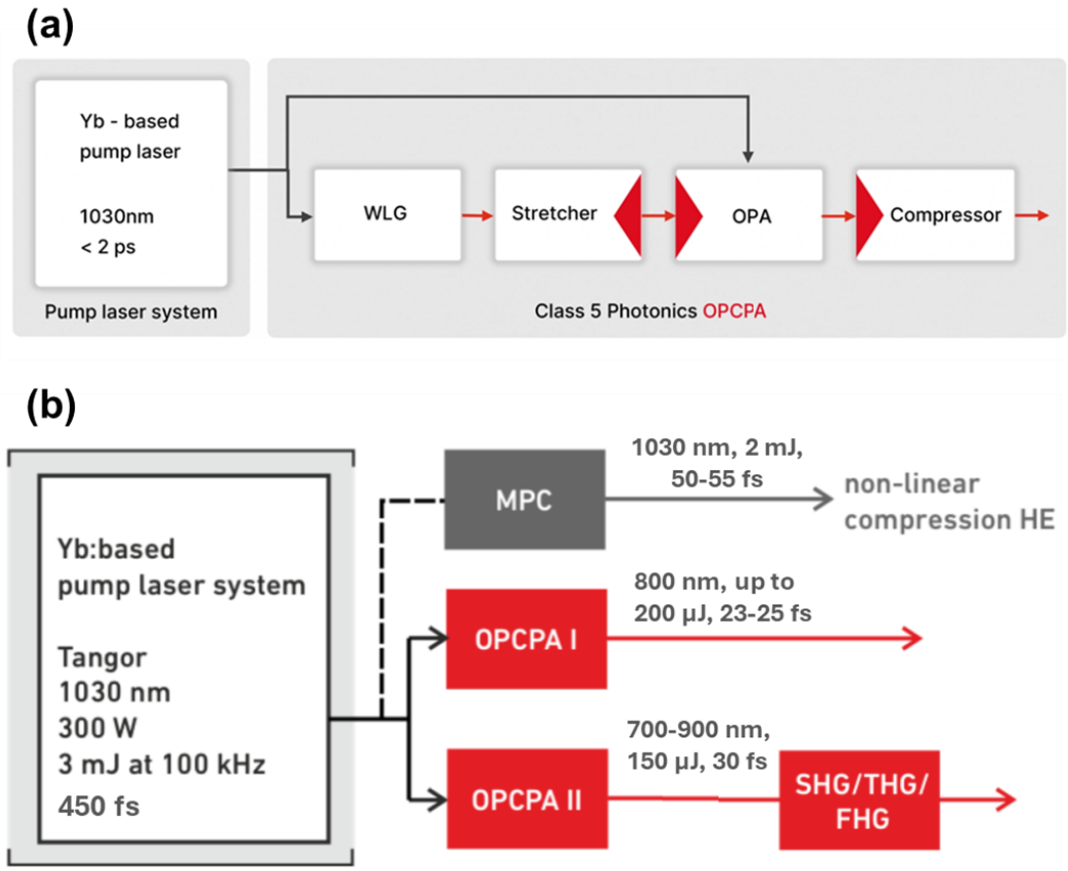

Figure 3.1 (a) Basic layout of the Class 5 Photonics OPCPA [38]. (b) JRML White Dwarf HE OPCPA with two synchronized OPCPA channels. Alternatively, the pump laser fundamental can be used directly after the non-linear compression with a multi-pass cell (MPC).

As sketched in Figure 3.1 (a), a fraction of the pump pulse energy is directed towards white light generation (WLG) to produce a broadband seed pulse for the subsequent amplification stages. A stretcher is employed to optimize the bandwidth and ensure the temporary overlap between the seed and pump pulses. The seed pulse is then amplified in an optical parametric amplifier (OPA), and the amplified pulse is subsequently compressed to its Fourier transform limit using a compressor.

Konza is a multiple-output laser system designed by Class 5 Photonics for JRML. As sketched in Figure 3.1 (b), it consists of a commercial Yb-based Tangor 300 pump laser from Amplitude (central wavelength 1030 nm, pulse energy > 3 mJ, pulse duration ~450 fs, repetition rate 100 kHz), a multi-pass cell (MPC) for non-linear compression of the Tangor output (resulting in 50-

55 fs pulses with >2 mJ per pulse), and a dual-output White Dwarf OPCPA system pumped with Tangor, with synchronization between the two channels of < 3 fs rms. The White Dwarf system generates two OPCPA outputs:

- High Energy (HE) OPCPA 1 (central wavelength 800 nm, pulse energy ~180-200 μJ, pulse duration 23-25 fs), and
- Tunable OPCPA 2 (central wavelength 700–900 nm, pulse energy ~100-120 μJ, pulse duration ~30 fs).

The Konza system also includes modules to generate second, third, and fourth harmonics from the output of the tunable arm (although only the second harmonic generation module is currently operational). All components of the laser system operate at a repetition rate of 100 kHz [37].

3.2 Commissioning of COLd- Target Recoil Ion Momentum Spectrometer (COLTRIMS) for 100 kHz Konza laser.

In general, a COLTRIMS apparatus combines a supersonic gas jet used to produce well-localized and internally cold targets with an electrostatic flat-field spectrometer for ions, enabling ion momentum measurements with resolution far below 1 atomic unit (a.u). COLTRIMS is often combined with electron detection in a configuration sometimes called a “reaction microscope”. Such instruments can detect both electrons and ions on a large solid angle, reaching 4π for low-energy particles. During my graduate studies, a new reaction microscope / COLTRIMS setup to be used in combination with the new 100 kHz Konza laser described above was acquired from Roentdek Handels GmbH and installed at JRML. While both electron and ion detectors have been tested, only the ion detection setup has been fully commissioned so far. Therefore, the discussion below mainly focuses on the measurements of ionic fragments with COLTRIMS.

In COLTRIMS, the central concept is the coincidence detection of fragments (ions, electrons, or both), in which the information on each detected fragment is recorded and stored for each laser shot, enabling very detailed characterization of molecular dynamics upon different interactions.

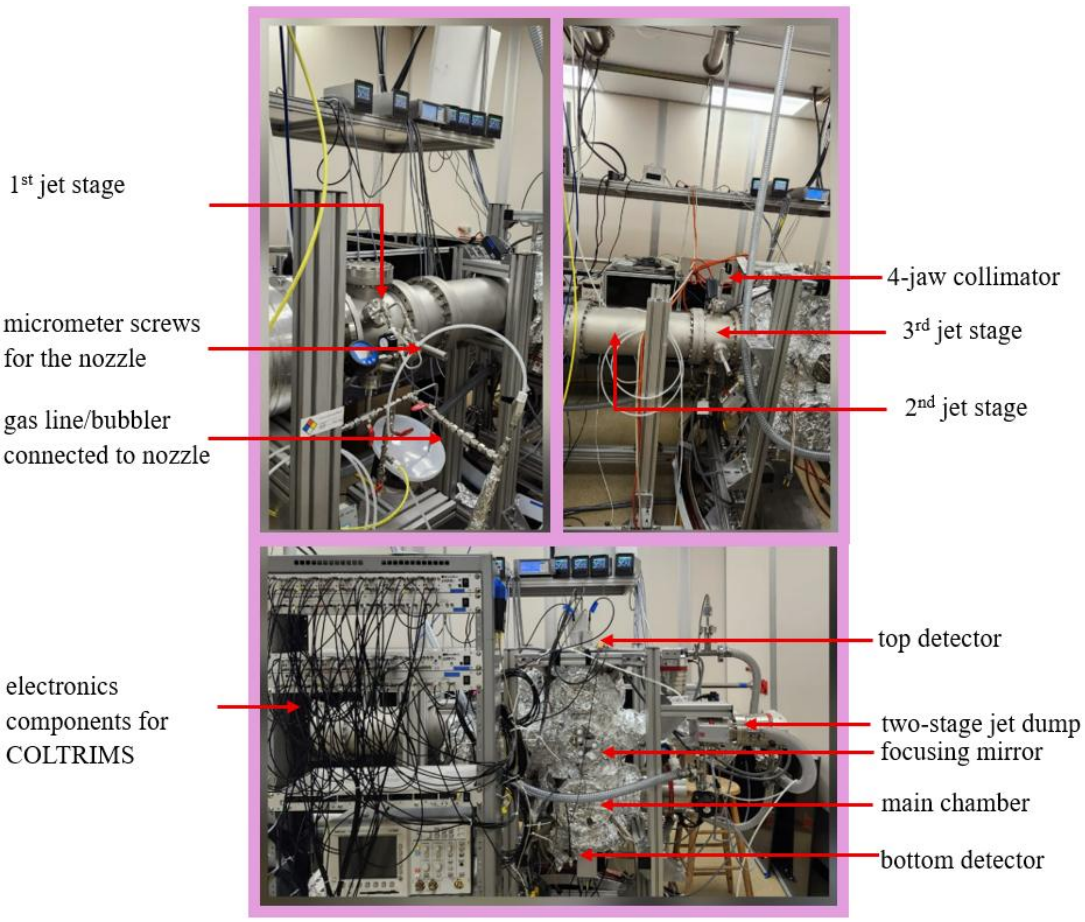

Figure 3.2 COLTRIMS experimental setup area in the Konza Lab at JRML, KSU

To detect all charged fragments (ions and/or electrons) that originate from the same molecule (i.e., the same reaction event) while avoiding "false coincidences", where some of the detected particles originate from two different target molecules or the residual gas, only one laser-molecule interaction per laser shot must be allowed. To achieve this condition in the experiment, a dilute supersonic gas jet, an ultrahigh vacuum environment, and tight focusing of laser beams play a crucial role. These components, as well as the spectrometer, delay line detector, and data acquisition system used in the new COLTRIMS apparatus, will be discussed in detail below. Figure 3.2 shows the photograph of the experimental area for the newly commissioned COLTRIMS setup, which depicts some of the components mentioned above.

3.2.1 Main components of the newly commissioned COLTRIMS setup.

3.2.1.1 Vacuum System

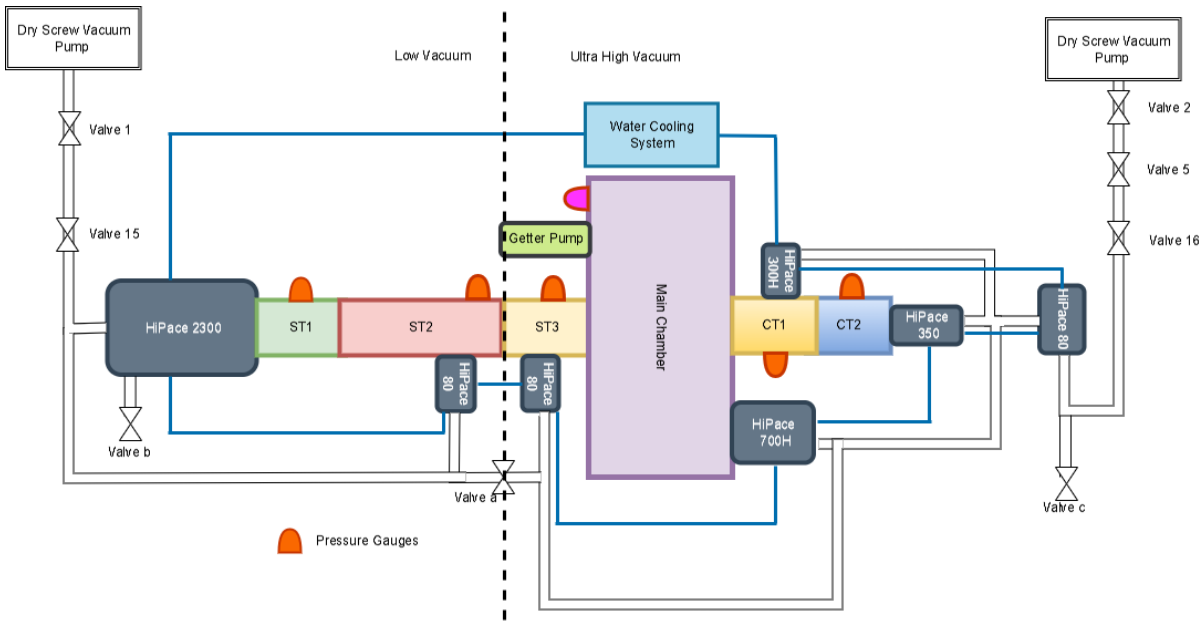

Figure 3.3 Schematic of the vacuum system, including pumps and chambers.

In COLTRIMS, maintaining ultrahigh-vacuum conditions in the reaction chamber is crucial to prevent a single laser pulse from triggering multiple fragmentation or ionization events, which can lead to false coincidence. If the pressure in the reaction chamber is too high, residual gas molecules in the chamber may interact with the laser pulses and generate unwanted background fragments. Quantitatively, for high-intensity laser pulses, for which the ionization probability in the focus of the pulse is saturated, avoiding false coincidence requires having less than one residual gas molecule in the laser focal volume. To achieve a sufficiently high vacuum inside the reaction chamber, the experimental setup incorporates several differentially pumped stages between the jet nozzle and main chamber, as well as two differentially pumped jet dump stages, here named “catchers”. Figure 3.3 presents the layout and components of the vacuum system for the COLTRIMS setup, including the three-stage jet system for delivering an atomic or molecular target.

There is one big turbomolecular pump, Pfeiffer HiPace 2300, attached to the jet side, to pump the high gas load of the first stage chamber. The second and third stage chambers are individually pumped by two Pfeiffer HiPace 80 turbo molecular pumps. The main chamber is pumped by a Pfeiffer HiPace 700H turbo pump and by the SAES Getters, S.p.A. getter pump systems. Lastly, the first and second stages of jet dump chambers are pumped out by Pfeiffer HiPace 300H and Pfeiffer HiPace 350 turbo molecular pumps, respectively. Valve "a" separates the high gas Stage 1 and 2 regions from the rest of the ultra-high vacuum regions. This is open only when we are pumping out the system and keep it closed during normal operations.

We measure the pressure using three types of ion gauges from Agilent Technologies: the FRG-730 (Full-range Pirani Bayard-Alpert gauge), which is connected to the first and second stages; the X3004-04401, connected to the third stage and the first and second jet dumps; and the X3004-04402, connected to the main chamber. All HiPace turbo pumps coupled with the COLTRIMS are connected to a water-cooling system, allowing water to circulate through the pumps continuously. This process makes sure that pumps can operate effectively to maintain stable pressure levels throughout the system. Initially, the rapid air removal process inside the system is achieved by employing all turbo pumps backed by two dry Screw vacuum pumps (Oerlikon Lybold Vacuum: WHU4400-DV650S) connected through the high-load valve (V1) and high-vacuum valve (V2). The high gas line is connected through valve 15 to the dry screw pump. The ultra-high vacuum lines are all pumped out through another HiPace 80 turbo molecular pump connected to the second dry screw vacuum pump through valve 16. Valve 5 is a fast-acting emergency valve. Valve b and c are two pump-out (or leak check) ports for the COLTRIMS setup. Baking the main chamber and the jet dump up to ~120-130 °C helps to reach a good high vacuum and minimize residual gases in the reaction chamber as well. Under the current ultra-high-vacuum condition, we can reach a pressure inside the main chamber as low as 4.5×10^{-11} Torr.

3.2.1.2 Supersonic Gas Jet

To achieve high resolution in momentum spectroscopy measurements, a well-localized, cold atomic or molecular gas target is essential. This is because the typical recoil-ion momenta are often in the order of (or smaller than) the thermal momentum spread at room temperature. A well-localized cold jet can be generated utilizing the concepts of adiabatic supersonic expansion of the target gas. For coincidence measurement, a low-density supersonic gas jet plays a crucial role in maintaining the condition of only one molecule interacting with a single laser pulse in the interaction region. Figure 3.4 illustrates the main components we used in our system to achieve a well-localized cold molecular jet.

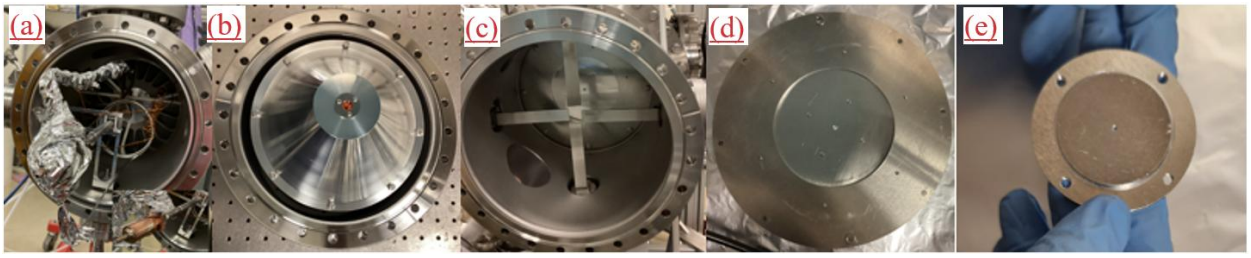

Figure 3.4 Components of the gas jet. a) nozzle (60 μm), b) first skimmer (0.3 mm), c) 4-jaw aperture (collimator), d) second skimmer (0.3 mm), and e) 1 mm aperture at the entrance of the main chamber.

When the incoming gas at a pressure of several bars expands through a small nozzle into a low-pressure region (~10^{-6} - 10^{-7} torr), the gas molecules reach a velocity greater than the speed of sound in the medium. This phenomenon defines the “supersonic” gas jet. It is also important to note that when the gas expands through the nozzle, in the ideal case, it would expand isotropically (freely) in all directions. However, this ideal condition is only possible to achieve if the pressure beyond the nozzle is exactly zero. Therefore, when the gas jet propagates further from the nozzle, its outer regions begin to interact with the residual gas molecules. These interactions result in a disturbed flow, slowing down the expansion. In contrast, the central part of the jet, restricted by the so-called barrel shocks on the sides and by the Mach disk, a shock wave that forms perpendicularly to the jet propagation direction, maintains a cooler and more collimated flow [64]. This well-preserved core region is often referred to as the “zone of silence”, where the gas molecules propagate at supersonic speeds in a nearly collision-free regime. To ensure that only this cold, central portion of the jet is used, it is crucial to extract it by placing the first skimmer

within the “zone of silence”. Further propagation of the target beam is shaped using a carefully designed sequence of skimmers, collimators, and apertures.

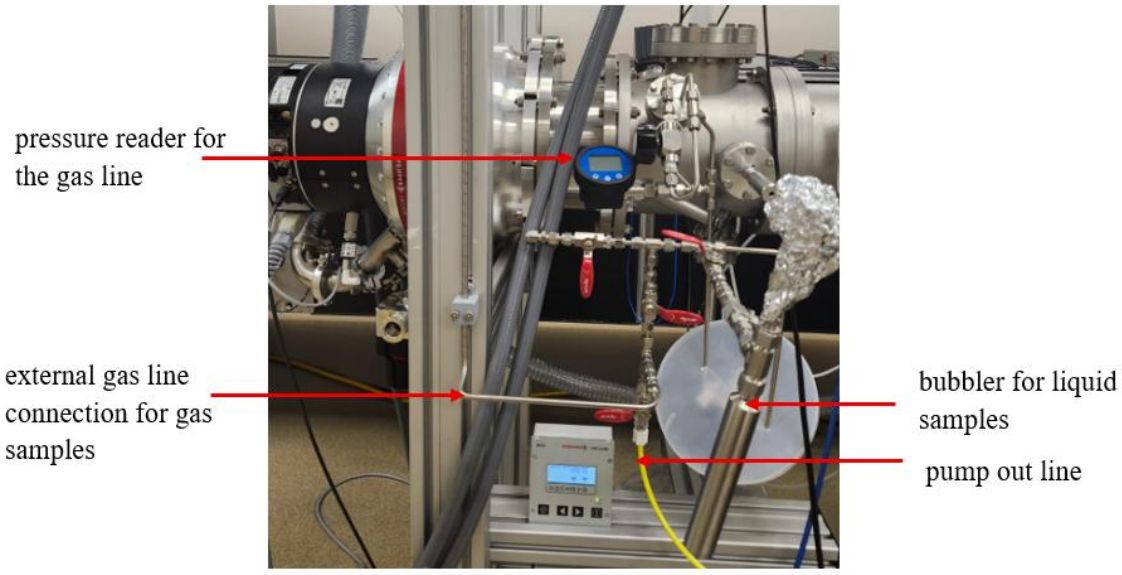

Figure 3.5 Image of the gas line, which connected to the nozzle from the inside, and a bubbler or gas bottle outside.

As shown in Figure 3.4, the gas jet system begins with a nozzle (containing a small filter tablet inside) with a diameter of 60 µm, which is attached to the gas line (Figure 3.5) connected to the gas cylinder located outside the chamber. There are two micrometer screws mounted outside the jet source, allowing fine adjustment of the nozzle position along the x and y axes. The first skimmer, with a diameter of 0.3 mm and its tip facing the nozzle, is mounted on the flange that separates the first and second vacuum stages. The skimmer tip is positioned approximately 8 mm from the nozzle tip, within the “zone of silence”. Inside the second stage (jet extension), before the second skimmer (also with a diameter of 0.3 mm), there is a 4-jaw slit set with 4 adjustable micrometer screws. This aperture serves as a collimator to narrow the gas jet as required. Finally, a 1 mm aperture is installed at the entrance of the main chamber to select only the central part of the gas jet before it enters the interaction region. This aperture also ensures that sufficiently low pressure can be maintained in the interaction region when the gas jet is operated with high backing pressure.

3.2.1.3 Focusing Mirror

To align and focus the laser beam (propagating along the x-axis) onto the thin cold gas jet (propagating along the y-axis), a focusing mirror with a focal length of 7.5 cm is mounted in the main chamber. The incident laser beam enters the main chamber through a 1 mm-thick CaF_2 window. The focusing mirror must be carefully adjusted so that the reflected beam precisely overlaps with the incident laser beam, ensuring proper focusing on the interaction region. During this alignment process, it is also important to check the count rate, detector image, and time-of-flight spectrum to verify that the focused laser beam is hitting the cold jet at the optimized back-focusing mirror position.

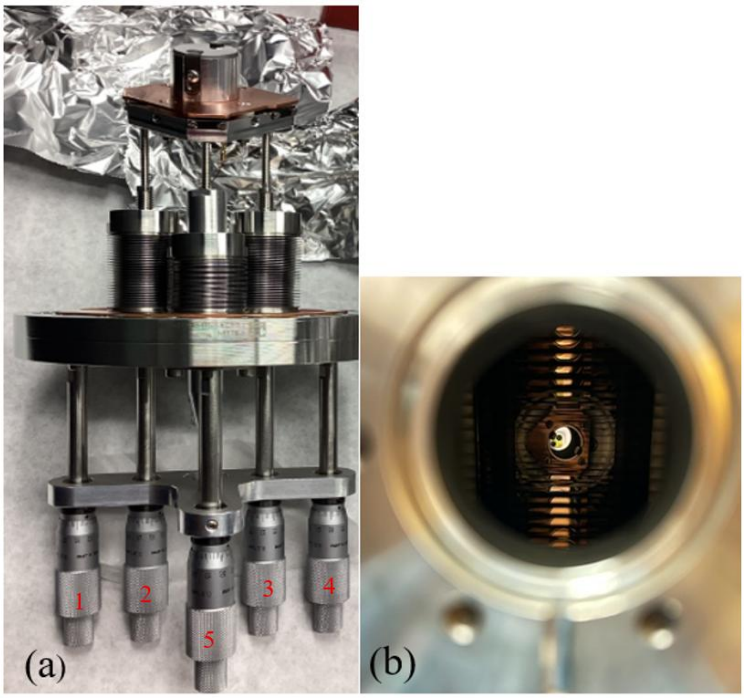

Figure 3.6 Images of the focusing mirror of focal length 7.5cm. (a) Mount the focusing mirror with five dedicated micrometer screws. (b) Image of the focusing mirror taken from the side of the entrance window of the laser.

The focusing mirror is mounted on a stage with three spring systems controlled by five micrometer screws, as shown in Figure 3.6 (a). The two outer screws, 1 and 4, allow us to move the mirror diagonally along the jet, while screw 2 and 3 enable us to tilt the mirror surface as needed. The mirror can move horizontally by moving the screw 5 independently. Moving the screw 1,4, and 5 simultaneously allowed the mirror to move along the laser beam direction (into and out of the interaction region).

3.2.1.4 Spectrometer

When the dilute molecular beam interacts with the laser beam at the interaction region, a homogeneous electric field is required to guide the resulting fragment ions towards the detector. Figure 3.7 illustrates the spectrometer configuration (vertical) used in our COLTRIMS setup. The total length of the spectrometer from the top mesh to the bottom mesh is 31.8 cm. The lengths of the short (electron) and long (ion) sides are 7 cm and 24.8 cm, respectively. The spectrometer consists of standard copper (Cu) plates, as well as a specially designed set of Cu plates near the area where the focusing mirror is mounted. All copper plates are electrically connected in series by 1 MΩ resistors from the top mesh to the bottom mesh. In the configuration used for the experiment in this thesis, the applied electric field is oriented to direct fragmented ions downward, toward the bottom detector. The voltages associated with the top and bottom meshes are chosen based on the target sample, ensuring that all fragment ions can be detected over a full 4π solid angle and optimal momentum resolution.

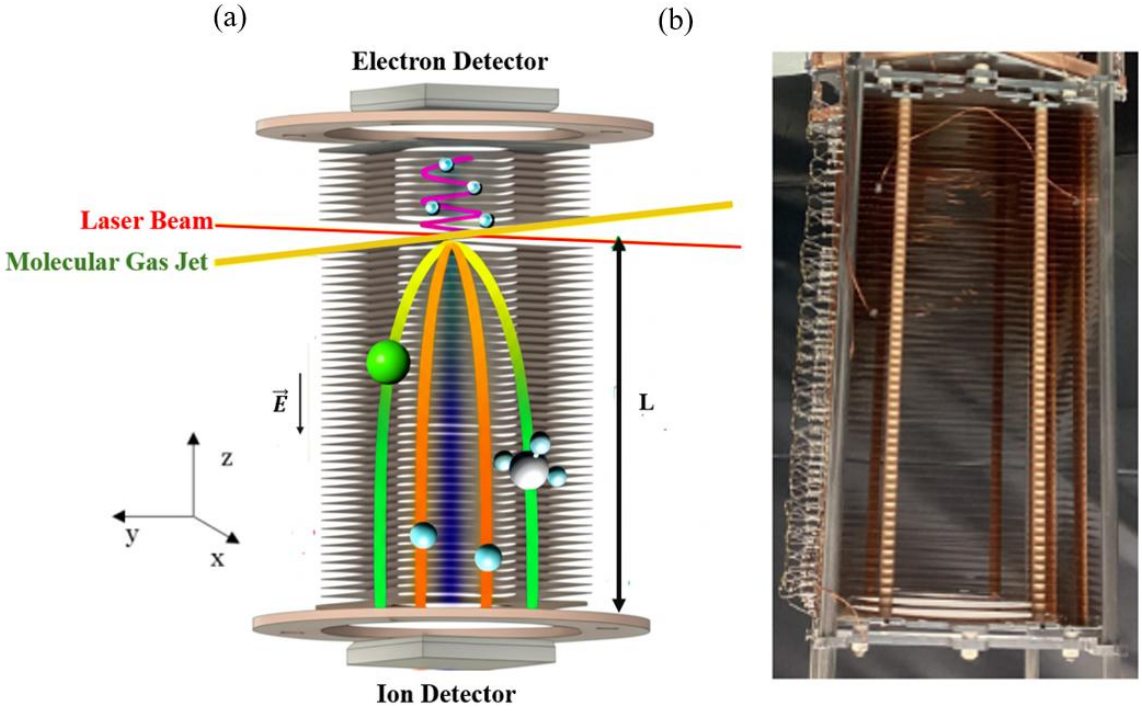

Figure 3.7 COLTRIMS spectrometer. (a) Schematic of the Spectrometer with ions and electrons trajectories. (x-axis is the laser beam direction, y-axis is the molecular gas jet direction, and z-axis is the electric field direction) (b) Image of the spectrometer (including Cu plates, ceramic rods, mounting frames with meshes, and resistors with clamps)

3.2.1.5 Ion and Electron Detectors

In the COLTRIMS main chamber, there are two RoentDeck time- and position-sensitive detectors placed at two ends of the spectrometer. These detectors are high-resolution imaging and timing devices that consist of microchannel plates (MCPs) and delay-line detectors (DLDs) designed to measure the 3D momentum vectors of detected fragment particles. In the COLTRIMS setup for the Konza laser, the top detector consists of a triple-stack (Z-stack) of MCPs with a diameter of 120 mm, while the bottom detector consists of the chevron MCP configuration and funnel MCP as the front plate with a diameter of 75 mm. Both detectors are equipped with three hexagonal delay-line anodes for two-dimensional position readout. Since the chevron configuration consists of MCPs of different resistances, it requires a resistance-matching shim ring to be placed between the front and back MCPs in the bottom MCP stack. As shown in Figure 3.8, the ion detector is attached to the bottom of the spectrometer for ion detection.

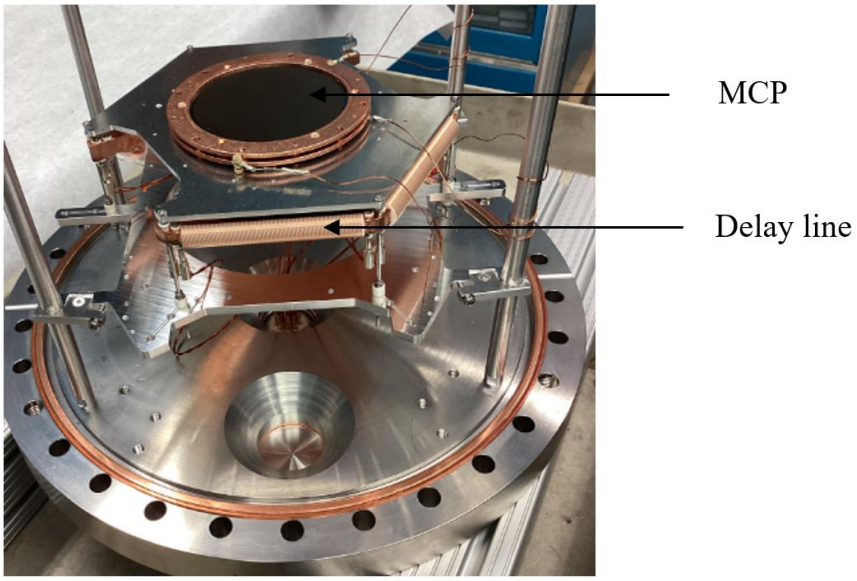

Figure 3.8 Image of bottom delay-line detector including Chevron MCPs stack and a 3-layer hexagonal delay-line anode.

Microchannel Plates (MCP)

The MCP is a circular glass plate used to detect ions, electrons, VUV rays, X-rays, and gamma rays in a vacuum environment by amplifying the detected signals. As shown in Figure 3.9, when a single fragment strikes the channel wall of the front plate of the MCPs stack, electrons

are emitted. These ejected electrons will then be accelerated by a static electric field generated by the voltages applied to the front and back of the MCP stack, along the channels in the plate, producing even more secondary electrons in a process known as electron avalanche. The glass capillary channels on the MCPs are made with a bias angle perpendicular to the Microchannel plate surface, preventing electrons from passing straight through the glass channels without hitting the wall. By the time ejected electrons reach the rear side of the MCPs stack, they produce a measurable electrical pulse containing time information of the incident particles. The bottom detector of this COLTRIMS setup consists of a set of MCPs with a diameter of 75 mm arranged in a chevron configuration with millions of micro-diameter glass capillary channels, which act as a secondary electron multiplier.

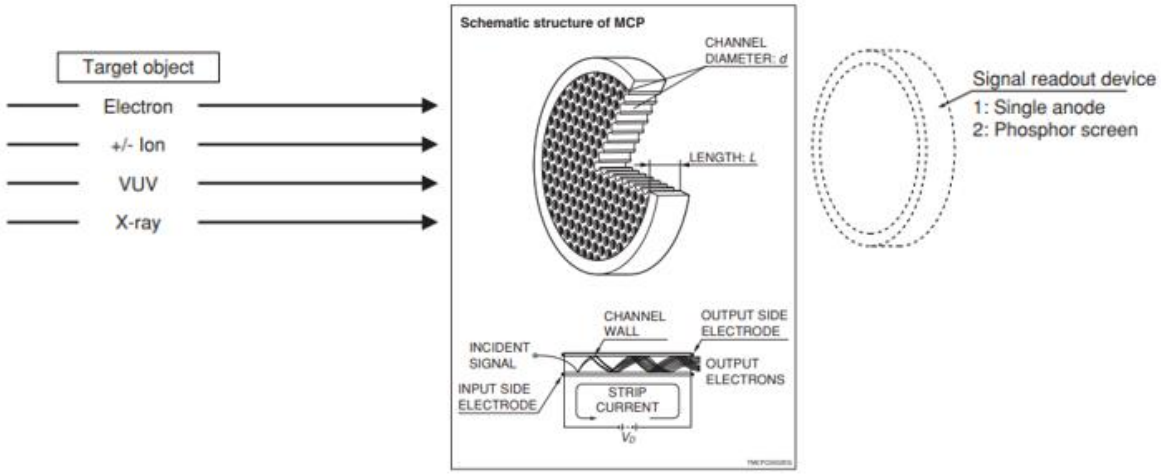

Figure 3.9 Schematic structure of the MCP. Adapted from [39]

The timing signal for each ion hit is collected from the front side of the MCP and measured using a single metal anode connected as the readout. Simultaneously, the 2D position information of the ion impact can be extracted from the delay-line anode connected to the back of the MCPs stack. The time of flight (TOF) of each ion is determined by measuring the impact time on the front MCP (t_{mcp}) with the trigger signal from the photodiode ($t_{trigger}$), as follows:

$$TOF = \left(t_{mcp} - t_{trigger}\right) \tag{3.1}$$

Delay Line Anode (DLD)

Unlike the standard two-layer DLD anode, which has only two perpendicular wire layers (x and y), the Hexanode we used in our system consists of three layers of helically wound wires (u, v, and w), each mounted at a relative angle of 60^0 to the others. Each layer consists of two parallel wires, a signal wire, which is kept at a more positive (+50V) potential than the reference wire. Keeping the two wires at slightly different voltages results in the electron signal being induced only in the signal wire, while electronic noise is generated in both wires.

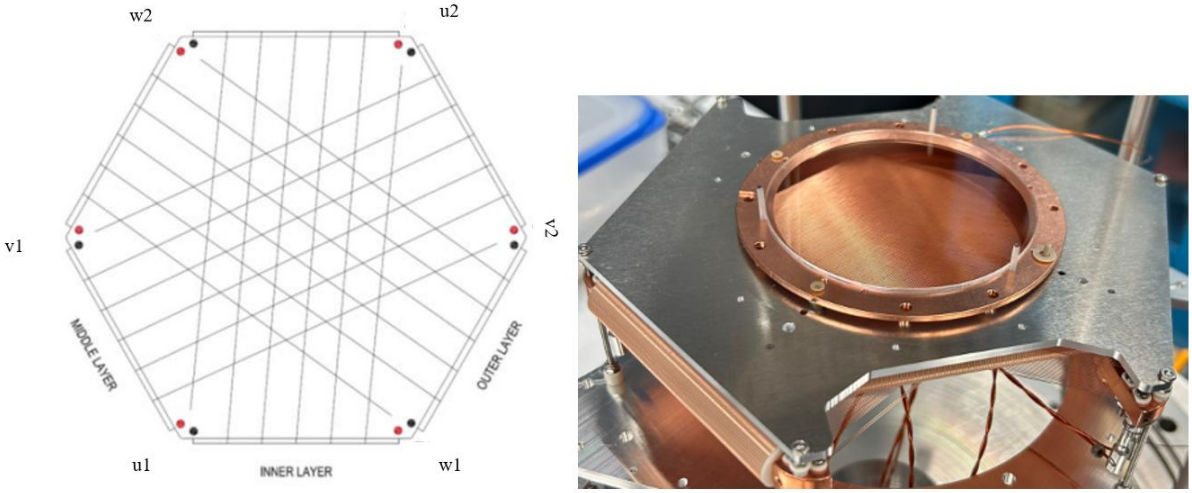

Figure 3.10 (a) Orientation of x, y, and z wire pair terminals on anode corners viewed from the rear side [40]. (b) Hex-DLD stack used for ion detection in the Konza COLTRIMS.

Later, by subtracting the signal in the reference wire from that on the signal wire, we can eliminate the unwanted electrical noise induced in the wires. Compared to a regular two-layer configuration (used in PULSAR COLTRIMS), the three-layer configuration significantly reduces the effective dead time for multi-hit events by allowing reconstruction of closely timed multi-particle events.

The electrical pulse generated by the hex-anode upon the ion hits the delay line wires will propagate towards the two ends of each wire. Then these electrical pulses of each wire will have two traveling times. If the arrival time at the two ends of a wire is t_1 and t_2 , the hit position information of an ion along the signal wire can be derived by taking the difference as follows [62],

$$Hit\ position = \frac{1}{2}\frac{V_{group}^{i}}{D_{1mm}}\ (t_1 - t_2) + O \qquad (3.2)$$

$$\text{“Time to position conversion factor”} = \frac{V_{group}^{i}}{D_{1mm}}$$

where V_{group}^{i} are the propagation speeds of signals in each direction along the wires (note that they are slightly different for each wire), D_{1mm} represents the distance signal travels along a wire to achieve 1mm movement. O is an offset value, which is a function of connection cable lengths and cable lengths up to TDC, which needs to be recalibrated whenever these parameters are changed.

Since the Hexanode has three delay line wires, positions on each layer, in the directions u, v, and w, can be determined as follows [40].

$$u = \frac{1}{2}\frac{V_{group}^{u}}{D_{1mm}}\ (t_{u1} - t_{u2}) \tag{3.3 a}$$

$$v = \frac{1}{2}\frac{V_{group}^{v}}{D_{1mm}}\ (t_{v1} - t_{v2}) \tag{3.3 b}$$

$$w = \frac{1}{2}\frac{V_{group}^{w}}{D_{1mm}}\ (t_{w1} - t_{w2}) + O \tag{3.3 c}$$

The sum of the total travel time of the two signals along each wire to the ends, which depends on the length of the wire, should be constant. This condition can be used to eliminate false events by keeping the time sum of detected events within a small time interval. The Hexanode's coordinate frame u, v, and w can be converted into a Cartesian coordinate (X,Y) by the following equations using only two of the hexagonal hit position coordinates.

$$X_{uv} = u + O_x \tag{3.4 a}$$

$$Y_{uv} = \frac{1}{\sqrt{3}}(u - 2v) + O_y \tag{3.4 b}$$

$$X_{uw} = X_{uv} \tag{3.4 c}$$

$$Y_{uw} = \frac{1}{\sqrt{3}}(2w - u) + O_y \tag{3.4 d}$$

$$X_{vw} = v + w + O_x \tag{3.4 e}$$

$$Y_{vw} = \frac{1}{\sqrt{3}}(w - v) + O_y \tag{3.4 f}$$

Where O_x and O_y are arbitrary offsets. More detailed information about Hex DLD can be found in the MCP Delay Line detector manual from Roendeck [40].

3.2.2 Data Acquisition.

Both the time of flight and the hit positions of all the fragment ions detected are obtained from the signals of the front MCP and the DLA, respectively. These components are placed inside the main chamber under high vacuum. Therefore, it is important to make sure all the cable connections, from detectors to flanges inside the chamber and from the outer flanges to electronics, are made properly before the COLTRIMS chamber is closed. The following flow chart shows how the cable connections from the outer flanges to the electronics are made.

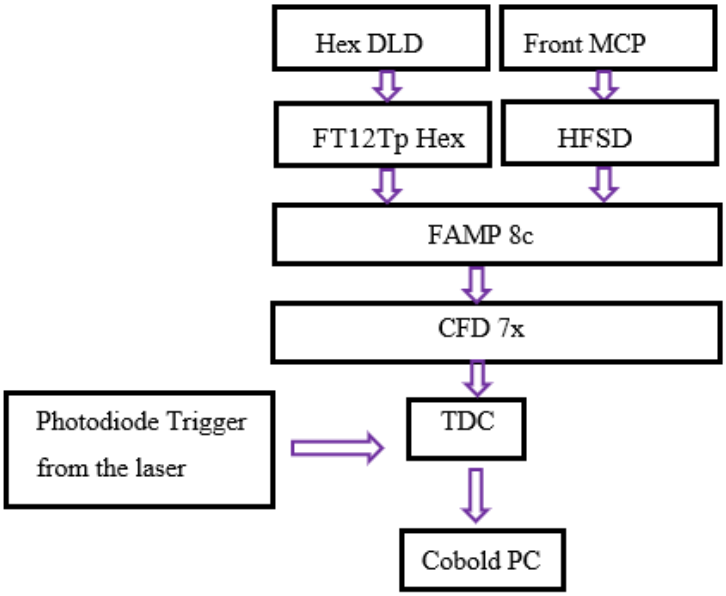

Figure 3.11 The flow chart illustrates the cable connection of the electronics for the bottom ion detector.

There are thirteen signals initially collected from the bottom detector, where twelve signals are from the Hex DLD, corresponding to u1, u2, u3, u4, u5, and u6 signal and reference channels, and one signal from the front MCP. The MCP signal passes through the high-frequency signal decoupler (HFSD), and all twelve Hex DLD signals are connected to the feedthrough signal decoupler (FT12TP Hex). FT12TP Hex will take the difference of the signal and reference wires to eliminate noise and filter only the signal corresponding to each of the six channels. All seven high-frequency signals are amplified using FAMP8c bipolar amplifier units.

All seven negative outputs of FAMP8c are then connected to the CFD7x, Constant Fraction Discriminator, to identify the signal arrival times of all 7 signals. The CFD circuit is a combination of two parts: “analogue circuit”, which produces a bipolar signal from a unipolar input signal

(FAMP8c), and a resistor-divider circuit, which splits the signal into two with different pulse heights (CFD fraction). The pulse height ratio can be set by adjusting the fraction ratio setting of the potentiometer.

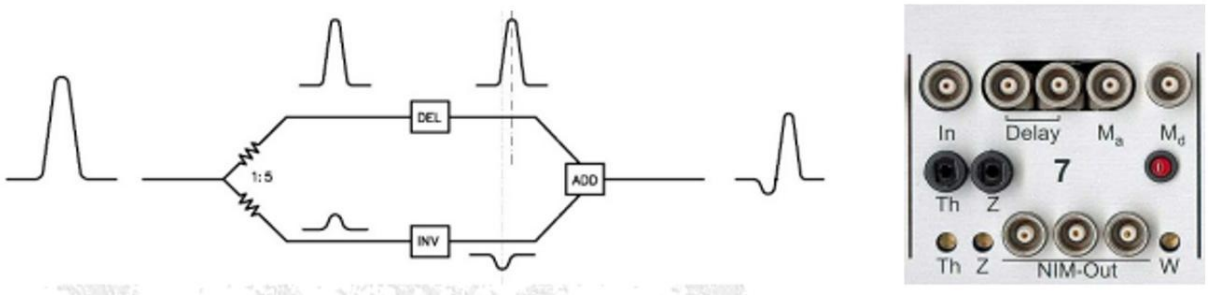

Figure 3.12 (a) Schematics of a CFD analogue chain. (b) Front panel input of CFD [41]. Roendeck CFD units require negative input signals on the "In" socket and provide three digital output signals, "NIM-Out". The input signal pulse height should be more than -100mV and should not exceed -2V for good temporal resolution.

As described in Figure 3.12, in the divided CFD input signal, one of the pulses is inverted while the other pulse is delayed. In our setup, the delay is introduced by an external coax cable (LEMO 00 series) of 80 cm length (corresponding to 4 ns delay) connected between the two sockets labeled "Delay" on the front panel. Later, these two pulses are superimposed again to form the bipolar signal. The bipolar signal can be observed using an oscilloscope by connecting the signal from the analogue walk monitor output socket labelled "Ma". For optimal operation of the CFD units, there are two other parameters called "Threshold level (Th)" and "Walk level (Z: Zero Crossing Level)", which require optimal settings. It is important to set the threshold level above the electronic noise but low enough to get even the smallest valid input signals. The walk level should be set closer to and slightly above the baseline level of the signal. A thumb rule for the relationship between CFD delay (D) and the CFD fraction (f) is given by

$$D = RT(1 - f) \tag{3.5}$$

where RT is the pulse rise time defined as the time from reaching 10% to 90% of the signal maximum [41].

Finally, the signals corresponding to the time and position of detected ions are collected shot-by-shot and recorded with a time-to-digital converter TDC8HP system from RoentDek, and all the data is saved using the Computer-Based Online-offline List-mode Data-analyser

(CoboldPC) [42], which is a data acquisition and control software, in the ".lmf" format to determine time-of-flight, XY impact position, coincidence events, and further analysis.

3.3 COLTRIMS setup used for pump-probe experiments on SO_2 molecules with PULSAR and FLAME lasers.

This section briefly summarizes the components and structure of the COLTRIMS setup coupled to the PULSAR laser at the JRML, which was used to collect data on sulfur dioxide (SO_2) molecules discussed in Chapter 4. This is an older setup based on the apparatus described in [63] with significant modifications in the supersonic jet arrangement. Conceptually, this instrument is very similar to the Konza COLTRIMS described above. Currently, the PULSAR COLTRIMS setup consists of a 30 µm diameter nozzle, equipped with two micrometer screws for precise alignment. Positioned behind the nozzle is a skimmer with a diameter of 200 µm, followed by two apertures of 1 mm and 2 mm in diameter to create a highly collimated cold molecular gas jet [43]. The gas jet, which in this setup propagates in the vertical direction downwards, is guided towards the main chamber through three differentially pumped stages, maintaining an ultra-high vacuum with pressure below 10^{-10} mbar. After the main chamber with an opening of 6 mm, there is a single-stage catcher (jet dump) to collect the residual gas. Ultra-high vacuum conditions are maintained by a set of turbo molecular pumps, backed by the roughing pumps. The laser beam is focused onto the molecular beam using a spherical mirror with a 7.5 cm focal length inside the chamber. The mirror mount consists of three micrometer screws aligned along the x, y, and z directions to adjust the focus of the laser beam on the cold gas jet. Ion fragments created from the laser molecular interaction inside the horizontally placed main chamber are guided toward the detector by a homogeneous electric field applied by the horizontally oriented spectrometer inside the main chamber. The ion detector consists of an MCP for time measurement and a two-layered delay line detector for determining the 2D position of the detected ions. More details on the ion detector and momentum calculation in PULSAR COLTRIMS can be found in Chapter 3 of [43] and [44].

3.4 Calculation of Momentum Components of Charged Fragments

For further analysis and physical interpretation of the saved data, the time information collected from the MCP front signal, and the position information from the delay-line anode signals of all detected ions need to be converted into momentum components along the x, y, and z directions. For the COLTRIMS setup, the coordinated system is defined as follows: the laser beam propagates along the x-axis, the thin molecular jet propagates along the y-axis, and the homogeneous electric field is applied along the z-axis. All charged fragment particles fly towards the detector along the z-axis under a constant acceleration motion.

The origin of the hit coordinates (x_0, y_0) is defined at the center of the detector, while the origin of the z-axis (z_0) is taken to be the point where the laser beam crosses the molecular jet in the interaction region. The three momentum components (P_x, P_y, and P_z) of a charged fragment with mass m and charge q, and a travel distance l from the interaction region to the ion detector can be calculated using Newton's second law for the equation of motion as follows,

$$P_x = \frac{m(x - x_0)}{(t - t_0)} \tag{3.6 a}$$

$$P_y = \frac{m(y - y_0)}{(t - t_0)} \tag{3.6 b}$$

$$P_z = \frac{ml}{(t - t_{0)}} - \frac{1}{2} qE(t - t_0) \tag{3.6 c}$$

where t_0 is the interaction time offset.

With all the complete momentum P_x, P_y, and P_z of a particular fragment of the molecule, its kinetic energy can be calculated by the equation,

$$KE = \frac{P_x^2 + P_y^2 + P_z^2}{2m} \tag{3.7}$$

It is also important to note that, assuming the molecule has zero initial momentum before fragmentation, total momentum must be conserved. Therefore, for a given molecule breaking into n charged fragments, the sum of the momentum components of all fragments along each axis should be zero.

$$\vec{p}_1 + \vec{p}_2 + \cdots + \vec{p}_n \approx 0 \tag{3.8}$$

Chapter 4 - Results and Discussion

4.1 Strong-field induced dynamics of the CH_2ClI molecule.

This section shows preliminary results of the experimental study of the fragmentation dynamics of CH_2ClI molecules irradiated by intense NIR pulses of the 100 kHz Konza laser (briefly described in section 3.1.3). This experiment was performed as a part of the commissioning of the new COLTRIMS setup described in section 3.2. Besides testing the system's components, the main motivation of this experiment was to evaluate the data collection efficiency of the 100 kHz laser system and to investigate the potential of detecting in coincidence all fragments produced in a complete breakup of a molecule with five atoms. To enable a direct comparison between the results obtained from the new COLTRIMS and previously analyzed data using PULSAR COLTRIMS, we selected the CH_2ClI (chloroiodomethane) molecule, which was studied in [43,44], as our target species. For this experiment, the aperture at the entrance of the main chamber was approximately 1 cm in diameter, which resulted in large background contributions from the warm part of the jet. To enhance the cold-to-warm-target ratio for the supersonic gas jet, this aperture was later replaced with a 1 mm aperture.

The high-energy (HE) OPCPA output of the Konza laser, with a fixed central wavelength of 800 nm, was employed in the experiment. Since the laser was still in the commissioning stage, the pulse duration did not reach the optimized value of 20-25 fs and was close to 100 fs. The peak intensity of the laser pulse at the focus was estimated to be 1.2×10^{14} W/cm^2. For these conditions, the value of Keldysh parameter is $\gamma \approx 0.83$ (Eq. 2.24), and the critical intensity limit for OBI for single ionization of the neutral CH_2ClI molecule, estimated according to Eq. 2.26, yields $I_{OBI} = 3.3 \times 10^{13}$ W/cm^2. These values suggest that the experiment is carried out in the over-the-barrier ionization regime, and single ionization at the peak intensity of the pulse is saturated. This expectation is consistent with the measured ion TOF spectrum shown in Fig. 4.1, which shows various ionic fragments resulting from single, double, or multiple ionization of the CH_2ClI molecule.

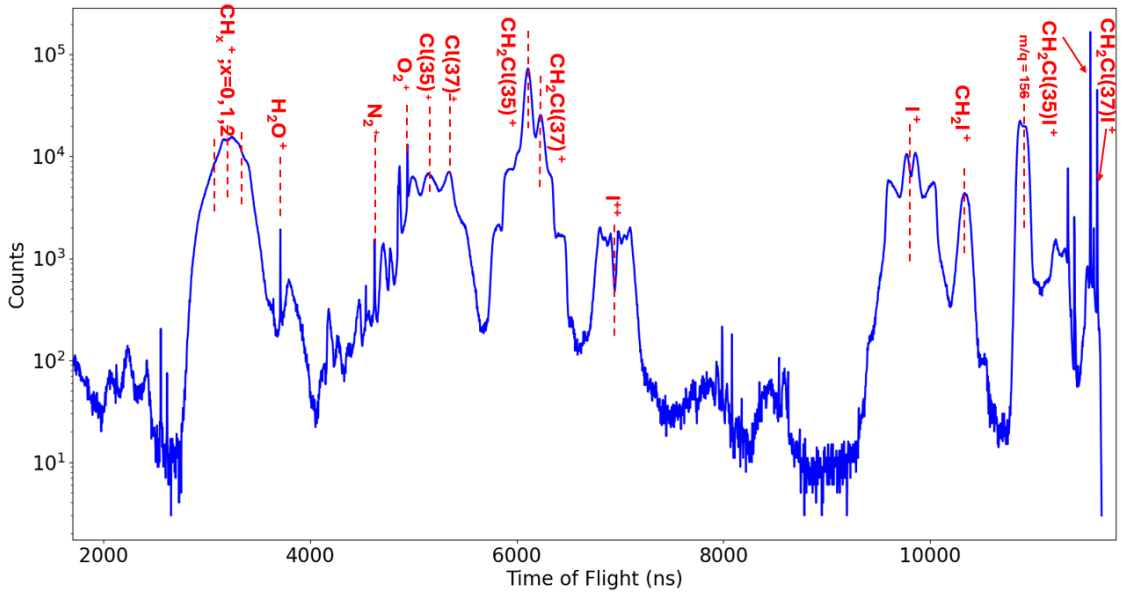

Figure 4.1 Time-of-flight (TOF) spectrum (in log scale) for the CH_2ClI molecules irradiated by a single NIR pulse.

As can be seen in Figure 4.1, when the single NIR pulse ionizes the CH_2ClI molecule, it can trigger various ionization, dissociation, and Coulomb explosion pathways. The vertical dashed lines indicate the ion peaks for different species, calibrated according to the mass-to-charge ratios, under the assumption of zero initial momentum along the spectrometer axis. The spectrum is dominated by the bound parent ions (CH_2ClI^+) and CH_2Cl^+ ion fragments with the ^{35}Cl isotope. Due to the natural abundances of ^{35}Cl and ^{37}Cl, the spectrum shows double peaks for ions with a Cl atom. Noticeably, the TOF distribution shows that dissociative ionization pathways favor the formation of CH_2Cl^+ fragments over CH_2I^+ fragments, likely reflecting the larger electronegativity of chlorine compared to iodine. Additionally, the TOF spectrum includes ion peaks corresponding to residual background gases such as O_2, N_2, and H_2O.

In the TOF spectrum, non-fragmented ("parent") ions (CH_2ClI^+ and (CH_2ClI^{2+})) from the cold jet appear as very narrow and sharp peaks, reflecting the relatively small momentum, which is balanced by the sum of the emitted electrons, which have a much smaller mass compared to the ion. In contrast, fragment ions from the molecules (such as I^+, I^{++}, CH_x^+, CH_2Cl^+, and CH_2I^+) and the background species exhibit a broader distribution with some symmetry around the zero-momentum line, as they have larger momentum, which is balanced by the momentum of other fragment ions produced during the molecular breakup. The broader distribution of a particular ion

peak can be described as follows: the left half of the distribution corresponds to the molecular fragment ions flying towards the detector immediately after breakup, while the right half represents ions that initially fly away from the detector but are later guided by the homogeneous electric field towards the ion detector.

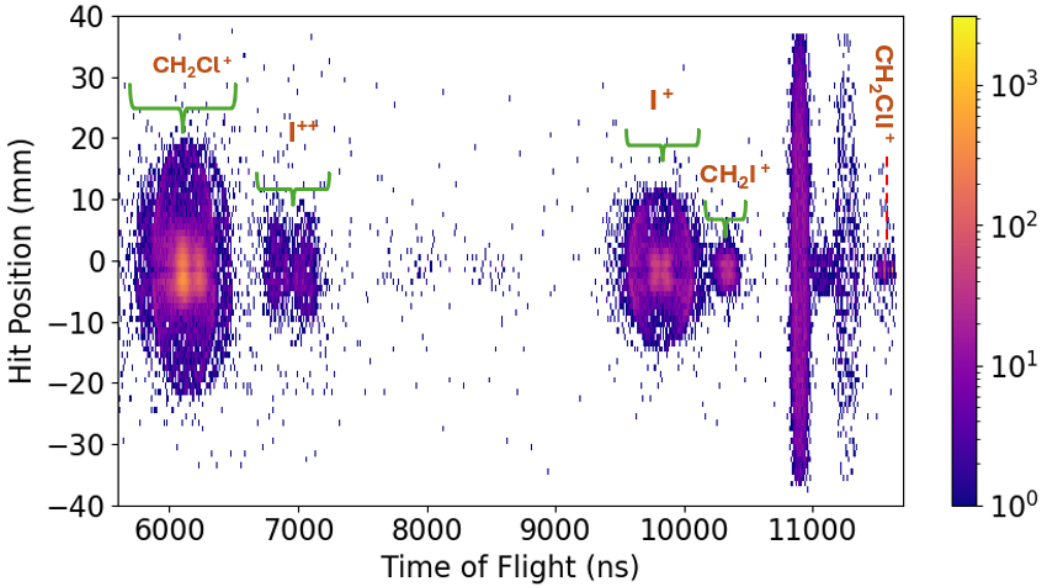

Figure 4.2 2D representation of the ion yield as a function of TOF and hit position on the detector from the detector center.

Figure 4.2 shows the 2D representation of the ion yield in the TOF window from (5600-11700) ns, including parent ions (CH_2ClI^+) and fragment ions CH_2Cl^+, I^{++}, I^+, and CH_2I^+ from the molecules. Since the 2D representation reflects the momentum distribution of each detected ion along the TOF, in this representation, we can observe that ions with low momenta (non-fragment/ parent ions) appear as a well-localized spot, while ions with larger momenta (fragment ions) appear in a circular-like distribution.

4.2.1 Coincidence Analysis

Since the ion detector employed here is capable of multi-hit detection, it is possible to detect multiple ions per laser shot. Among these detected ions, those originating from the same ionization event (i.e., from the same molecule) are expected to be correlated in their arrival times at the detector. The TOF of each detected ion, which, in our experiments, is typically in the range of microseconds, depends on its mass-to-charge ratios and initial momenta. Coincidence analysis involves identifying such correlated ion hits using correlation maps of the ions' time of flight. In these maps, the x-axis typically represents the TOF of the first detected ions, while the y-axis represents either the TOF of the second detected ions in the two-body coincidence, or the summation of the TOF values of all remaining n-1 fragment ions in the case of n-body break-up channels.

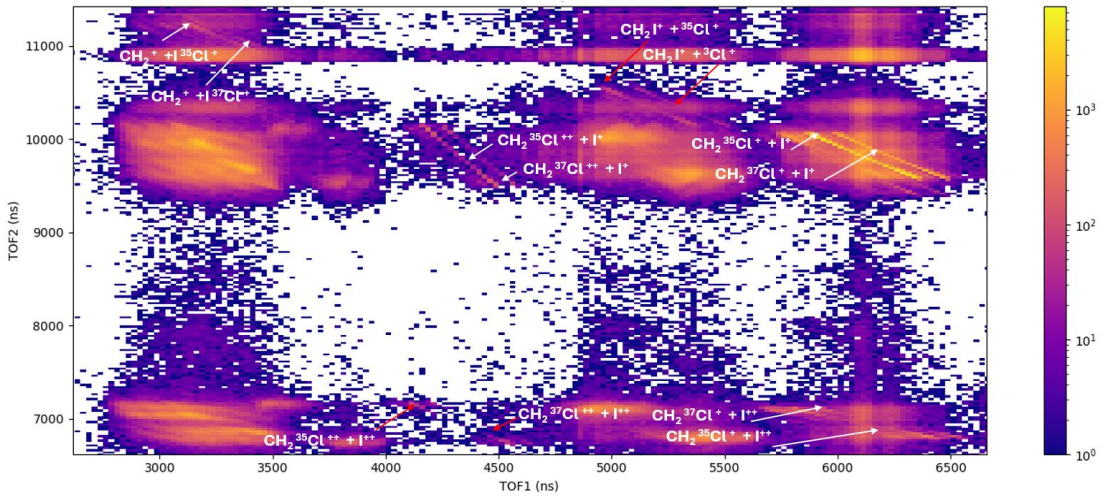

Figure 4.3 Photoion-Photoion Coincidence (PiPiCo) map of the CH_2ClI molecule irradiated by a single NIR pulse. The x-axis represents the TOF of the first detected ions, while the y-axis represents the TOF of the second detected ions.

Figure 4.3 shows the typical correlation map of two-body breakup channels of the CH_2ClI molecule. Due to the momentum conservation in each two-body breakup channel, the velocities of the two fragments are coupled in a way that their momentum vectors point in opposite directions. As a result, the ion emitted toward the detector arrives earlier than its partner, which is emitted in the opposite direction. This gives a nearly linear correlation between the two TOF values, which appeared in a narrow diagonal line in the PiPiCo map. These lines are labeled based

on the TOF values of the two fragment ion combinations that can be produced by the same molecule. The rest of the broader structureless background features occur from either false (random) coincidence or incomplete many-body breakup pathways, where one or more fragment ions are not detected. For further analysis, true coincidence events from a particular two-body breakup channel can be extracted by applying a TOF gating condition along the corresponding sharp lines.

Figure 4.4 shows the typical correlation map of three-body breakup channels of the CH_2ClI molecule. Since it is three fragment ions, the resulting correlation map is referred to as a Triple Photoion Coincidence (TriPiCo) map. In the TriPiCo map, the x-axis represents the TOF of the first detected ion, while the y-axis represents the summation of the TOF of the second and third hit ions of the $CH_2^+ + Cl^+ + I^+$ 3-body breakup channel.

According to Figure 4.4, the sharpest and brightest TriPiCo line corresponds to the coincidence channel (b) with the ^{35}Cl isotope. Channels (c) and (d) are identified as incomplete channels, as they detect the first hit without one or two hydrogen atoms attached to Carbon.

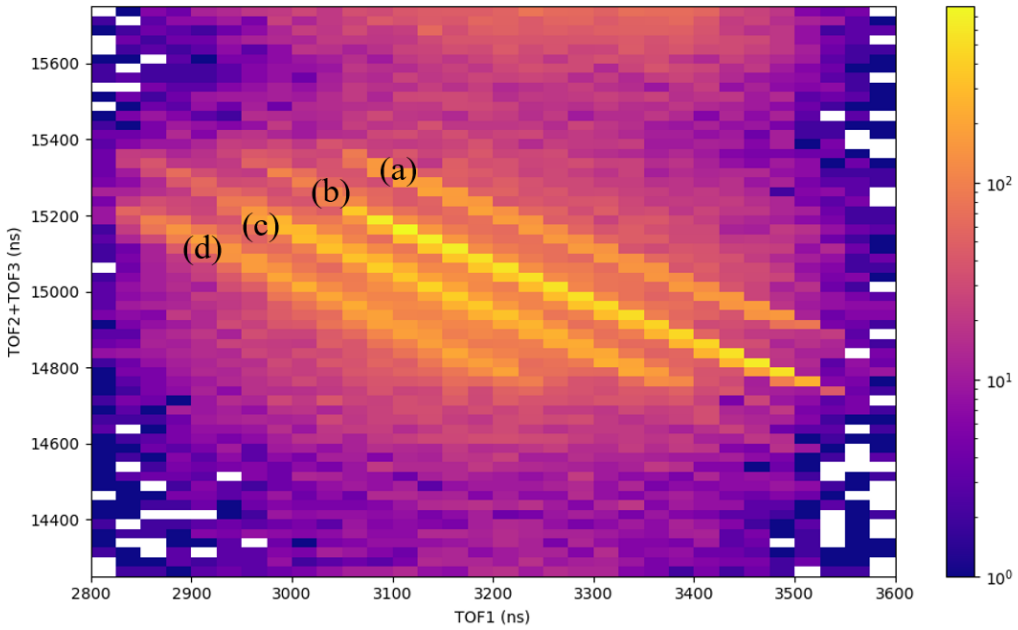

Figure 4.4 Triple Photoion Coincidence (TriPiCo) map for the three-body breakup channel of the CH_2ClI molecule irradiated by a single NIR pulse. The channels labeled from a to d are: (a) $CH_2^+ + {}^{37}Cl^+ + I^+$, (b) $CH_2^+ + {}^{35}Cl^+ + I^+$, (c) $CH^+ + {}^{35}Cl^+ + I^+$, and (d) $C^+ + {}^{35}Cl^+ + I^+$.

All the coincidence maps shown in this section are from data collected for 90 minutes. This higher repetition rate enables us to collect more statistics in high-coincidence data in less time, while also minimizing false coincidences. Figure 4.5 (a) and (b) show both four and five-body coincidence events in the CH_2ClI molecule, which we could successfully observe using the 100 kHz laser. It is important to highlight that, compared to the 3 and 10 kHz laser systems available at JRML, the new 100kHz laser enabled significantly faster data acquisition. The ability to effectively capture the fragmentation dynamics of larger molecules with this high-repetition rate laser enables a significant improvement in ultrafast molecular dynamics studies.

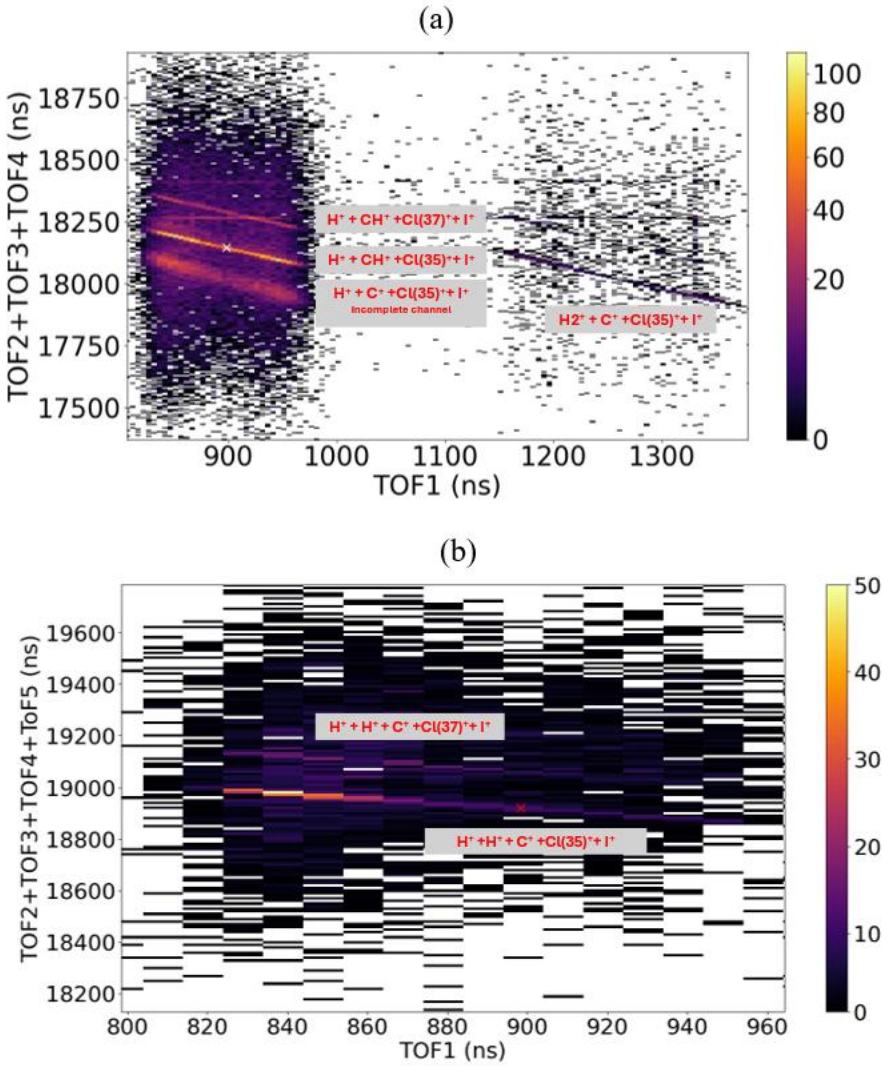

Figure 4.5 n-body (n=4 and 5) coincidence channels observed in the CH_2ClI molecule irradiated by a single NIR pulse. (a) 4-body breakup and (b) 5-body breakup of the CH_2ClI molecule. The x-axis represents the TOF of the first detected ion, while the y-axis represents the summation of the TOF of all the other detected fragment ions corresponding to the n-body breakup channels.

While the overall fragmentation pattern as well as PiPiCo and TriPiCo spectra presented here are similar to those obtained in [43,44] using the PULSAR laser, a direct comparison with those results is hampered by the difference in laser pulse duration. While earlier work with PULSAR employed 25-28 fs laser pulses, the Konza pulse duration used here was not optimized yet and was significantly longer (~100 fs). This difference particularly influenced the kinetic energy distributions for different fragments and channels. Figure 4.6 shows such an example of the kinetic energies (KE) of each fragment ion and the kinetic energy release (KER) of the three-body breakup channel $CH_2^+ + {}^{35}Cl^+ + I^+$, which were shifted to lower values for this work compared to the results of [43,44]. Because of this, the data obtained for CH_2ClI fragmentation could not be used for a cross-check of the ion energy calibration, which was part of the motivation for this work.

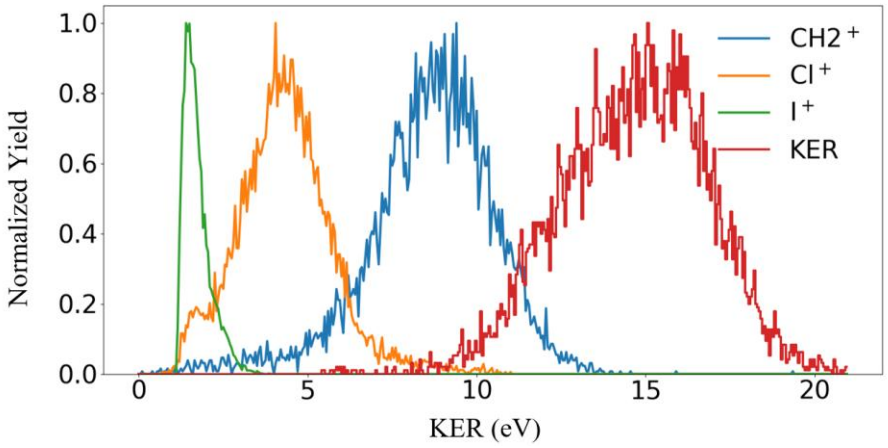

Figure 4.6 The 1D KER distribution of the three-body fragmentation channel $CH_2^+ + {}^{35}Cl^+ + I^+$ and the KE distribution of individual fragment ions. All yields represented are normalized to 1 relative to their maximum yield.

4.2 NIR pump and NIR probe experiment on sulfur dioxide molecules.

This pump-probe experiment was performed using the PULSAR laser system, operating at a 10 kHz repetition rate. The laser generates NIR pulses with a central wavelength of 790 nm and a pulse duration of approximately 28 fs. This study was carried out using the older COLTRIMS setup described in Section 3.3. In the experiment, the incoming laser beam was split by a beam splitter to generate a pump pulse with an intensity of 3.4 x 10^{14} W/cm^2 and a probe pulse with an intensity of 8 x 10^{14} W/cm^2. The Keldysh parameter calculated for the pump and probe intensities is $\gamma \approx 0.556$ and 0.36, respectively. The critical intensity limit for OBI of the SO_2 molecules is 9.3 x 10^{13} W/cm^2, which suggests that single ionization for both pump and probe pulses falls into the over-the-barrier regime. Both beams were linearly polarized, and the time delay between them was controlled using a motorized delay stage.

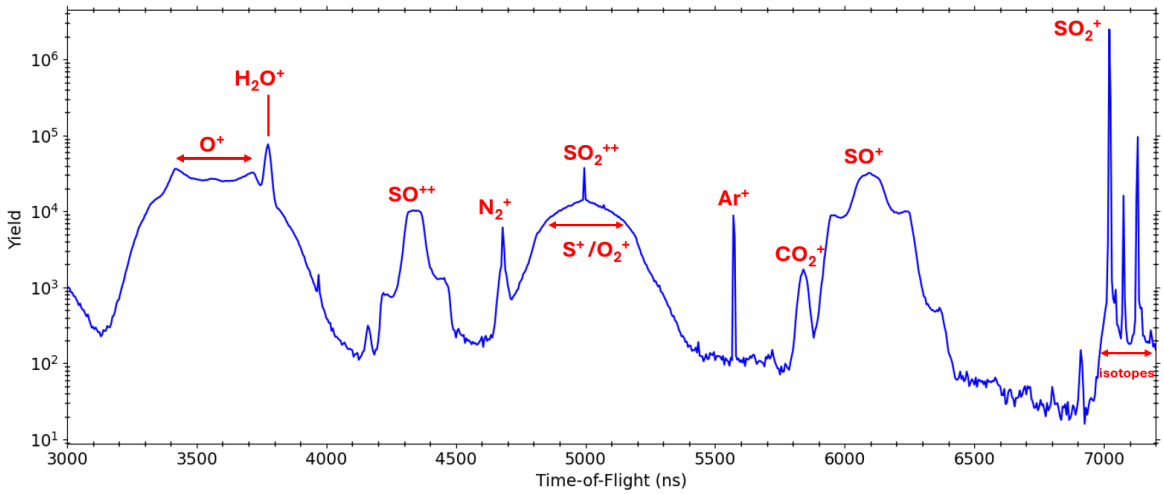

Figure 4.7 TOF spectrum of SO_2 molecules (in log scale) initially irradiated by an NIR pump pulse of intensity 3.4 ×10^{14} W/cm^2 and followed by an NIR probe pulse of intensity 8 ×10^{14} W/cm^2.

Figure 4.7 shows contributions from all ionic fragments detected during the pump-probe experiment, originating from the ionization and/or fragmentation of SO_2 molecules and background residual gases. The most prominent peaks at larger TOF values correspond to the singly charged parent ion (SO_2^+) and its isotopes (^{33}S and ^{34}S). The doubly charged parent ions have the same mass-to-charge ratio as S^+ and O_2^+ ions, hence appear at the same TOF position. However, due to their low momentum, the SO_2^{++} form a sharp, narrow peak that sits on top of the broader distribution, corresponding to S^+ and O_2^+ ions.

4.2.1 Channel Identification and Separation

Figure 4.8 represents the 2-D scaled projection of the 3-D momentum sphere of fragment ions that appear in the same TOF window as shown in Figure 4.7. In this 2-D representation, the sharp, narrow parent ion peaks in the 1D TOF spectrum (SO_2^+ and SO_2^{++}) appear as well-localized spots in the middle, while the ions with broader peaks appear as circle-like structures.

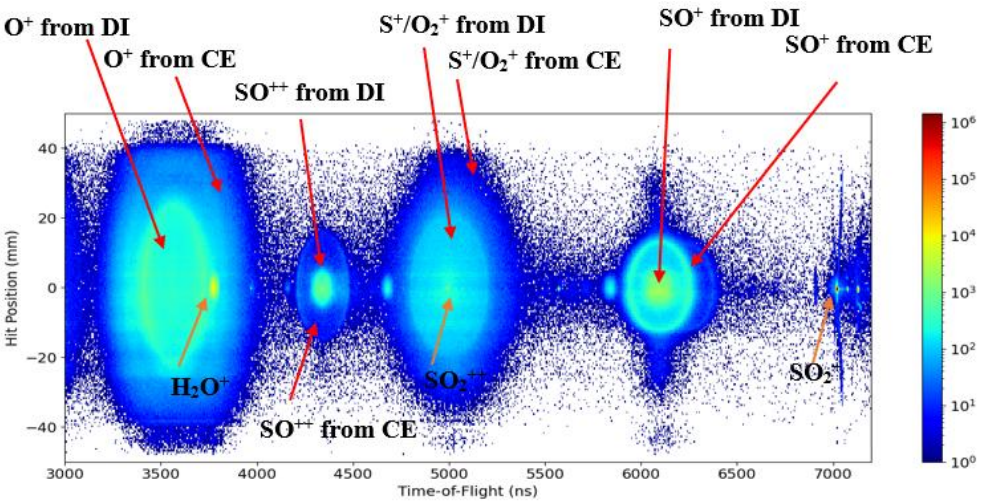

Figure 4.8 2D representation of the ion yield (of the ions shown in the same TOF as in Figure 4.7) as a function of the TOF and hit position on the detector from the detector center. The arrows show different fragmentation pathways (either DI or CE) of fragment ions of the sulfur dioxide molecule detected in the pump-probe experiment.

As shown in Figure 4.8, the fragment ion species appearing in the circle-like structure have two distinct contributions. The inner structure corresponds to ions resulting from dissociative ionization (DI) with a neutral partner, while the outer features come from the double ionization and subsequent Coulomb Explosion (CE). Hence, the 2D representation guides us to distinguish ion fragments with different momenta (kinetic energies) from different breakup pathways. To verify ions corresponding to these two pathways, we can look at and compare the kinetic energy distributions of each ion detected in coincidence or without a coincidence partner in the pump-probe experiment.

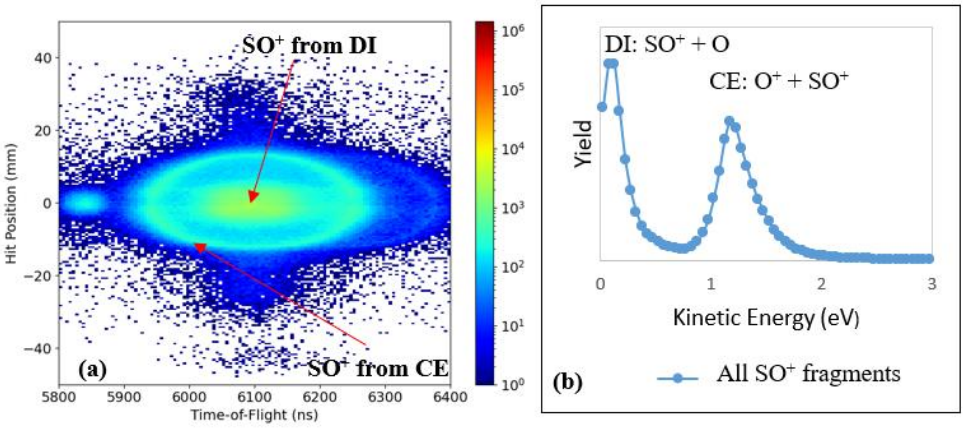

Figure 4.9 (a) 2D representation of all detected SO^+ as a function of TOF and hit position on the detector, (b) The corresponding kinetic energy distribution of all SO^+ ions (with or without coincidence partners).

Figure 4.9 (a) illustrates all the SO^+ ion fragments detected, without any coincidence condition. (We will refer to such data as "non-coincident" throughout the rest of the document). Therefore, it includes the ions created due to the dissociative ionization with a neutral partner and those due to the Coulomb explosion with a charged partner. Figure 4.9 (b) shows the KE distribution of all the SO^+ ions shown in Figure 4.9 (a). The low KE peak at 0.125 eV corresponds to SO^+ ions from DI, which appear in the inner region of the circle-like structure. The higher KE peak at 1.175 eV corresponds to SO^+ ions from CE appearing in the outer region in the circle-like structure, which is detected in coincidence with O^+ ions.

Figure 4.10 shows the typical PiPiCo map observed in the pump-probe experiment on SO_2 molecules. By applying TOF gating on the sharp lines, the events corresponding to the coincidence detection of the two fragment ions from the same molecules can be filtered out for further analysis.

Figure 4.11 compares the kinetic energy peaks that appear in the non-coincident energy distribution (blue curve) with the KE of corresponding fragment ions detected in coincidence with different 2-body CE channels (grey and orange). The higher energy peaks appear in all non-coincident ion spectra corresponding to the events from the CE two-body breakup channels with charged partners. The low KE peak in the non-coincident spectra corresponds to ions from DI.

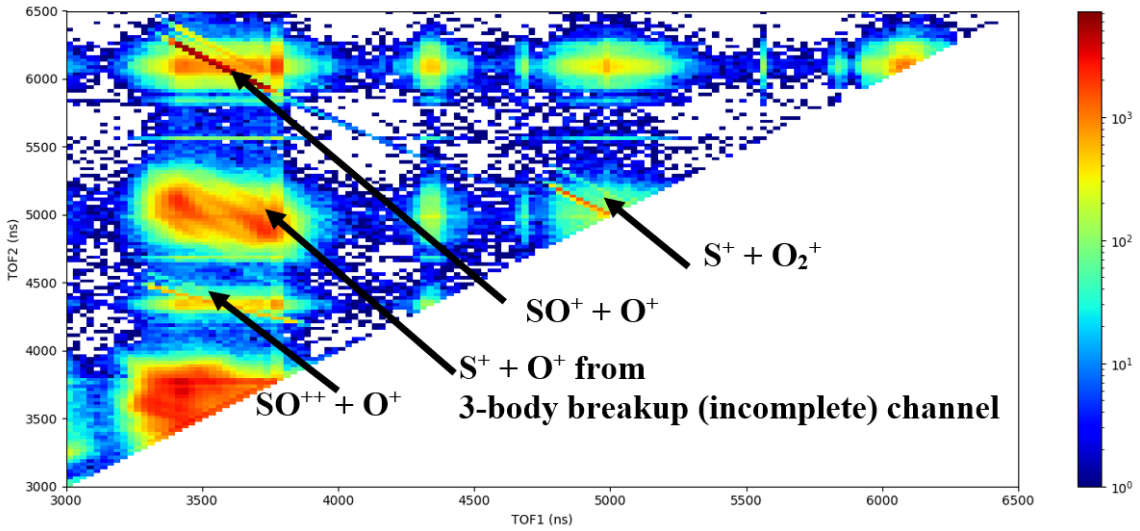

Figure 4.10 Figure 4.10 PiPiCo map for 2-body breakup channels observed in SO_2 irradiated by an NIR pump pulse of intensity 3.4×10^{14} W/cm^2 and followed by an NIR probe pulse of intensity 8×10^{14}W/cm^2.

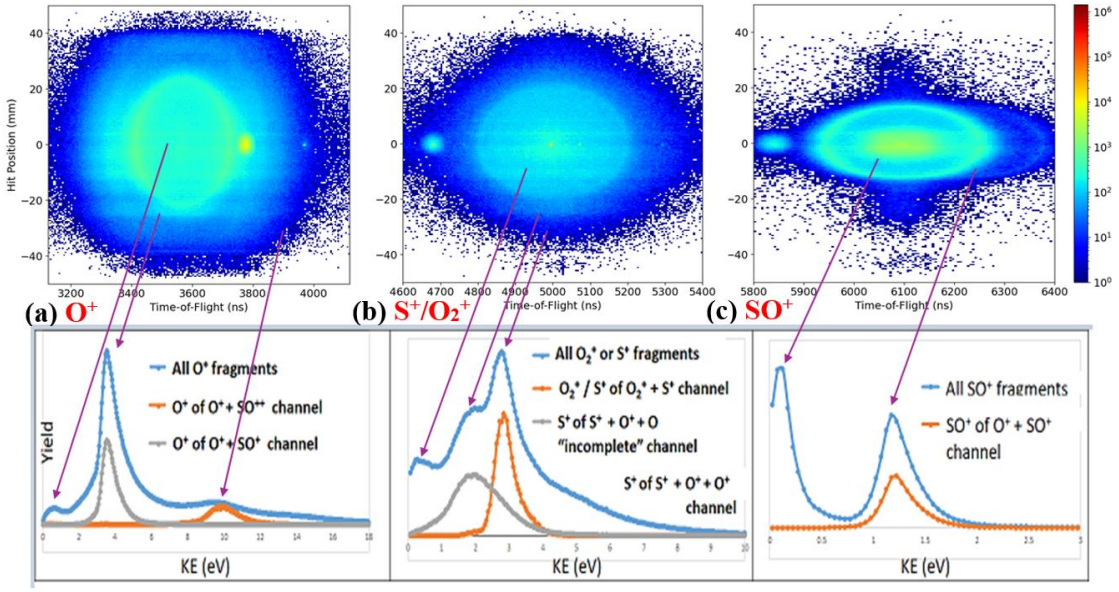

Figure 4.11 2D representation of O^+, S^+/O_2^+, and SO^+ ions as a function of TOF and hit position on the detector (top panel), and their corresponding kinetic energy distributions (bottom panel). Blue curves show the KE distributions for all ions detected without coincidence, while grey and orange curves represent the KE spectrum of ions detected in coincidence with a charged partner. Coincidence channel yields were scaled by different constant factors to enable visual comparison.

4.2.2 Channel Selective Analysis of Strong-Field Induced Nuclear Wave Packet in Sulfur Dioxide

As illustrated in Figure 4.12, we mainly focus on the scenario where the pump pulse ionizes the neutral SO_2 molecule in the $\tilde{X}^1A_1$ ground state and launches an ionic wave packet in the $\tilde{X}^2A_1$ electronic ground state (or other low-lying cationic states). Then, the probe pulse will dissociate or further ionize the created SO_2^+ ions. However, as will be discussed below, we have also observed signatures of vibrational excitation of the neutral SO_2 molecule in its $\tilde{X}^1A_1$ ground state by the pump pulse.

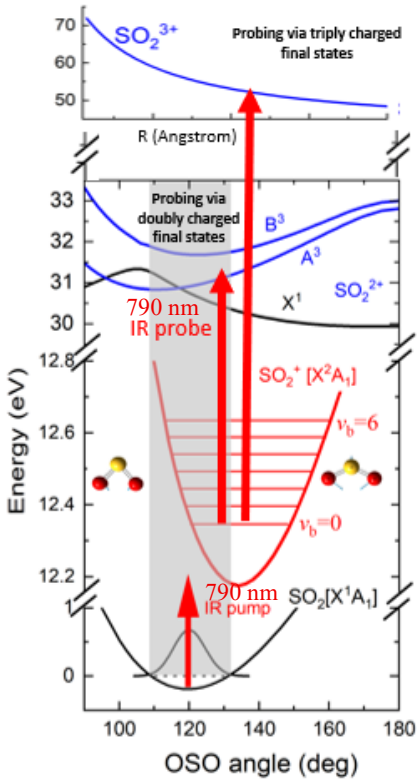

Figure 4.12 Sketch of the pump-probe scheme and relevant potential energy curves for the SO_2 molecule [19].

In this study, we mainly focus on the following fragmentation channels (after both pump and probe pulses): Singly charged final states produced by dissociative ionization into (1) SO^+ + O and (2) O^+ + SO channels; double ionization producing bound parent ion (3) SO_2^{2+}; double ionization resulting in a Coulomb explosion into complete channels (4) $O^+ + SO^+$, (5) $S^+ + O_2^+$ and

incomplete channel (6) $O + O^+ + S^+$; and triple ionization resulting in a Coulomb explosion into (7) $O^+ + O^+ + S^+$ final state.

Figure 4.13 presents two examples of selecting events related to channels 1 (panel a) and 4 (panel b) listed above. In both features, the enhancement observed around zero delay (sharp vertical line) shows the contribution where two pulses overlap.

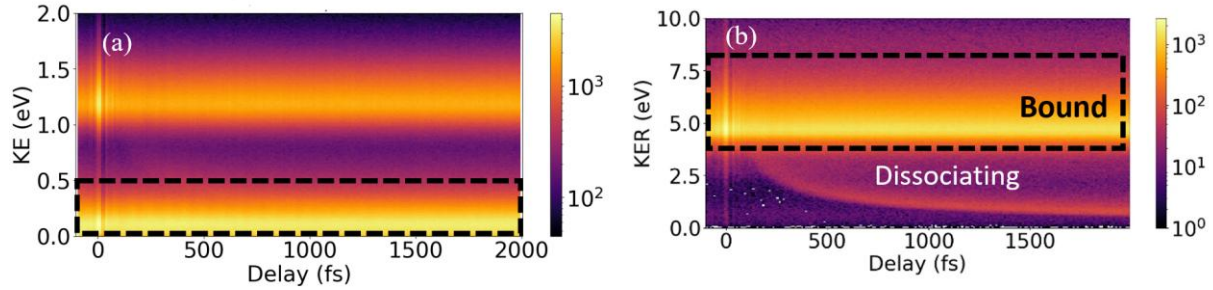

Figure 4.13 (a) Delay-dependent kinetic energy distribution of all SO+ detected non-coincidence. (b) Delay-dependent kinetic energy release of $O^+ + SO^+$ two-body coincidence channel. The delay window for the scan is from -100 to 2000fs with a 10fs step size. Positive delay is the strong NIR pulse arriving late as the probe pulse.

Figure 4.13 (a) shows the KE distribution of all detected SO^+ ions as a function of pump-probe delay. In these non-coincidence data, the events with low KE (0 eV to 0.5 eV, marked by the dashed rectangle) result from the $SO^+ + O$ final state and can originate from dissociative ionization, either by the pump or the probe pulse, or by their combined action. The higher-energy band at 1.25 eV is due to $SO^+ + O^+$ Coulomb explosion (see Figure 4.11 (c)). This horizontal band (marked by a dashed rectangle) is also clearly visible in Figure 4.13 (b), which displays the delay-dependent KER (here, just the sum of two fragments' KEs) of SO^+ and O^+ ions detected in coincidence. Note that, for this channel, the SO^+ ion carries $1/4^{th}$ of the KER because of the mass ratio of the two fragments, which have the same momenta. In both panels, the upper horizontal band reflects the events where the molecule remains bound (neutral or charged) after the pump pulse and is (further) ionized and fragmented into $O^+ + SO^+$ final state by the probe. The delay-dependent low-KER region in Figure 4.13 (b) corresponds to events where the pump pulse first dissociates the molecules, which are then further ionized by the probe pulse at internuclear separations increasing with time, leading to the Coulomb explosion with KEs decreasing as a function of the delay.

4.2.3 Signatures of molecular bending vibrational dynamics

Although the horizontal bands shown in Figure 4.13 (a) and (b) do not reveal any pronounced delay dependence in such a 2D representation, they do reflect the dynamics of the molecules that are ionized (or excited) by the pump pulse and further ionized and/or dissociated by the probe. To obtain a clearer picture and quantitative insight into the dynamics triggered by the pump pulse, we performed Fast Fourier Transforms (FFT) on the delay-dependent yield of the singly and doubly charged final states within the regions marked by dashed boxes in Figure 4.13, as well as other channels discussed above. For the FFT analysis, only events within the delay range of 150 to 2000 fs were selected to exclude the contribution from the region where two pulses overlap. Additionally, the mean value of the selected data was subtracted to eliminate the DC component of the oscillations. Figure 4.14 (a) shows an example of selecting yield on the SO^+ + O singly charged final state (corresponding to the low-KE events marked in Figure 4.13 (a)), and the corresponding FFT spectrum is shown in Figure 4.14 (b).

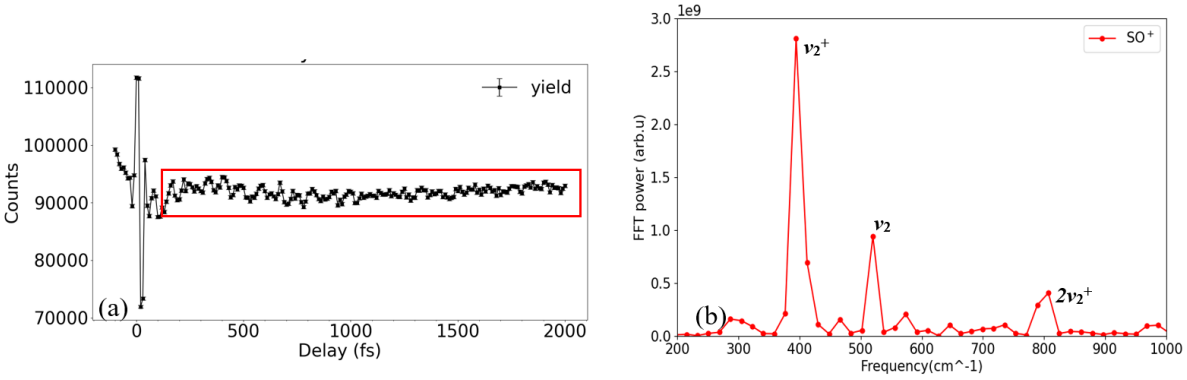

Figure 4.14 (a) Delay-dependent yield of SO^+ + O final state gated on KE from 0 to 0.5 eV. (b) Fast Fourier Transforms (FFT) of the delay-dependent yield selected from 150-2000 fs. v_2^+, v_2, and $2v_2^+$ are the ionic ground-state bending frequency, the neutral ground-state bending frequency, and the first overtone of ionic frequency, respectively. Resolution of the FFT spectrum is ≈ ± 18 cm^{-1}.

According to Figure 4.14 (b), the results are dominated by the peak centered at ~400 cm^{-1}, which corresponds to the ionic ground state bending vibrational frequency (v_2^+) of SO_2^+ ($\tilde{X}^2A_1$). Previous studies have shown that the equilibrium geometry for ionic SO_2^+ ($\tilde{X}^2A_1$) state and neutral SO_2 ($\tilde{X}^1A_1$)have almost the same S-O bond length but significantly different (<OSO) bond angle [19], [45], and [48]. Therefore, in this study, we mostly consider the PEC of SO_2 in terms of bond angle instead of bond length, as shown in Figure 4.12. Due to this equilibrium geometry, ionization

of the molecule to the ground cationic state results in strong excitation into bending vibrational modes (v_2^+) and weak excitations into the symmetric (v_1^+) and asymmetric modes (v_3^+) [48]. As shown in Figure 4.15, the bending vibrational frequencies of the first seven modes of SO_2^+ ($\tilde{X}^2A_1$) show very similar vibrational frequency values around 400 cm^{-1} [45], [47].

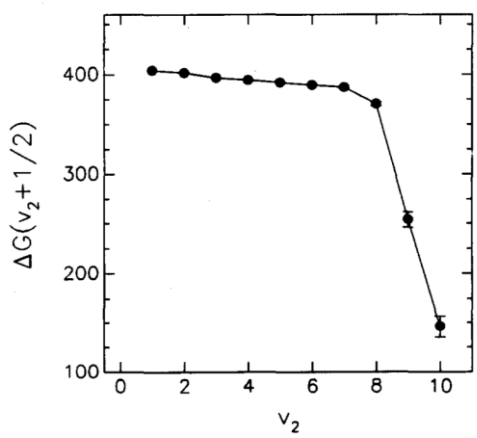

Figure 4.15 The vibrational spacing $\Delta G\ (v_2+1/2)$ of v_2 in the X^2A_1 state as a function of the vibrational quantum number v_2 [45].

Besides the main frequency component, a weak peak around 800 cm^{-1}, which corresponds to the first overtone of the ionic bending vibrational frequency ($2v_2^+$), can also be observed in the FFT spectrum. Interestingly, our experimental data also shows a clear signature of the bending vibrational frequency (v_2) in the ground state of the neutral SO_2 ($\tilde{X}^1A_1$) centered at ~ 520 cm^{-1}[46].

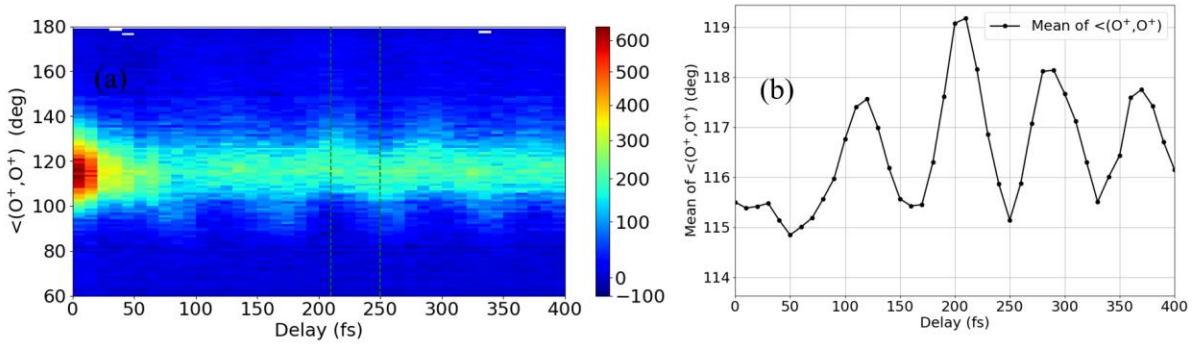

Figure 4.16 (a) Delay-dependence of the angle between the two O^+ momentum vectors from the $O^+ + O^+ + S^+$ triply charged final state (gated on events with KER>14 eV to discard the molecules that undergo dissociation). 210 fs and 250 fs are the points where the bending wave packet reaches the outer and inner turning points in the X^2A_1 state [19]. (b) The average of the mean angle (<O^+, O^+>) as a function of delay.

To directly look at the oscillations of the O-S-O bond angle reflecting bending vibration, in [19], we selected events corresponding to the $O^+ + O^+ + S^+$ triply charged final state, focusing on the horizontal high KE band similar to the one shown in Figure 4.13 (b). Figure 4.16 shows a clear oscillation of the angle between the two O ions. The periodicity of this oscillation was estimated to be 83 fs (~ 400 cm^{-1}), which corresponds to the ionic bending vibrational frequency of the wave packet in $\tilde{X}^2A_1$ state discussed above. Due to the clear oscillations observed between the angle of two O+ at different delays, this pattern provides a good reference to check how the yield of different singly and doubly charged final states behaves at different delays corresponding to small and large angles between the two oxygen ion momenta. As shown in [19], this delay dependence of the momentum space angle can be directly associated with the time evolution of the real-space O-S-O bond angle, even though the absolute values of both angles are different. Thus, the results of Figure 4.16 confirm that the wave packet in the ionic ground state initially moves towards the larger angles, as is expected from the neutral and ionic PECs sketched in 4.12.

Comparing the delay dependence yield modulation of all final states in Figure 4.17 (a), the yield of the doubly charged bound parent ion (SO_2^{++}) shows the clearest signature of oscillations and a minimum at small angles. All other doubly charged final states show almost out-of-phase relationships compared with the yield modulation of SO_2^{++} at small angles. The dephasing of the SO_2^{++} ion yield at larger delays might be due to the excitation into the rotational wave packet by the pump pulse, which will be discussed later in more detail. The $SO^+ + O$ and $O^+ + SO$ singly charged final states show an out-of-phase relationship in their yields at small angles. Hence, it seems SO^+ production is more favorable at the inner turning point in the ionic ground state, while O^+ production is more likely to happen at outer turning points at larger angles.

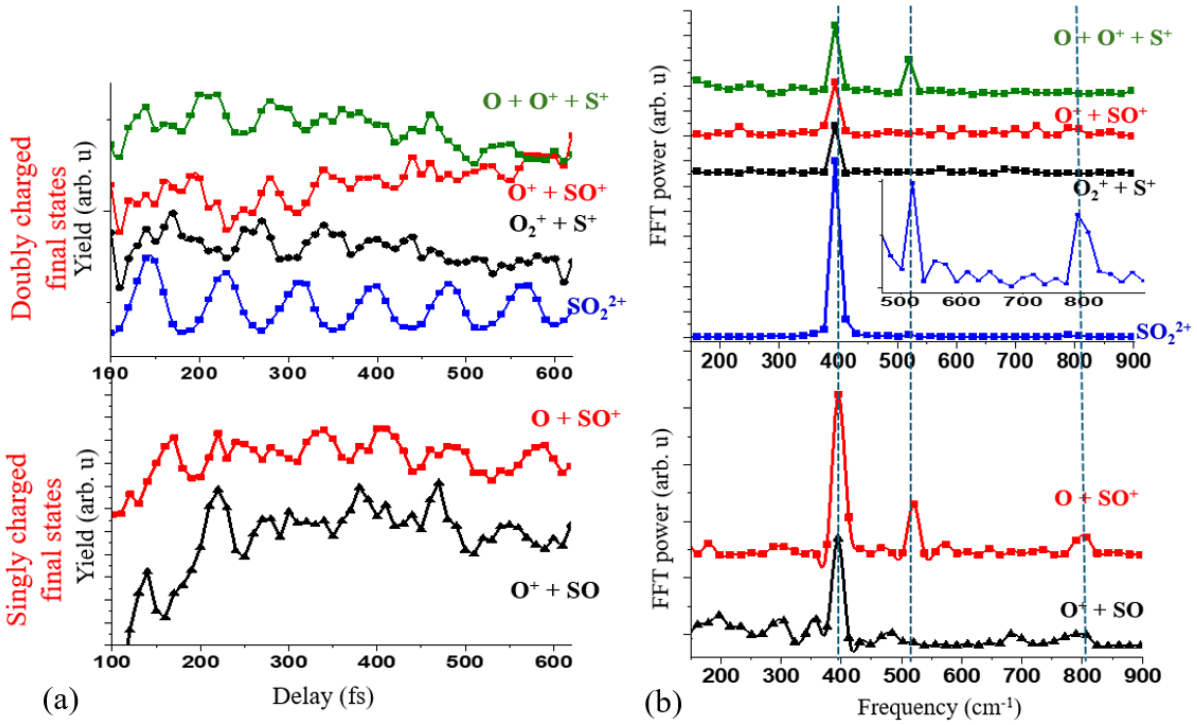

Figure 4.17 (a) Delay-dependent yield of singly and doubly charged final states. The yield data are shifted in the vertical direction for visual convenience. Vertical black dashed lines indicate the times when the O-S-O angle is small, based on the results shown in Figure 4.16 (b). (b) The FFT of the corresponding ion yields shown in (a).

To identify all the frequencies involved with the delay-dependent yield spectra in Figure 4.17 (a), we looked at the corresponding FFT spectrum of each of them. According to Figure 4.17 (b), it is evident that in all given final states, we see the most prominent peak around ~ 400 cm^{-1}, which corresponds to the ionic ground state bending vibrational frequency (v_2^+) of SO_2^+. Other than the clear signature in the singly charged final state of $SO^+ + O$, we could observe a weak signature of the first overtone ($2v_2^+$) of the ionic bending frequency of SO_2^+ in the doubly charged parent ion as well. Interestingly, among all the singly and doubly charged final states, three final states $SO^+ + O$, SO_2^{++}, and $S^+ + O^+ + O$ showed clear signatures of the bending vibrational frequency of the ground state of the neutral SO_2 (v_2) (around ~ 520 cm^{-1}).

As a next step, to find the phases of wave packets corresponding to ionic or neutral ground-state bending vibrational frequencies at 0 fs time delay, we select a specific frequency peak in the FFT spectrum and perform the Inverse Fast Fourier Transform (IFFT) of the corresponding data. Since we selected data from 150 fs to remove the contribution from two pulses overlapping, the

resultant IFFT does not include information on delays before 150 fs. Hence, a sine curve is fitted to the yield obtained from the IFFT and extrapolated to 0 fs to obtain the yield modulation and phases of the wave packets when the dynamics start. In the next sections, we will discuss the ionic and neutral wave packet motion directions by incorporating the phases of the IFFT yields on specific channels.

4.2.3.1 Ionic ground-state bending vibrational frequency of SO_2^+

As shown in Figure 4.18, out of all the IFFT yields for the ionic bending vibrational frequency of SO_2^+, the extrapolated yield of the SO_2^{++} final state is found to be almost out-of-phase with the results for $SO^+ + O^+$ and $S^+ + O_2^+$ channels. The bound SO_2^{++} is more likely to form at large angles. At the small angles, SO_2^{++} ions are more likely to break up, resulting in higher yields of $SO^+ + O^+$ and $S^+ + O_2^+$ two-body break-up channels. While this is natural to expect that O_2^+ formation is more likely to happen at delays corresponding to small angles, where the cations are found when the probe pulse arrives, understanding the phase of the oscillations for the other channels requires a detailed knowledge of the relevant PECs of the corresponding final states.

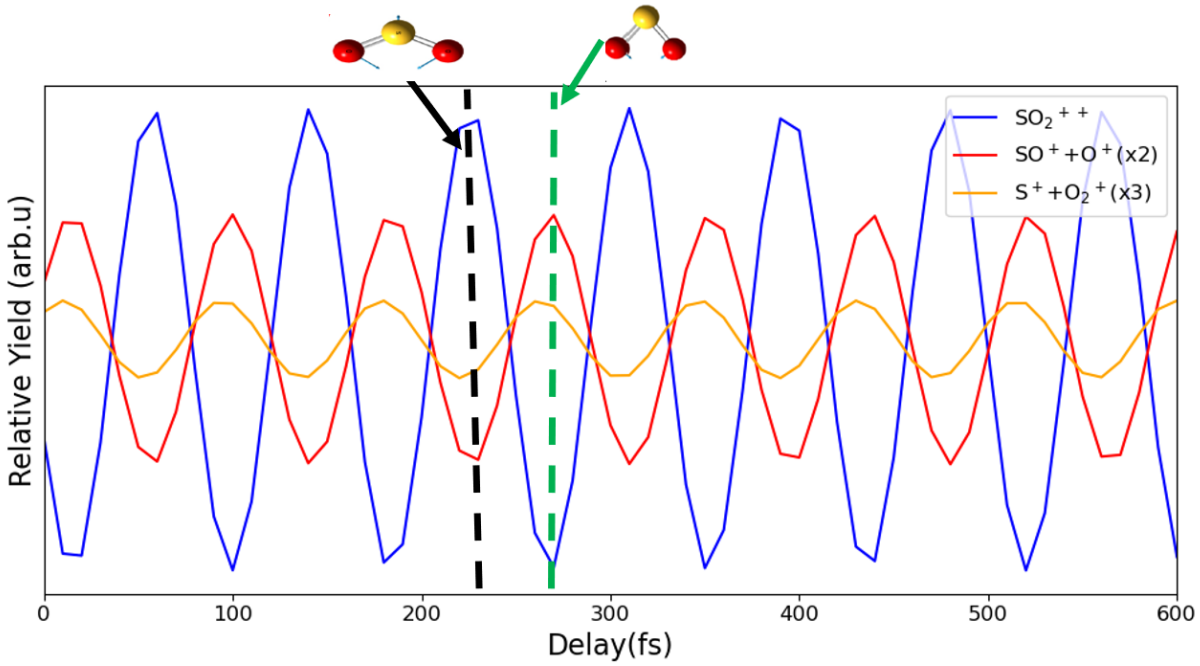

Figure 4.18 Phase modulation of the ionic wave packet of $SO^+ + O^+$, $S^+ + O_2^+$, and SO_2^{++} doubly charged final states. The black and green dashed line corresponds to delay points at which the angle between the two O^+ becomes maximum and minimum, respectively.

4.2.3.2 Neutral ground-state bending vibrational frequency of SO_2

The neutral ground-state bending vibrational frequency of SO_2 reflects the events where the pump pulse initiates the neutral wave packet, and the probe pulse will ionize the molecule to one of the bound or dissociative final states. According to Figure 4.19, the extrapolated yield of all three channels that manifest the vibrational frequency of the neutral initially increases. Since, based on the PECs shown in Figure 4.12, we expect the ionization probability to rise for larger angles, this suggests that the neutral wave packet initially moves to the right (i.e., towards larger angles).

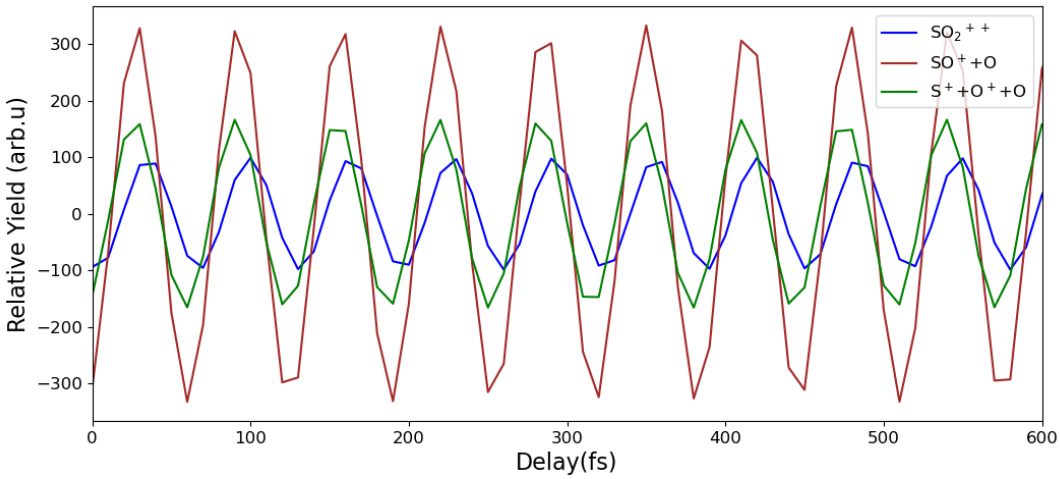

Figure 4.19 Phase modulation of the neutral wave packet of $SO^+ + O$, $S^+ + O^+ + O$, and SO_2^{++} final states.

There are two well-known mechanisms that induce a wave packet in the neutral ground state. The first case is called “Lochfrass or R-selective depletion mechanism”, which is a scenario that results from the ionization probability dependence on molecular geometry. In this case, the strong, intense laser pulses will selectively ionize molecules that have a geometry favorable for ionization, resulting in the remaining wavefunction oscillating. The second mechanism is based on the non-resonant two-photon Raman excitation. In this case, if the molecular axis lines up with the laser polarization direction, the electric field of the laser can induce a temporary distortion to the molecule’s electronic states by modifying their shapes. Bond softening can be identified as a related concept to the Raman excitation, where the laser field weakens the molecular bonds, distorting the potential energy surfaces, and setting the wave packet in oscillatory motion. For diatomic molecules, these mechanisms can be distinguished by looking at the initial phase of the

neutral wave packet oscillation. In case the initial phase shows a sine-like oscillation ($\phi \approx \pm\pi/2$) where the wave packet launches from the equilibrium position with maximum initial momentum, the relevant mechanism is more likely the "Raman excitation" [60]. In Lochfrass, the initial phase shows cosine-like oscillation where the wave packet begins the motion at a turning point with zero initial momentum.

However, unlike linear molecules, it is not very straightforward to understand what is happening in the neutral wave packet in ground-state SO_2. According to Figure 4.19, initially, all three channels show a phase closer to $\pi/2$ and increasing the yield towards the larger angles. From this, it seems one of the probable mechanisms for bending vibrational wave packet formation in the neutral ground state of the SO_2 molecule could be the "Raman excitation". However, the determination of the dominant mechanism of the excitation of the neutral bending vibrational mode in SO_2 is still unclear at this stage of analysis.

4.3 Visible – Near Infrared (NIR) pump-probe experiment on SO_2 molecules.

The main goal of this section was to study the wave packet dynamics triggered by a shorter wavelength excitation. A more specific reason to employ a 400 nm pump pulse was to avoid the single-photon resonant coupling between the lowest cationic states in the pump step, which complicates the interpretation and the modelling of 800 nm pump-800 nm probe results, as discussed in detail in Ref. [19]. In addition, the range of the delay scans was extended to 20 ps in order to improve the FFT resolution and to track longer-term wave packet dynamics.

To improve the stability of the 400 nm pulses, for this experiment, we used the FLAME laser instead of PULSAR but used the same COLTRIMS experimental setup as in the previous section. As discussed in section 3.1.2, FLAME is a laser system operating at 3 kHz, which generates near-infrared (NIR) pulses with a central wavelength of approximately 800 nm and a pulse duration of 27 fs. The incoming beam is split into two beams; one beam passes through a motorized delay stage to control the time delay between the two beams, while the other beam passes through a Barium Borate (BBO) crystal to generate second harmonics of the fundamental beam. The generated visible laser beam has a central wavelength of approximately 400 nm. The power of the two beams could be controlled independently, so the intensities of the visible (400 nm) beam $\approx 4 \times 10^{14}\ W/cm^2$ and NIR beam $\approx 14.8 \times 10^{14}\ W/cm^2$ were employed. The

(Keldysh) parameter calculated for the pump and probe pulses is $\gamma \approx 1.016$ and 0.264, respectively. Even though estimated γ value for the 400 nm pump pulse is slightly greater than 1 (which suggests the transition towards a multi-photon ionization picture), the critical intensity limit for OBI of the SO_2 molecules is 9.3 x 10^{13} W/cm^2, which suggests that even for the pump pulse and, certainly for the probe the ionization happens in the over-the-barrier regime.

Figure 4.20 shows the typical time-of-flight spectrum for the (400 nm) pump and NIR probe experiment of the SO_2 molecules. The main experiment was conducted by scanning from -1 ps to 20 ps in 10 fs steps. Negative delays are NIR pulse coming early, and positive delays are the NIR pulse arriving later than the 400 nm pulse. An analysis for all the singly, doubly, and triply charged final states, as in the NIR-NIR pump-probe experiment described in the previous section, was carried out.

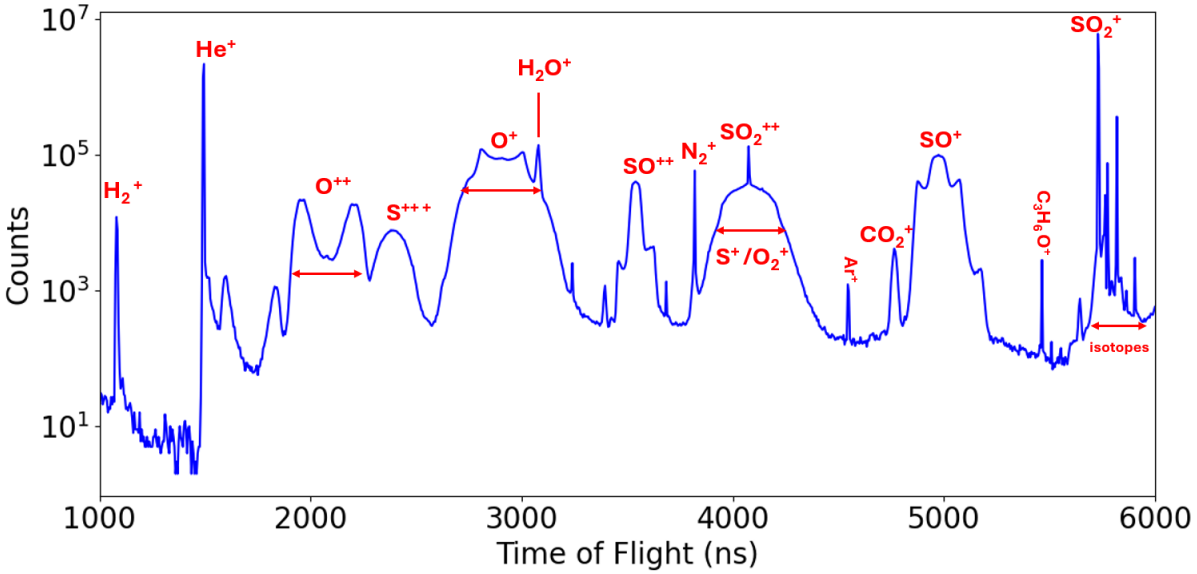

Figure 4.20 TOF spectrum of Visible (400 nm) pump and NIR probe experiment.

Figure 4.21 shows the FFT spectra of all the channels, which exhibit clear signs of oscillations in the delay-dependent yield. Both $SO^+ + O^+$ and $S^+ + O^+ + O^+$ channels were gated in the high KER band, corresponding to CE of the bound molecule (see Figure 4.13 (b)). To visualize the oscillations, for the three-body channel, additional gating on the angle between the two O^+ momentum vectors from 80^0 to 110^0 was applied. The $SO^+ + O$ channel was gated on the lowest KE band in the non-coincident data (similar to Figure 4.13 (a)). According to the FFT spectra, the

observed vibrational dynamics are dominated by the ionic state bending vibrational frequency of ~400 cm^{-1}. Interestingly, with the 400 nm pump, we did not find signatures of the neutral-state vibrational dynamics in any channel studied.

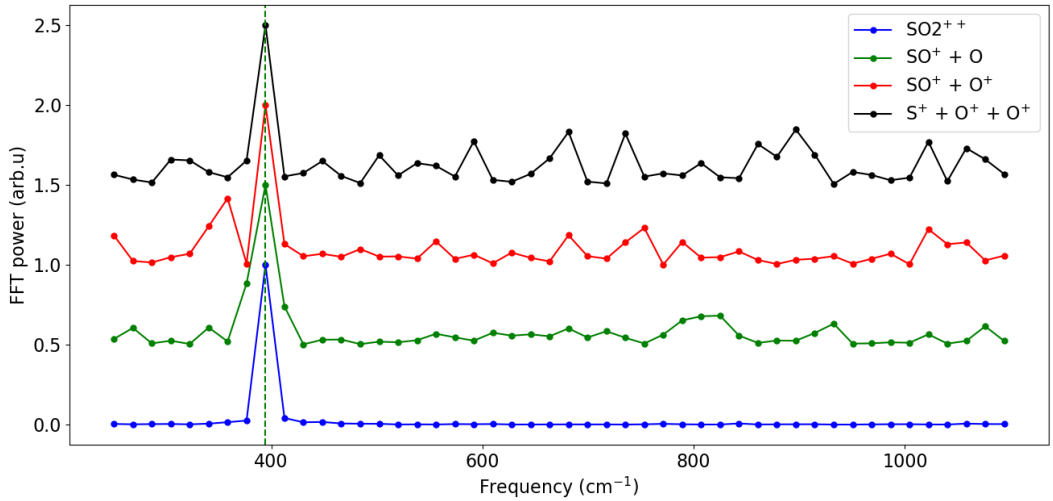

Figure 4.21 FFT spectra of singly, doubly, and triply charged final states correspond to the delay-dependent yield ranging from 150 to 2000 fs with a 10-fs step size. For the three-body channel, only the events of the angle between two O^+ momentum vectors from 80^0 to 110^0 were selected.

It is important to note that the FFT spectra of Figure 4.21 show only the contribution of the delay range from 150 to 2000 fs instead of a 20000fs large delay window. The main reason was that with the long delay window, the oscillations of ~400 cm^{-1} frequency were found to become extinct completely soon after 2 ps, resulting in no clear peak in the FFT spectra. This observation was not the same in the FFT spectra for the delay-dependent yield of the doubly charged parent ion SO_2^{++}.

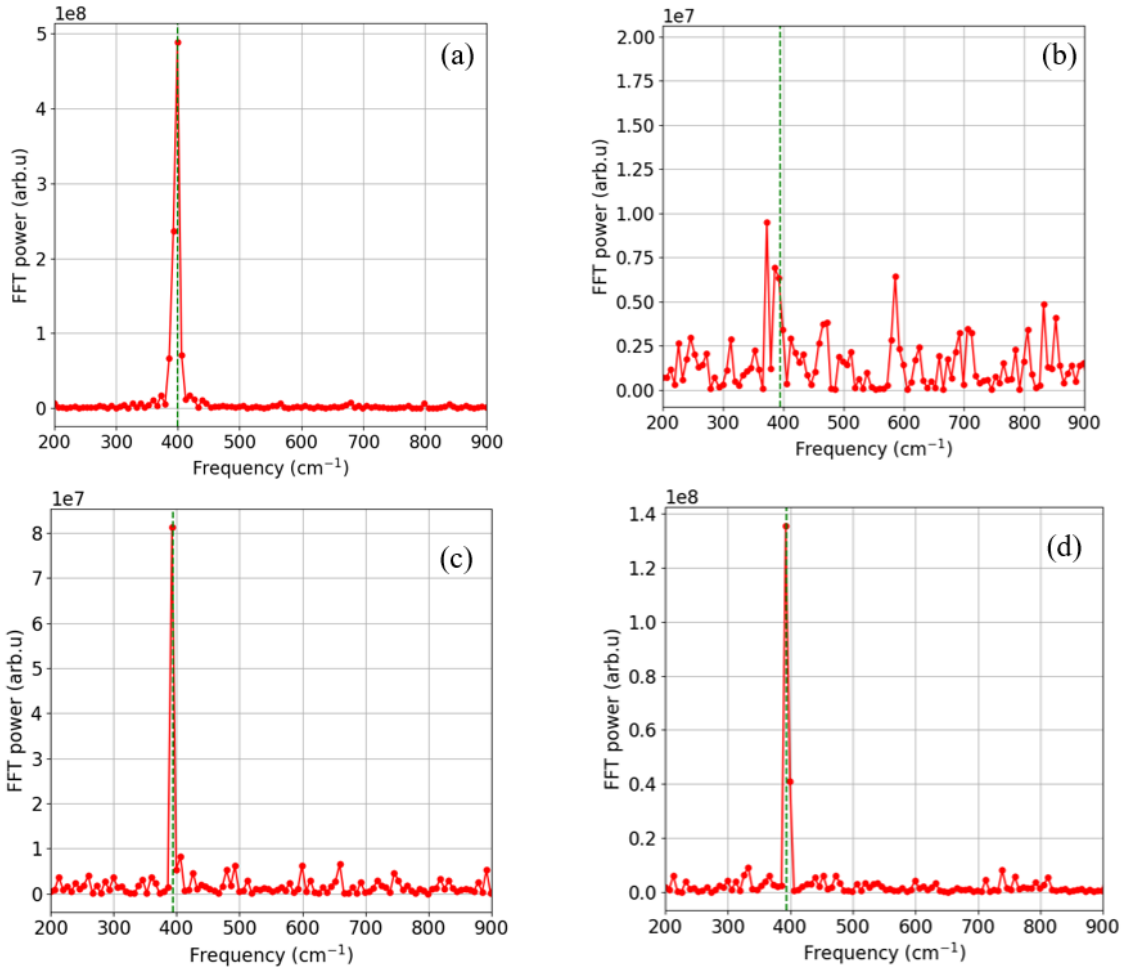

Figure 4.22 The FFT spectra correspond to delay-dependent yield of SO_2^{++} gated in a 5 ps delay window up to (a) 5 ps (b) 10 ps (c) 15 ps, and (d) 20 ps.

As shown in Figure 4.22, the 400 cm^{-1} frequency peak shows the highest amplitude in the initial delay up to 5 ps (a). In the 5-10 ps delay window (b), the FFT signal has disappeared, and it is at the noise level of the signal. After 10 ps, oscillations reappear (c and d) and the peak height increases. However, the amplitude of the FFT peak height at later delays (d) does not grow as high in the first 5 ps window (a).

To further investigate the differences in the amplitude of the 400 cm^{-1} frequency and to observe how the corresponding frequency peak completely dies out and starts to reappear, a sliding delay window FFT of 1850 fs window size was performed, with the end position of the window varying from 2 ps to 20 ps.

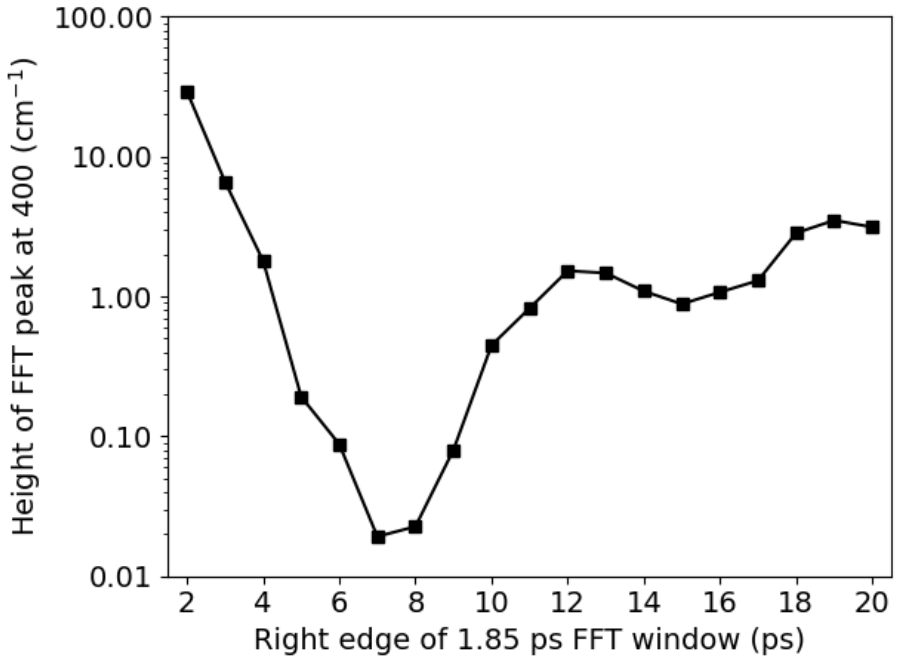

Figure 4.23 Peak height of the v_2^+ frequency obtained by sliding window FFT spectra of a delay window of 1850 fs for SO_2^{++} ions.

Figure 4.23 shows the height of the 400 cm^{-1} peak as a function of the FFT window end position. The distribution indicates that the height of the frequency peak initially decreases and completely dies out starting from 4 ps, and reappears after 9 ps.

These observations in the FFT spectra of the delay-dependent yield of SO_2^{++}, could be a signature of the vibrational wave packet dephasing and subsequent revival discussed in section 2.2. The phenomenon of vibrational revivals is well-understood for diatomic molecules but is much less studied in polyatomic systems with an additional degree of freedom [50]. As shown in Figure 4.15, in the previous studies of photoelectron (PE) spectra of SO_2 [45],[51] the first seven vibrational levels were found to have similar frequencies around ~400 cm^{-1}, with almost equal spacing of ~2.4 cm^{-1} between the adjacent vibrational levels. According to the discussion on vibrational revival time and vibrational level spacing in the theory section, the expected revival time of the ionic wave packet should be around ~27 ps, defined by the inverse of half of the vibrational level spacing. Correspondingly, the observed reappearance of the 400 cm^{-1} likely corresponds to the half revival, which is expected to be centered around ~13.5 ps.

Surprisingly, this behavior was not observed on any other channel so far. In all other channels, the vibrational bending frequency (400 cm^{-1}) dies out (wave packet dephasing) soon after 2 ps, but it does not show any signature of revival.

In the sliding delay window analysis, only in the SO_2^{++} FFT spectra, the peak height of the revival showed a good contrast at large delays compared to 2 ps window. However, compared to the peak height of the initial signal at 2 ps in all other channels, if the revival were to be observed, the peak height of the revival frequency would be at the noise level. Hence, having insufficient contrast in the FFT spectrum might be a reason why we do not see the signature of revivals in other channels.

Interestingly, in Figure 4.23, we observe the ~400 cm^{-1} FFT peak height reach a minimum, and after it reappears, it does not go to a minimum again within the 20 ps delay window. A possible scenario explaining this behavior would be, the level of incoherence of the vibrational levels involved due to the mismatch of their phases seems to be higher than the complete destructive interference of their phases. Coupling to different degrees of freedom (like rotational motion) might also play a role here. While in [19] it was shown that the rotational dynamics, which we will discuss later on, influences the yields of various fragmentation channels in 800 nm pump- 800 nm probe experiments, at this point, we do not have a clear picture of how it could influence the long-term evolution of the vibrational wave packet in SO_2^+.

As shown in Figure 4.15, the first seven vibrational levels are almost equally spaced, but exhibit a small but clear shift towards smaller frequencies for larger values of v_2 [45],[51]. Therefore, one part of the motivation for performing a long delay scan up to 20 ps delay with 10-fs step size was to see if it is possible to resolve individual vibrational levels of the ionic ground state of SO_2^+. Figure 4.24 shows the FFT spectrum corresponding to the delay-dependent yield of SO_2^{++} up to 20 ps delay window. The prominent peak is centered at 395 cm^{-1}, while there are three more subpeaks centered around 384.8, 389.7, and 399.8 cm^{-1} with a resolution of $\pm 1.7\ cm^{-1}$. While the overall range of the spectrum matches the expected values shown in Figure 4.15, the current FFT resolution is still not good enough to clearly resolve the vibrational levels contributing to the nuclear wave packet in SO_2^+ ionic ground state.

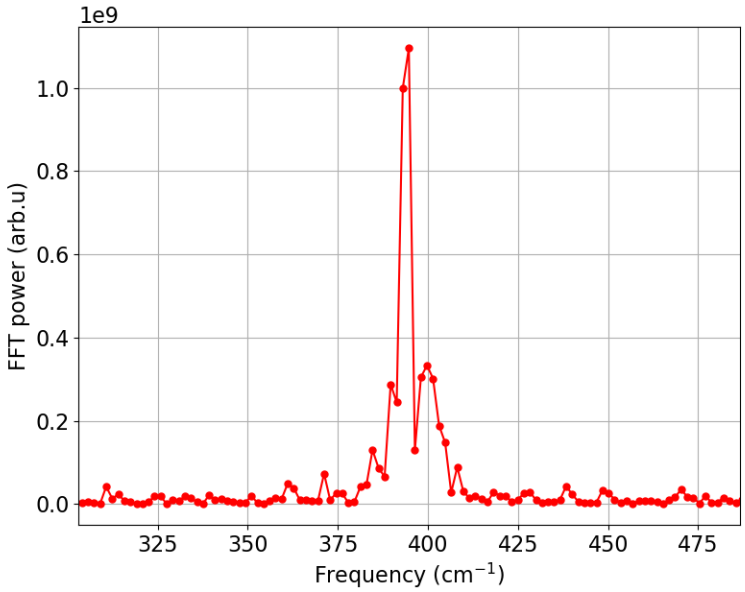

Figure 4.24 Resolving different vibrational levels of SO_2^+ ionic ground state.

Due to the bending vibration of the sulfur dioxide molecular ion at different delays, the angle between the two oxygen changes from small angles to larger angles, resulting in oscillatory motion in the delay-dependent angle. This observation could be observed in the delay-dependent mean angle of the two O^+ ions (<O^+, O^+ >) in the triply charged $S^+ + O^+ + O^+$ final state. Other than this prominent bending vibrational motion (v_2^+), the delay-dependent yield of the same three-body breakup channel showed a signature of symmetric stretching vibrational motion (v_1^+) as well.

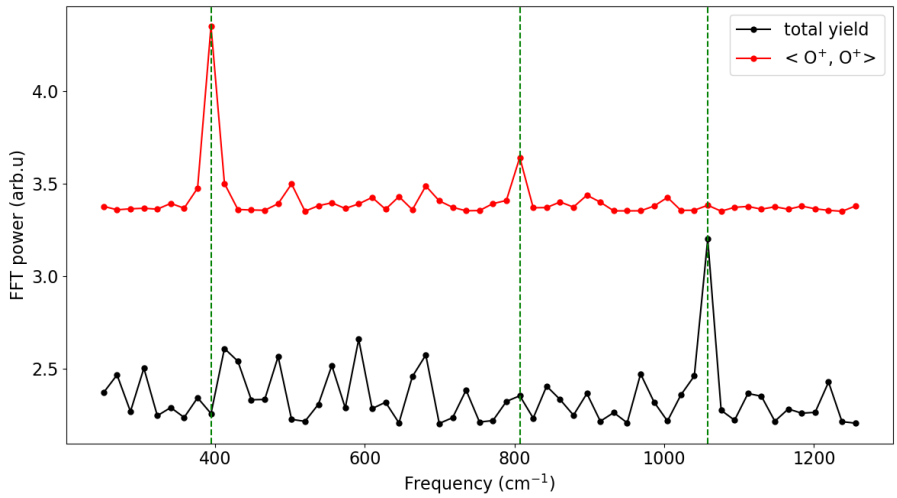

Figure 4.25 Delay-dependent mean angle (red) and total yield (black) of the $S^+ + O^+ + O^+$ three-body breakup channel. In both cases, the KER> 14 eV was selected to remove the events corresponding to molecules undergoing dissociation.

As shown in Figure 4.25, the FFT of the delay-dependent mean angle between the two O^+ ion momenta exhibits a strong peak at ~400 cm^{-1}, which corresponds to the v_2^+ vibrational mode and a weak peak at ~800 cm^{-1}, which corresponds to the first overtone of the ionic bending vibrational frequency $(2v_2^+)$. Interestingly, in the delay-dependent total yield of the same triply charged final state, we see a peak at ~1058 cm^{-1} in the FFT spectrum. This peak is identified as the frequency of the symmetric stretching vibrational mode v_1^+ of SO_2^+ in the ground state [52]. Figure 4.26 explains the absence of the frequency peak of v_2^+ mode (~400 cm^{-1}) in the FFT spectrum corresponding to the total delay-dependent yield. At the delays when the two O^+ ions come closer together, forming small angles between them, we see a maximum in the yield. However, the corresponding delay-dependent yield for large angles shows a minimum. As shown in Figure 4.26, due to the bending motion of the two O^+ ions, we see a clear peak at ~400 cm^{-1} in the FFT spectra for delay-dependent yield gated on small (blue) and large angles (black). This out-of-phase relation in the yield at small and large angles explains the reason for the absence of the v_2^+ frequency peak in the FFT spectrum (red curve in Figure 4.26), when the delay-dependent yield corresponding to the total angle range is taken. However, the v_1^+ frequency peak, in the total yield, starts to appear when gated on a range between small and large angles (green curve in Figure 4.26).

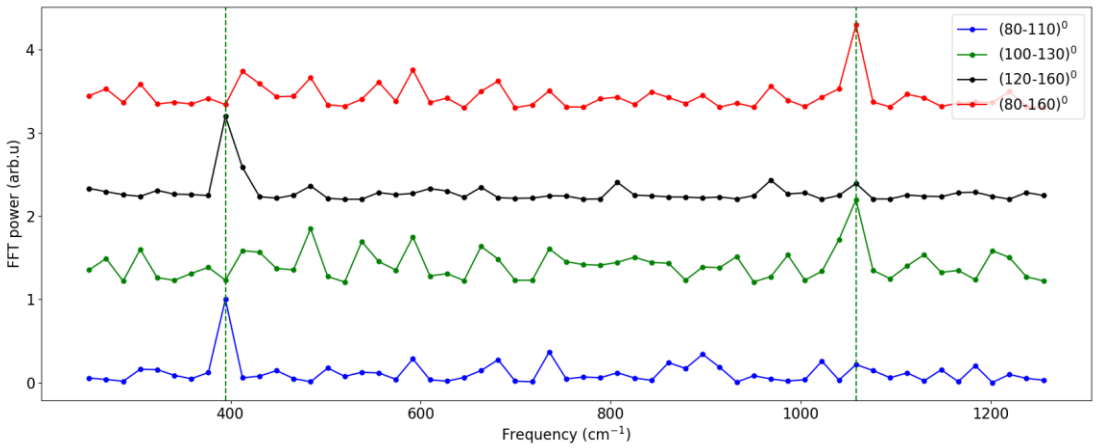

Figure 4.26 FFT spectrum of the delay-dependent yield of the $S^+ + O^+ + O^+$ channel gated on different angle ranges between the two O^+ ions' momentum vectors. Only the events of KER> 14 eV were selected.

Even though the most prominent difference of the reaction coordinate between the ground and ionic state is the bond angle (~119^0 and ~133^0), there is a slight difference between the equilibrium bond lengths (1.414 Å and 1.401 Å) of the two states as well. This difference might induce some symmetric stretching in the molecules. Other than that, both v_1^+ and v_2^+ belong to the same A_1 irreducible symmetry representation; there can be some coupling between the two modes under C_{2v} symmetry, which might also result in symmetric stretching in the bond length. However, if the experimental technique (i.e., photoelectron (PE) spectra) used to resolve these bands lacks the resolution to distinguish these modes, the weak transition (v_1^+) may be blended in or hidden, so only the v_2^+ transition appears prominently. In the experimental study described in [52], they have shown the observation of both symmetric bending and symmetric stretching vibration modes frequencies by employing high-resolution PE spectra using coherent extreme ultraviolet radiation. Even though it is not clear why the v_1^+ frequency was observed only in the triply charged channel in our experiment with the 400 nm pump pulse, the empirical conclusion here is that the total yield of the $S^+ + O^+ + O^+$ channel (or, in other words, ionization probability to this final state) does not depend much on the bending vibrations (bond angle), but changes with the symmetric stretching vibrations (bond length change).

4.4 Rotational Wave Packet Dynamics

In the delay-dependent yield of different final states, we could observe that there is either an increase or a decrease in the yield before it flattens out (neglecting the enhancement in the overlap region). This signature was visible in both 400 nm and 800 nm pump experiments. To confirm whether this modulation in the delay-dependent yield corresponds to rotational dynamics of the molecule, we look at the molecular alignment parameter $< cos^2\theta >$ for different final states. Figure 4.27 shows the delay-dependent yield and the corresponding $< cos^2\theta >$ of the $SO^+ + O^+$ two-body breakup channel. The delay window for the 800 nm pump experiment was only up to 2 ps.

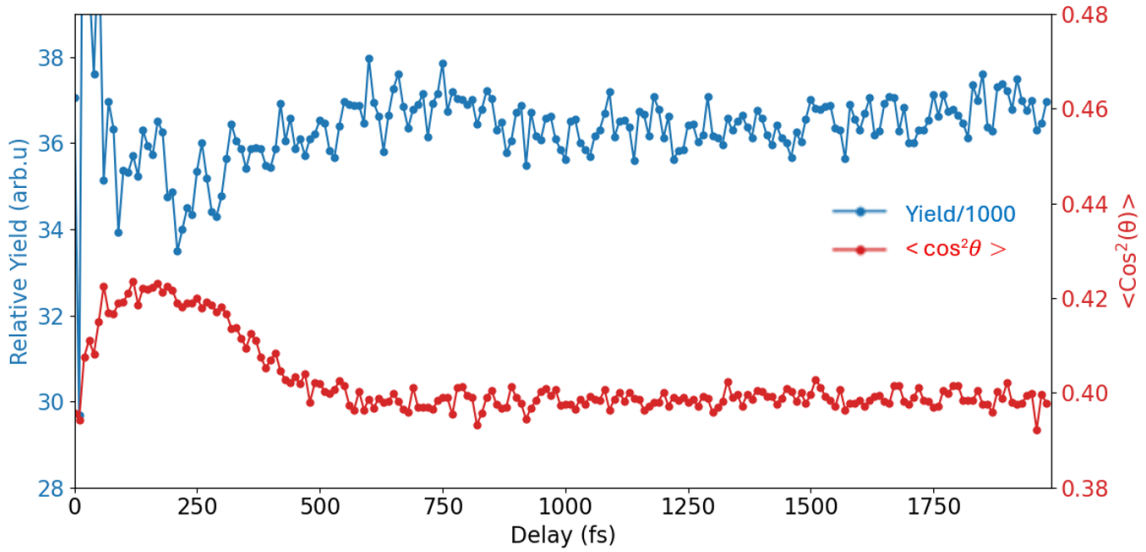

Figure 4.27 800 nm pump delay-dependent yield (yield/1000) (blue) of the $SO^+ + O^+$ channel and delay dependence of $< \cos^2\theta >$ (red) where θ is the angle between the laser polarization direction and the recoil axis of the two-body breakup channel. (From 800 nm pump and 800 nm probe experiment scanned up to 2 ps delay)

According to Figure 4.27, the timescale of the initial decrease in the delay-dependent yield matches the enhancement observed in the $< cos^2\theta >$ distribution. Hence, the observed yield variation can be attributed to because of the initial alignment of the pump-induced rotational wave packet. The initial enhancement in the $< cos^2\theta >$ tells that the pump pulse initially aligns the molecule parallel to the laser polarization direction. However, the decrease in the measured delay-dependent yield of the two-body breakup channel indicates that CE of the molecule resulting in the SO^+ and O^+ fragments is less likely to happen during the parallel alignment of the molecule.

After 500 fs, the initial alignment deteriorated because of the rotational wave packet dephasing. However, the 800 nm pump experiment was only carried out up to a 2 ps delay, which prevents observing any signatures of rotational revival of the wave packet. Figure 4.28 shows the same observables for the same channel with the 400 nm pump scanned up to a 20 ps time delay.

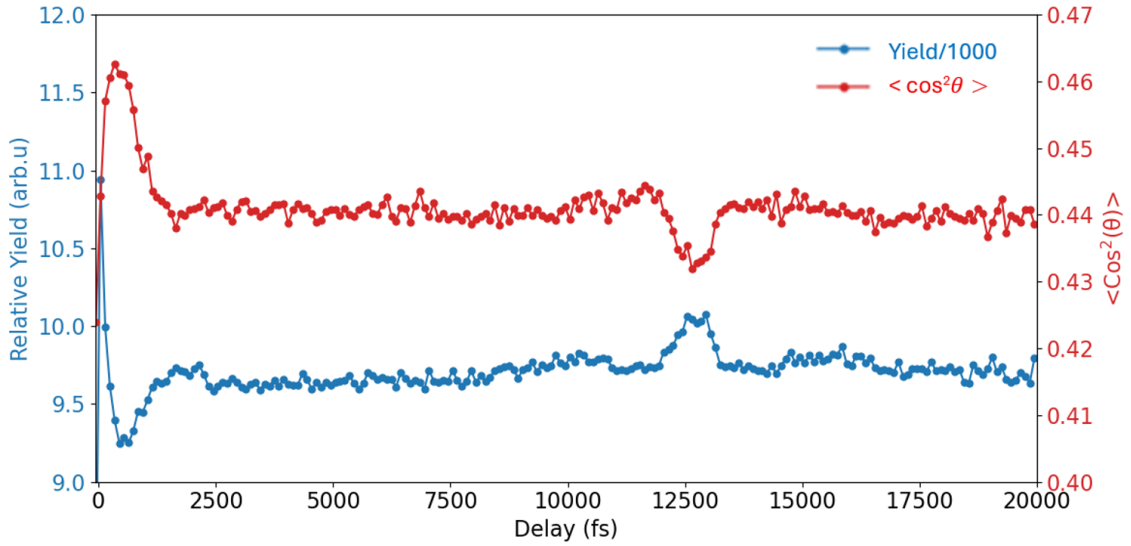

Figure 4.28 400 nm pump delay-dependent yield (yield/1000) (blue) of the $SO^+ + O^+$ channel and delay dependence $< \cos^2\theta >$ (red) where θ is the angle between the laser polarization direction and the recoil axis of the two-body breakup channel. (400 nm pump and 800 nm probe experiment scanned up to 20 ps delay with 10fs step size. For the visual convenience of the plots, a 100fs bin size was employed.)

According to Figure 4.28, we can observe a similar pattern of decrease and increase in the delay-dependent yield and $< cos^2\theta >$ respectively. This shows the same kind of parallel alignment of the molecule with the laser polarization direction initially. There is also a clear signature of dephasing in the rotational wave packet. Interestingly, around ~13 ps, we can observe signatures of the realignment of the molecule. At this delay, molecules show anti-alignment with the laser polarization axis. In this perpendicular arrangement, the CE and fragmentation of the molecules producing the SO^+ and O^+ fragments are more likely to happen. This can be observed in the increase of the delay-dependent yield of the two-body breakup channel around ~13 ps. Expected rotational revival of the SO_2 is found to be around ~26 ps [54]. Hence, what we observe around ~13 ps could be a clear signature of the fractional (half) revival of the rotational wave packet of SO_2.

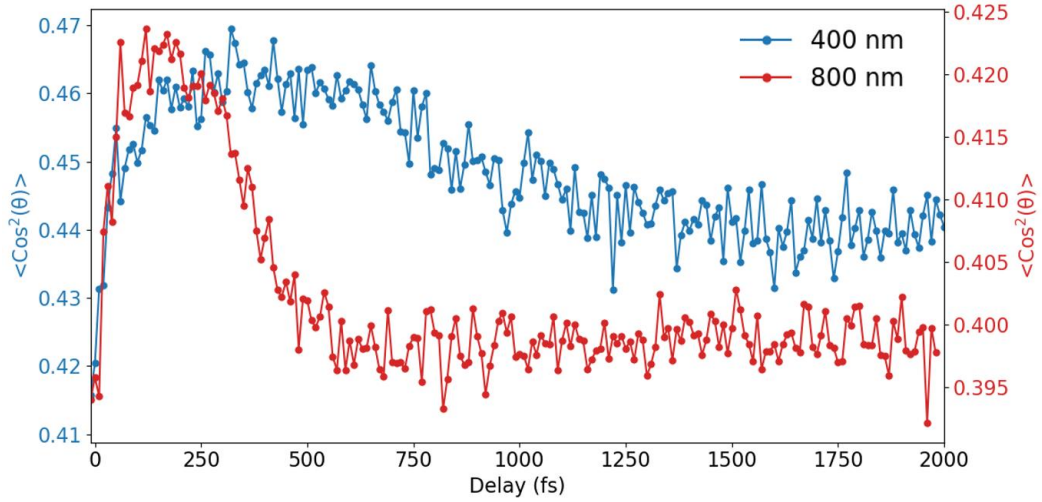

Figure 4.29 Comparison of the delay dependence of $< \cos^2\theta >$ where θ is the angle between the laser polarization direction and the recoil axis of the $SO^+ + O^+$ two-body breakup channel. Only the events up to 2 ps delay are shown here.

As shown in Figure 4.29, in both pump pulses, the initial alignment deteriorated because of the rotational wave packet dephasing. However, the time scale of this dephasing was found to be significantly longer for the shorter wavelengths. For the 800 nm pump, dephasing was found to be around ~500 fs, and for the 400 nm was around ~1500 fs. Since faster dephasing of the rotational wave packet corresponds to a broader distribution of the populated vibrational states, the observed differences in the time scale are most likely due to the narrower distribution of the populated rotational states for the 400 nm pump. Therefore, a shorter time in dephasing tells the population of a larger number of rotational states, while a longer time tells the population of a smaller number of rotational states.

4.5 Summary

In this chapter, we have considered nuclear wave packet dynamics in laser-irradiated SO_2 molecules, which were excited by 800 nm or 400 nm pulses and, in both cases, probed with a second, more intense 800 nm pulse. Almost all the FFT spectra observed in both experiments are dominated by the frequency of ~ 400 cm^{-1}, which corresponds to the ionic ground-state bending vibrational frequency (v_2^+) of SO_2^+. In addition, for the case of an 800 nm pump, in several channels, clear signatures of neutral ground state bending vibrational frequency v_2 at ~ 520 cm^{-1}, and the first overtone of v_2^+ at ~ 800 cm^{-1} have been observed. With a 400 nm probe, in the yield of triply charged $O^+ + O^+ + S^+$ coincidence channel, we also observed the 1058 cm^{-1} frequency, which reflects the symmetric stretching (v_1^+) mode frequency of the ground-state SO_2^+. The summary of the vibrational frequencies observed in this work is shown in Table 1.

Table 1 Ground state frequencies for neutral and ionic geometry of SO_2 molecules for different vibrational modes. Here, the frequencies are given in cm^{-1}.

Modes	O-S-O bending	S-O symmetric stretching
Molecule		
SO_2 ($\tilde{X}^1A_1$)	520	-
SO_2^+ ($\tilde{X}^2A_1$)	395	1058

For ionic bending vibrations at both pump wavelengths, CEI using $O^+ + O^+ + S^+$ channel shows that the created ionic wave packet initially moves towards larger angles, as expected from the neutral and ionic ground-state PECs sketched in Figure 4.12. Therefore, the IFFTs of this gated frequency enabled experimental determination of the evolution of ionization and/or fragmentation probability as a function of the angle between the two O^+ momenta (and, thus, indirectly, O-S-O bond angle) for a specific final state. However, understanding the reasons for this dependence on each channel will require more detailed theoretical modelling.

The IFFT plots obtained by filtering on the v_2 frequency of the neutral molecule showed that the yield of all channels where this frequency is observed initially increases. Since the ionization potential of SO_2 decreases at large angles, we consider this as an indication that the neutral-state vibrational wave packet, similar to the ionic case, initially moves towards larger angles. Based on the previous results on exciting vibrational wave packets in the ground state of

neutral molecules [60, 66, 67, 68, 69], this suggests two-photon Raman excitation as a dominant mechanism triggering SO_2 bending vibrations. The absence of such neutral wave packet motion in the experiments with 400 nm pump is consistent with this picture since the cross section for off-resonant two-photon Raman scattering decreases for higher photon energies, and the photon energy of 400 nm is twice as large as for 800 nm. However, our expectations for the wave packet phase (i.e., initial direction of motion) are deduced from the consideration of diatomic molecules [66, 67, 68] or stretching vibrations of polyatomic systems [60, 69], and it is not completely clear to what extent they apply to bending vibrations observed in this work. Therefore, at this stage, an alternative Lochfrass mechanism (discussed in section 4.2.3.2) cannot be reliably excluded as the reason behind the observed bending vibrations of neutral SO_2. Unambiguous identification of the dominant mechanism will require more elaborate modelling of SO_2 ionization and fragmentation as a function of molecular geometry.

Besides the absence of the neutral v_2 frequency at ~ 520 cm^{-1}, two main features in the vibrational dynamics triggered with 400 nm pump were not observed in 800 nm pump – 800 nm probe experiments. First, while in all channels studied with a 400 nm pump, the v_2^+ mode frequency dies out completely between 2 and 4 ps. For SO_2^{2+} yield we observe the reappearance of this feature at larger delays. While the exact origin of this behavior and its channel specificity remain unclear, this could be a signature of the vibrational wave packet dephasing and subsequent revival. Considering the vibrational level spacing of the anharmonic potential, we could find the half revival of the corresponding wave packet at ~ 13 ps, which is consistent with our observations. Compared to the peak height of the original frequency of v_2^+, if the revivals were to be observed in other channels, then the peak height of the revival frequency would be at the noise level. Hence, having insufficient contrast in the FFT spectrum might be a reason why we do not see the signature of revivals in other channels. Even though we observed signatures of dephasing with both pump wavelengths, for the 800 nm pump, our delay scanning window was not sufficient to observe signatures of vibrational revival or lack thereof.

Second, besides the strong v_2^+ mode frequency, in the experiment with 400 nm pump, we could observe a weak feature corresponding to symmetric stretching (v_1^+) mode frequency in the total yield of the $S^+ + O^+ + O^+$ channel. This frequency also died out soon after 2 ps and did not reappear or was not observed in any other channels. Why this frequency was observed after 400

nm excitation and was not found in the experiments with 800 nm pump remains unclear and represents an interesting question for future analysis and theoretical modelling.

Finally, for both pump wavelengths, we observed a weak, yet distinct impulsive alignment of the molecules induced by the pump laser pulse, evident from the time evolution of the angular distributions of the fragments with respect to the linear laser polarization. With both 400 nm and 800 nm pump wavelengths, the initial alignment deteriorated due to the dephasing of the rotational wave packet. However, with the 400 nm pump pulse, the time scale of dephasing (~1.5 ps) was significantly longer than that of the 800 nm pump wavelength (~0.5 ps). Narrow distribution of the populated rotational states most likely would be the reason why we see longer dephasing time with the 400 nm pump pulse. Interestingly, we could also observe a signature of half revival of the rotational wave packet in our pump-probe experimental data with the 400 nm pump extended to 20 ps delay window.

Chapter 5 - Conclusion

This thesis mainly focuses on studying strong-field-induced nuclear dynamics of molecules. To capture such ultrafast dynamics in real time, we employed two different femtosecond laser systems at the J. R. Macdonald Lab. Exploiting a basic pump-probe scheme, we used Coulomb Explosion Imaging, combined with time-resolved ion mass spectrometry and channel-selective Fourier analysis, to probe nuclear wave-packet dynamics in sulfur dioxide molecules irradiated by visible and NIR laser pulses. For these measurements, we employed COLd Target Recoil Ion Momentum Spectroscopy (COLTRIMS) as an experimental probe tool.

The first part of this thesis discussed the commissioning of a new COLTRIMS system with the newly installed 100 kHz Konza laser system. Besides the higher repetition rate of the laser, compared to the other COLTRIMS apparatuses available at JRML, this setup can potentially provide higher momentum resolution in the experimental data. This improvement is mainly due to the thin-jet configuration of the setup, which enables a low target density with a very narrow jet, resulting in lower background pressure and a small interaction region with the laser. After baking the main chamber and the jet dumps (catchers), this apparatus has reached ultra-high vacuum conditions in the main chamber as low as 4.5×10^{-11} Torr, which is lower than the pressures that could be achieved in other COLTRIMS systems available at the JRML. Commissioning experiments on CH_2ClI molecules discussed in this thesis showed that with this new setup operating at 100 kHz, a significant amount of 5-fold coincidence events can be collected in less than 90 minutes.

The second part of this thesis focuses on the study of strong-field-induced molecular wave packet dynamics in sulfur dioxide (SO_2) molecules. The two pump-probe experiments described in this section were conducted using an older COLTRIMS instrument coupled with two different femtosecond laser systems, operating at 3 kHz and 10 kHz repetition rates. In both experiments, the information on the time evolution of the created molecular wave packets was deduced by performing Fourier analysis on the delay-dependent yields of several singly, doubly, and triply charged final states of the molecule. We traced signatures of bending vibrations of the molecule in the ionic and neutral ground states, although the latter could be observed only in the experiments with the 800 nm pump pulse. In the experiments with the 400 nm pump, a longer delay scan window enabled the observation of vibrational wave packet dephasing and its subsequent

fractional revival. If this finding is confirmed, this might be the first observation of vibrational revivals in a polyatomic molecule. Moreover, for both pump wavelengths, we observed weak but clear impulsive alignment of the molecules and subsequent dephasing of the rotational wave packet. The timescale of this dephasing becomes slower for 400 nm excitation, most likely reflecting the narrower distribution of the populated rotational states. Finally, with the 400 nm pump, where the delay was scanned up to a 20 ps delay, we could also observe a signature of half revival of the rotational wave packet at ~13 ps. Interestingly, this time roughly matches the position of vibrational half-revival.

In conclusion, the work discussed in this thesis provides a significant amount of new information about light-induced nuclear dynamics in molecules. Also, our experimental results have shown the advantage of having a longer delay scan window for resolving nuclear dynamics, as it enables us to see longer-scale wave packet dynamics, which reveal many important quantum mechanical phenomena such as dephasing and revival. Other than that, a longer delay window can potentially improve the resolution of the Fourier spectra as well. The resolution in current experiments, though, was limited by the statistics and the number of delay steps within the scan range. The experimental results on SO_2 molecules were obtained with 3 kHz and 10 kHz laser systems for measurements with 400 nm and 800 nm pump, respectively. To avoid most of these limitations, we can exploit the advantage of having a higher repetition rate of the laser and employ the newly commissioned COLTRIMS setup available with the 100 kHz laser at the JRML for future experiments. This combination will allow us to perform pump-probe experiments with a small step size, good statistics, and a larger delay range, enabling simultaneous measurements of high-resolution Fourier spectra and Coulomb explosion patterns based on multi-coincidence ion detection. With a 100 kHz laser, all this can be achieved while reducing the data collection time in the experiments.

Bibliography

[1] A. A. Ischenko, . P. M. Weber and D. R. Miller, "Capturing Chemistry in Action with Electrons: Realization of Atomically Resolved Reaction Dynamics," *Chemical Reviews,* vol. 117, no. 16, pp. 11066-11124, 2017.

[2] M. F. Holick, "Skin: Site of the Synthesis of Vitamin D and a Target Tissue for the Active Form, 1, 25-Dihydroxy vitamin D_3," *Annals of the New York Academy of Sciences,* vol. 548, no. 1, pp. 14-26, 1998.

[3] S. Hsieh and J. H. Eland, "Reaction dynamics of three-body dissociations in triatomic molecules from single-photon double ionization studied by a time-and position-sensitive coincidence method," *Journal of Physics B: Atomic, Molecular and Optical Physics,* vol. 30, no. 20, p. 4515, 1997.

[4] L. Zhou, C. Y. Chang, Q. Z. Yin, and J. M. William, "Evidence for direct molecular oxygen production in CO_2 photodissociation," *Science,* vol. 346, no. 6205, pp. 61-64, 2014.

[5] D. Y. Yang and S. Y. Sheu, "Pump–probe spectroscopy of photoinduced charge transfer reactions in solution," *The Journal of Chemical Physics,* vol. 106, no. 3, pp. 9427-9438, 1997.

[6] S. X. Hu and L. A. Collins, "Attosecond pump probe: exploring ultrafast electron motion inside an atom," *Physical Review Letters,* vol. 96, no. 7, p. 073004, 2006.

[7] A. D. Dutoi and L. S. Cederbaum, "Time-resolved pump-probe spectroscopy to follow valence electronic motion in molecules: Application," *Physical Review A,* vol. 90, no. 2, p. 023414, 2014.

[8] B. Motohiro, K. Ohta, S. Yamaguchi, S. Hirai, and K. Tominaga, "Vibrational dynamics of hydrogen-bonded complexes in solutions studied with ultrafast infrared pump-probe spectroscopy," *Accounts of Chemical Research,* vol. 42, no. 9, pp. 1259-1269, 2009.

[9] G. Rajib, A. K. Mora, S. Nath, and K. Deepak, "Ultrafast Dynamics of Hydrogen Bond Breaking and Making in the Excited State of Fluoren-9-one: Time-Resolved Visible Pump–IR Probe Spectroscopic Study," *The Journal of Physical Chemistry B,* vol. 121, no. 5, pp. 1068-1080, 2017.

[10] J. C. Polanyi and A. H. Zewali, "Direct observation of the transition state," *Accounts of Chemical Research,* vol. 28, no. 3, pp. 119-132, 1995.

[11] A. H. Zewail, "Femtochemistry: Atomic-scale dynamics of the chemical bond," *The Journal of Physical Chemistry A,* vol. 104, no. 24, pp. 5660-5694, 2000.

[12] A. Stolow, "Femtosecond time-resolved photoelectron spectroscopy of polyatomic molecules," *Annual Review of Physical Chemistry,* vol. 54, no. 1, pp. 89-119, 2003.

[13] A. Stolow, "Time-resolved photoelectron spectroscopy: Non-adiabatic dynamics in polyatomic molecules," *International Reviews in Physical Chemistry,* vol. 22, no. 2, pp. 377-405, 2003.

[14] T. Gejo, N. Tatsuru, N. Takahiro, T. Kenta, T. Yoshihito, N. Akinobu, N. Kiyonobu, R. Yamamura, N. Futamata, T. Suenaga, and O. Takahashi, "Dissociation and ionization dynamics of CF_3I and CH_3I molecules via pump-and-probe experiments using soft x-ray free-electron laser," *Journal of Physics B: Atomic, Molecular and Optical Physics,* vol. 54, no. 1, p. 144004, 2021.

[15] H. Stapelfeldt, E. Constant, H. Sakai, and P. B. Corkum, "Time-resolved Coulomb explosion imaging: A method to measure structure and dynamics of molecular nuclear wave packets," *Physical Review A,* vol. 58, no. 1, p. 426, 1998.

[16] F. Légaré, K. F. Lee, I. V. Litvinyuk, P. W. Dooley, S. S. Wesolowski, P. R. Bunker, P. Dombi, F. Krausz, A. D. Bandrauk, D. M. Villeneuve, and P. B. Corkum, "Laser Coulomb-explosion imaging of small molecules," *Physical Review A—Atomic, Molecular, and Optical Physics,* vol. 71, no. 1, p. 013415, 2005.

[17] A. Assion, M. Geisler, J. Helbing, V. Seyfried, and T. Baumert, "Femtosecond pump-probe photoelectron spectroscopy: Mapping of vibrational wave-packet motion," *Physical Review A,* vol. 54, no. 6, p. R4605, 1996.

[18] H. V. Lam, A. S. Venkatachalam, S. Bhattacharyya, K. Chen, K. Borne, E. Wang, R. Boll, T. Jahnke, V. Kumarappan, A. Rudenko, and D. Rolles, "Differentiating three-dimensional molecular structures using laser-induced coulomb explosion imaging," *Physical Review Letters,* vol. 132, no. 12, p. 123201, 2014.

[19] H. V. Lam, V. H. Hoang, A. S. Venkatachalam, S. Bhattacharyya, K. Chen, S. Jacod, S. Kudagama, T. T. Nguyen, D. Rolles, U. Thumm, and A. Rudenko, "Simultaneous imaging of vibrational, rotational, and electronic wave-packet dynamics in a triatomic molecule," *Physical Review A,* vol. 111, no. 6, p. L061101, 2025.

[20] J. J. Larsen, K. Hald, N. Bjerre, H. Stapelfeldt, and T. Seideman, "Three-dimensional alignment of molecules using elliptically polarized laser fields," *Physical Review Letters,* vol. 85, no. 12, p. 2470, 2000.

[21] J. Ullrich, R. Moshammer, R. Dörner, O. Jagutzki, V. Mergel, B. H. Schmidt and L. Spielberger, "Recoil-ion momentum spectroscopy," *Journal of Physics B: Atomic, Molecular and Optical Physics,* vol. 30, no. 13, p. 2917, 1997.

[22] R. Dörner, V. Mergel, O. Jagutzki, L. Spielberger, J. Ullrich, R. Moshammer and B. H. Schmidt, "Cold target recoil ion momentum spectroscopy: a 'momentum microscope'to view atomic collision dynamics," *Physics Reports,* vol. 330, no. 2-3, pp. 95-192, 2000.

[23] K. Lin, X. Hu, S. Pan, F. Chen, Q. Ji, W. Zhang, H. Li, J. Qiang, F. Sun, X. Gong, and H. Li, "Femtosecond resolving photodissociation dynamics of the SO_2 molecule," *The Journal of Physical Chemistry Letters,* vol. 11, no. 8, pp. 3129-3135, 2020.

[24] D. Rösch, Y. Xu, H. Guo, X. Hu, and D. L. Osborn, "SO_2 Photodissociation at 193 nm Directly Forms S (^{3}P)+ O_2 ($^3\Sigma_g$–): Implications for the Archean Atmosphere on Earth," *The Journal of Physical Chemistry Letters,* vol. 14, no. 12, pp. 3084-3091, 2023.

[25] K. Amini, "A tutorial review: probing molecular structure and dynamics with CEI and LIED," *arXiv preprint arXiv:2112.10029,* 2021.

[26] Z. Vager, R. Naaman and E. P. Kanter, "Coulomb explosion imaging of small molecules," *Science,* vol. 244, no. 4903, pp. 426-431, 1989.

[27] L. V. Keldysh, "Ionization in the field of a strong electromagnetic wave," *Soviet Physics JETP,* vol. 20, p. 1307, 1965.

[28] L. Gallmann, I. Jordan, H. J. Wörner, L. Castiglioni, M. Hengsberger, J. Osterwalder, C. A. Arrell, M. Chergui, E. Liberatore, U. Rothlisberger, and U. Keller, "Photoemission and photoionization time delays and rates," *Structural Dynamics,* vol. 4, no. 6, 2017.

[29] H. Mustroph, "Potential-Energy Surfaces, the Born–Oppenheimer Approximations, and the Franck–Condon Principle: Back to the Root," *ChemPhysChem,* vol. 17, no. 17, pp. 2616-2629, 2016.

[30] V. P. Gupta, Principles and applications of quantum chemistry, Academic Press, 2015.

[31] R. Schinke, Photodissociation dynamics: spectroscopy and fragmentation of small polyatomic molecules, Cambridge University Press, 1995.

[32] H. Yuan, Y. Gao, B. Yang, S. Gu, H. Lin, D. Guo, J. Liu, S. Zhang, X. Ma, and S. Xu, "Coulomb Explosion Imaging of Complex Molecules Using Highly Charged Ions," *Physical Review Letters,* vol. 8, no. 133, p. 193002, 2024.

[33] S. Eckart, "Strong field-induced quantum dynamics in atoms and small molecules," *Journal of Physics B: Atomic, Molecular and Optical Physics,* vol. 57, no. 20, p. 202001, 2024.

[34] X. Li, X. Yu, P. Ma, X. Zhao, C. Wang, S. Luo, and D. Ding, " Ultrafast Coulomb explosion imaging of molecules and molecular clusters," *Chinese Physics B,* vol. 31, no. 10, p. 103304, 2022.

[35] K. Schnorr, "XUV Pump-Probe Experiments on Electron Rearrangement and Interatomic Coulombic Decay in Diatomic Molecules," PhD Thesis, Ruprecht-Karls-Universität, Heidelberg, 2014.

[36] X. Ren, A. M. Summers, A. Vajdi, V. Makhija, C. W. Fehrenbach, N. G. Kling, K. J. Betsch, Z. Wang, M. F. Kling, K. D. Carnes, and I. Ben-Itzhak, "Single-shot carrier-envelope-phase tagging using an f–2f interferometer and a phase meter: a comparison," *Journal of Optics,* vol. 19, no. 12, p. 124017, 2017.

[37] S. H. Zavareh, Ultrafast molecular imaging studies with laser-induced electron diffraction at high repetition rates, PhD thesis, Kansas State University, 2024.

[38] "OPCPA – the key to power scaling and flexibility," CLASS 5 Photonics, October 2023. [Online]. Available: https://www.class5photonics.com/opcpa/.

[39] K. K. Hamamatsu Photonics, "MCP (Microchannel Plate) assembly," December 2021. [Online]. Available: https://www.hamamatsu.com/content/dam/hamamatsu-photonics/sites/documents/99_SALES_LIBRARY/etd/MCP_assembly_TMCP0003E.pdf.

[40] RoentDek Handels GmbH, "MCP delay line detector manual," February 2024. [Online]. Available: https://www.roentdek.com/manuals/MCP%20Delay%20Line%20manual.pdf.

[41] RoentDek Handels GmbH, "The Constant Fraction Discriminators CFD8c, CFD7x, CFD4c, CFD1c and CFD1x," [Online]. Available: https://www.roentdek.com/manuals/CFD%20Manual.pdf.

[42] RoentDek Handels GmbH, "CoboldPC," [Online]. Available: https://www.roentdek.com/manuals/CoboldPC%20UserManual%20(6.2.90.2).pdf.

[43] F. Ziaee, Imaging nuclear motion during the photofragmentation of halomethane molecules triggered by ultraviolet light, PhD thesis, Kansas State University, 2022.

[44] B. Kaderiya, Imaging photo-induced dynamics in halomethane molecules with coincident ion momentum spectroscopy, PhD thesis, Kansas State University, 2021.

[45] L. Wang, Y. T. Lee and D. A. Shirley, "Molecular beam photoelectron spectroscopy of SO2: geometry, spectroscopy, and dynamics of SO_2^+," *The Journal of Chemical Physics,* vol. 87, no. 5, pp. 2489-97, 1987.

[46] T. Shimanouchi, "Sulfur Dioxide," NIST Chemistry WebBook, SRD 69, [Online]. Available: https://webbook.nist.gov/cgi/formula?ID=B4000005&Mask=800#Electronic-Spec.

[47] M. Michael, G. L. Sharon, and N. Meot, "SO_2^+," NIST Chemistry WebBook, SRD 69, [Online]. Available: https://webbook.nist.gov/cgi/cbook.cgi?ID=C12439779&Mask=1A8F.

[48] J. H. Eland and C. J. Danby, "Photoelectron spectra and ionic structure of carbon dioxide, carbon disulphide and sulphur dioxide," *International Journal of Mass Spectrometry and Ion Physics,* vol. 1, no. 2, pp. 111-9, 1968.

[49] S. W. Crane, J. W. Lee, M. N. Ashfold and D. Rolles, "Molecular photodissociation dynamics revealed by Coulomb explosion imaging," *Physical Chemistry Chemical Physics,* vol. 25, no. 25, pp. 16672-98, 2023.

[50] R. W. Robinett, "Quantum wave packet revivals," *Physics Report,* vol. 392, no. (1-2), pp. 1-119, 2004.

[51] D. M. Holland, M. A. MacDonald, M. A. Hayes, P. Baltzer, L. Karlsson, M. Lundqvist, B. Wannberg, and W. Von Niessen, "An experimental and theoretical study of the valence shell photoelectron spectrum of sulphur dioxide," *Chemical Physics,* vol. 188, no. (2-3), pp. 317-338, 1994.

[52] Y. Mo, J. Yang and G. Chen, "Zero kinetic energy photoelectron study of $SO_2^+(X^2\ A_1)$ using coherent extreme ultraviolet radiation," *The Journal of Chemical Physics,* vol. 120, no. 3, pp. 1263-1270, 2004.

[53] H. V. Lam, Molecular-frame measurements of light-induced processes using rotational coherences driven by ultrafast laser pulses, Kansas State University, 2021.

[54] I. F. Tenney, M. Artamonov, T. Seideman, and P. H. Bucksbaum, "Collisional decoherence and rotational quasirevivals in asymmetric-top molecules," *Physical Review A,* vol. 93, no. 1, p. 013421, 2016.

[55] B. Zeng, W. Chu, G. Li, J. Yao, H. Zhang, J. Ni, C. Jing, H. Xie, and Y. Cheng, " Real-time observation of dynamics in rotational molecular wave packets by use of air-laser spectroscopy," *Physical Review A,* vol. 89, no. 4, p. 042508, 2014.

[56] P. F. Bernath, Spectra of Atoms and Molecules, Oxford University Press, 2020.

[57] S. Ghosh, A. Chiruvelli, J. Banerji, and P. K. Panigrahi, "Mesoscopic superposition and sub-Planck-scale structure in molecular wave packets," *Physical Review A—Atomic, Molecular, and Optical Physics,* vol. 73, no. 1, p. 013411, 2006.

[58] M. Protopapas, C. H. Keitel and P. L. Knight, "Atomic physics with super-high intensity lasers," *Reports on Progress in Physics,* vol. 60, no. 4, p. 389, 1997.

[59] B. Feuerstein, T. Ergler, A. Rudenko, K. Zrost, C. D. Schröter, R. Moshammer, J. Ullrich, T. Niederhausen, and U. Thumm, "Complete characterization of molecular dynamics in ultrashort laser fields," *Physical Review Letters,* vol. 99, no. 15, p. 153002, 2007.

[60] Z. Wei, J. Li, L. Wang, S. T. See, M. H. Jhon, Y. Zhang, F. Shi, M. Yang, and Z. H. Loh, "Elucidating the origins of multimode vibrational coherences of polyatomic molecules induced by intense laser fields," *Nature Communications,* vol. 8, no. 1, p. 735, 2017.

[61] P. W. Dooley, I. V. Litvinyuk, K. F. Lee, D. M. Rayner, M. Spanner, D. M. Villeneuve, and P. B. Corkum, "Direct imaging of rotational wave-packet dynamics of diatomic molecules," *Physical Review A,* vol. 68, no. 2, p. 023406, 2003.

[62] X. Li, Molecular response to ultra-intense X-rays studied with ion and electron momentum imaging, PhD thesis, Kansas State University, 2019.

[63] C. M. Maharjan, Momentum imaging studies of electron and ion dynamics in a strong laser field, PhD thesis, Kansas State University, 2007.

[64] J. Kelsall, A. Radić, J. Ellis, D. J. Ward, and A. P. Jardine, "Minimizing interference in low-pressure supersonic beam sources," *The Journal of Chemical Physics,* vol. 162, no. 9, 2025.

[65] X. M. Tong and C. D. Lin, "Empirical formula for static field ionization rates of atoms and molecules by lasers in the barrier-suppression regime," *Journal of Physics B: Atomic, Molecular and Optical Physics,* vol. 35, no. 15, p. 2593, 2005.

[66] T. Ergler, B. Feuerstein, A. Rudenko, K. Zrost, C. D. Schröter, R. Moshammer, and J. Ullrich, "Quantum-Phase Resolved Mapping of Ground-State Vibrational D_2 Wave Packets via Selective Depletion in Intense Laser Pulses," *Physical Review Letters,* vol. 97, no. 10, p. 103004, 2006.

[67] E. Goll, G. Wunner, and A. Saenz, "Formation of ground-state vibrational wave packets in intense ultrashort laser pulses," *Physical Review Letters,* vol. 97, no. 10, p. 103003, 2006.

[68] L. Fang and G. N. Gibson, "Strong-field induced vibrational coherence in the ground electronic state of hot I_2," *Physical Review Letters,* vol. 100, no. 10, p. 103003, 2008.

[69] A. Rudenko, V. Makhija, A. Vajdi, T. Ergler, M. Schürholz, R. K. Kushawaha, J. Ullrich, R. Moshammer, and V. Kumarappan, "Strong-field-induced wave packet dynamics in carbon dioxide molecule," *Faraday Discussions,* vol. 194, pp. 463-78, 2016.